THE CHARGE ASYMMETRY IN W BOSONS PRODUCED IN $p\overline{p}$ COLLISIONS AT $\sqrt{s} = 1.96$ TeV

A Dissertation

Submitted to the Graduate School
of the University of Notre Dame
in Partial Fulfillment of the Requirements
for the Degree of

Doctor of Philosophy

by

Julie Torborg, B.A.

Mitchell Wayne, Director

Graduate Program in Physics
Notre Dame, Indiana
July 2005

THE CHARGE ASYMMETRY IN W BOSONS PRODUCED IN $p\overline{p}$ COLLISIONS AT $\sqrt{s} = 1.96$ TeV

Abstract

by

Julie Torborg

The primary mode of production of W^+ bosons in a $p\overline{p}$ collider is $u + \overline{d} \rightarrow W^+$. The u quark generally carries more momentum than the $\overline{d}$ and the resultant W^+ tends to be boosted in the proton direction. Similarly, W^- bosons are boosted in the anti-proton direction. This is observed as an asymmetry in the rapidity distributions of positive and negative W bosons. Measurement of this asymmetry serves as a probe of the momentum distribution of partons within the proton. These distributions are required as input to the calculation of every $p\overline{p}$ production cross section.

This thesis presents the first measurement at DØ of the charge asymmetry of the W boson production cross section as measured in $W \rightarrow e\nu$ decays in 0.3 fb^{-1} of $p\overline{p}$ collisions collected with the DØ Detector. Theoretical predictions made using the CTEQ6.1M and MRST(2004) parton distribution functions are compared with the measurement.

DEDICATION

I dedicate this work to my partner, Josh.

"Teamwork is what the Green Bay Packers were all about. They didn't do it for individual glory. They did it because they loved one another."

Vince Lombardi

CONTENTS

FIGURES

TABLES

ACKNOWLEDGMENTS

Having loitered in graduate school for eight years, the list of people who deserve acknowlegement has grown quite long; I apologize for any omissions.

First, there are the usual suspects: my family, my advisor, and my collaboration. My parents, Roger and Sharon Torborg, deserve the lion's share of the accolades in this division, having put 31 years (yes, I am including gestation) toward the completion of this thesis. They got the tough end of it; generally only hearing from me when I needed some money, someone to move me, or some encouragement. My grandmother, Mary Helen, and siblings, Brenda, Christine, Rick and his wife Kate, Andy and Brad have each given me unique support; for that I thank them.

My advisor, Mitchell Wayne, has fought many a battle for me, and supported me with a fatherly encouragement that made me dread disappointing him. (He knows his audience–there is nothing more motivating to a Catholic-bred girl than the guilt of disappointing her father.)

Within the DØ Collaboration, which provided many more sources of support than I can name here, three names stand out: Tom Diehl, Drew Alton, and Jon Hays. Each has been a compass to me in my efforts to complete this analysis.

The second round of thanks goes to my friends; Dr. Roger Jones, who introduced me to relativity, quantum theory, and the Standard Model; my cat Zora;

and Sid Meier, whose world-conquering video games have helped me resolve a lot of stress.

Finally, and most importantly, I would like to thank my partner and fiancé, Joshua Kalk. He has helped me through this analysis in innumerable ways. In addition to making life more pleasant and meaningful, and taking care of the tedious details of life (like vacuuming, and feeding the cat) when I've been too pressed, he has had his hands in the gritty details of this analysis. He is the person I turn to when my code is broken, a plot looks nasty, or the math is hard. I may have been able to get here without him, but it would have taken longer and been a lot less fun.

CHAPTER 1

INTRODUCTION

In 2005 we celebrate the centennial anniversary of Albert Einstein's *annus mirabilis*, in which he published five papers introducing work that would be key to physics in the twentieth century. Two of the papers ([1], [2]) establish that the molecular description of matter is valid in reality, and not merely a theoretical convenience. Two of the papers ([3], [4]) develop his Special Theory of Relativity and introduce the most famous equation the world has ever known: $E = mc^2$. The final paper ([5]), the one for which he won the Nobel Prize in 1921

Absent any one of these three ideas, particle physics could not exist. The theory that particle physics is based on, called *The Standard Model*, describes matter as coalitions of particles (quarks and leptons) that interact by exchanging quanta of light (or another of the "force-mediating" bosons); and turning energy into matter (as is described by the famous equation) is the experimental particle physicist's bread-and-butter.

This analysis focuses on one of the "other" bosons, the W boson. At colliders like the Fermilab *Tevatron*, W bosons are most often produced by the head-on collision of a quark and antiquark that are each traveling at nearly the speed of light. The result is analagous to that of a head-on collision between an Hummer and a Cooper Mini: the resultant wreck (W boson) will travel in the direction that the bigger vehicle (quark) was traveling. This thesis examines the "wreckage",

the W charge production asymmetry, in an attempt to determine the ratio of the momenta of the quarks.

1.1 The Standard Model

Matter, as Einstein helped establish, is made up of molecules, which are made of atoms, which are made of protons, neutrons and electrons. When the neutron was observed in 1932, it was considered the last piece of the atomic puzzle. So neat and tidy was the picture that some physicists were ready to call the mysteries of nature solved and close up shop. That is, until studies of cosmic rays and, later, the introduction of particle accelerators would reveal the bevy of particles that would suggest the tale was not all told. Then, in 1964, George Zweig and Murray Gell-Mann independently proposed that this veritable zoo of particles, of which the proton and neutron were members, could be neatly explained by the introduction of three constituent particles, which Gell-Mann christened *quarks*.

With the discovery of the *top* quark in 1994, the quark model has been expanded to include three more types or *flavors*. The six quarks are arranged into three generations with a lepton and neutrino in each generation (see Table 1.1). Like quarks, leptons and neutrinos are spin-1/2 particles (fermions).

Mediating the interactions among the fermions are a complement of spin-1 particles (bosons). Each of these fundamental bosons, called gauge bosons after the gauge theories from which they arise, mediate one of the three fundamental forces described by the Standard Model[1] Each of these fundamental forces corre-

[1]There is, of course, a fourth fundamental force: gravity. Gravity is too weak to have a significant effect in short-range particle interactions. It has been postulated that there is a corresponding fourth gauge boson, the graviton, that carries the gravitational force, but at this time their is neither substantial experimental evidence for the graviton, nor a mathematically coherent theory of quantum gravity.

TABLE 1.1

SPIN-1/2 FERMIONS

Generation I	Generation II	Generation III	Electric Charge	Baryon Number	Lepton Number
Quarks and Antiquarks					
u (up)	c (charm)	t (top)	$+2/3$	$+1/3$	0
d (down)	s (strange)	d (down)	$-1/3$	$+1/3$	0
$\overline{u}$	$\overline{c}$	$\overline{t}$	$-2/3$	$-1/3$	0
$\overline{d}$	$\overline{s}$	$\overline{d}$	$+1/3$	$-1/3$	0
Leptons and Antileptons					
e^+ (positron)	μ^+	τ^+	-1	0	1
e^- (electron)	μ^- (muon)	τ^- (tauon)	$+1$	0	-1
Neutrinos					
ν_e	ν_μ	ν_τ	0	0	1
$\overline{\nu}_e$	$\overline{\nu}_\mu$	$\overline{\nu}_\tau$	0	0	-1

All free particles must have integer values of electric charge, baryon number, and lepton number, which are all conserved quantities. Each quark (q) and lepton (ℓ) has an associated charge- and- baryon number conjugate anti-particle ($\overline{q}$, $\overline{\ell}$.)

sponds to a type of "charge"; a particle is susceptible to the force when it carries the associated type of charge (see Table 1.2).

The mathematical intricacies of the theories that describe these interactions: Quantum electrodynamics (QED), Cabibbo-Kobayashi-Maskawa (CKM) Theory, quantum chromodynamics (QCD) and relativity, are detailed elsewhere [6]. The particles and rules of Tables 1.1 and 1.2 are enough to determine which composite particles and interactions are allowed.

TABLE 1.2

SPIN-1 GAUGE BOSONS

Force	Charge	Mediating Particles	Susceptible Particles
strong	color	gluons (g)	quarks, gluons
weak	weak	vector bosons ($W^{\pm}$, Z^0)	quarks, leptons, neutrinos
electro-magnetic	electric	photons(γ)	leptons, $W^{\pm}$, quarks

The word "color" here does not describe any optical property; it is a convenient analogy to describe the possible configurations of the multiple modes of "charge" that arise from the SU(3) gauge. Red, green and blue light combine to produce the neutral color that characterizes white light and free particles.

Particles composed of quarks are called hadrons and grouped according to the number of valence quarks [2] they carry as mesons (quark-antiquark) and baryons (3 quarks or 3 antiquarks).

The neutron is a baryon of quark combination udd, charge 0 ($2/3-1/3-1/3=0$) and baryon number +1 ($1/3+1/3+1/3=1$). A slightly different quark combination, uud, produces a baryon of charge +1 ($2/3+2/3-1/3=1$) and baryon number +1 ($1/3+1/3+1/3=1$), the proton. The same combination in antiquarks $\overline{u}\overline{u}\overline{d}$ produces the antiproton, which has charge ($-2/3-2/3+1/3=-1$) and baryon number ($-1/3-1/3-1/3=-1$) conjugate to that of the proton.

Each of these baryons has one quark of each color (anti-color) charge. No doublet of red, green and blue produces a neutral sum, but a combination of color

[2] In addition to the valence quarks, which provide a hadron its properties, there is a constantly changing "sea" of quark/anti-quark pairs.

TABLE 1.3

SELECT MESONS AND THEIR COMPOSITION

Meson	Quarks	Electric Charge
π^+ pion	$u\overline{d}$	+1
π^- pion	$d\overline{u}$	-1
K^- kaon	$s\overline{u}$	-1
K^0 kaon	$d\overline{s}$	0
ϕ phi	$s\overline{s}$	0

and anticolor will. Thus in order for mesons to be color neutral, they must be composed of a quark and anti-quark. Some examples are in Table 1.3.

In addition to binding to form composite particles, fundamental particles may annihilate to form other fundamental particles or release energy. Annihilations that produce bosons are more formally interactions between the originating particles and the absorbing particle or decay products. However, these "intermediate" states are worthy of study in their own right, which is exactly what is done in this thesis.

CHAPTER 2

W BOSON PRODUCTION ASYMMETRY

The probability that any particular interaction will occur, called the cross section and represented by σ, is one of the most frequently measured quantities in high energy physics. Cross sections give information about various properties of interacting particles, such as their size and structure.

Modeling hadronic cross sections is complicated by structure within the hadron: a $p\overline{p}$ interaction is actually the interaction of a quark or gluon (parton) from the proton and another from the antiproton. Contributions from Next-to-Leading Order (NLO) and higher processes (Figure 2.2) cannot be calculated using perturbation theories. Instead these cross sections are calculated using *factorization* and *renormalization* techniques.

2.1 Factorization and Renormalization

Attempts to calculate hadronic cross sections using perturbation theory are stymied by the occurance of divergences in NLO and higher corrections. These divergences come in three forms: infrared (IR), ultraviolet (UV), and collinear gluon emission (Figure 2.3).

IR divergences result from contributions of gluons with very small energy approaching zero. Conversely, UV divergences are the result of attempting to integrate over infinite energies. These divergences can be compensated for using

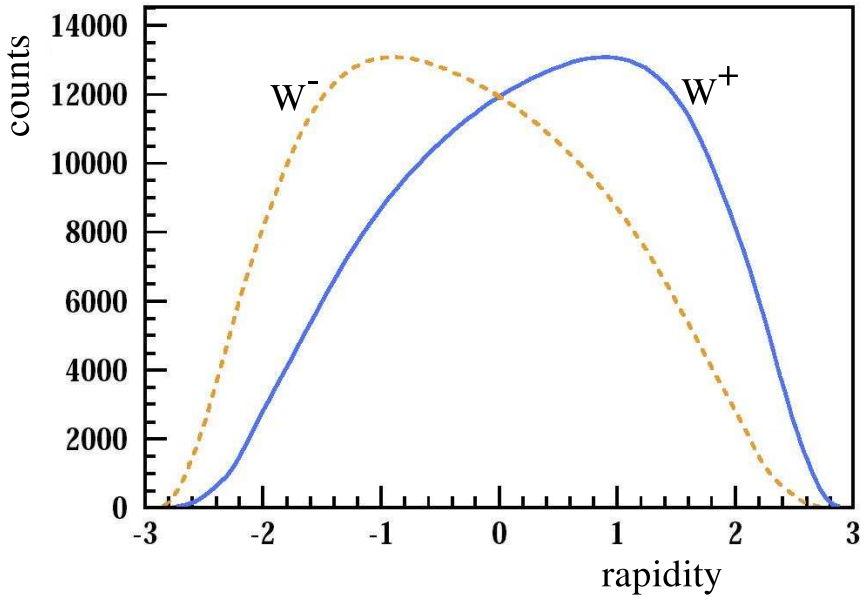

Figure 2.1. Schematic representation of the W boson asymmetry as a function of rapidity. Adapted from [7].

renormalization techniques, which impose cutoffs to prevent the divergences from becoming infinite.

As yet, no sufficient theoretical technique has been established to compensate for collinear gluon emission. The cross section equations can, however, be factorized such that the parts that are perturbative by renormalization and non-perturbative parts are convolved by simple multiplication, as shown in Equation 2.1.

$$\sigma_{P+\overline{P}\to X} = \sum_{ij} \int d\boldsymbol{p}_i d\boldsymbol{p}_j f_i(x_i) f_j(x_j) \sigma_{ij\to X}(\boldsymbol{p}_i \boldsymbol{p}_j). \tag{2.1}$$

Here, the sum is over all partons, and $\sigma_{ij\to X}(\boldsymbol{p}_i \boldsymbol{p}_j)$ is the perturbative calculation of the partonic cross section. The non-perturbative term $f_i(x_i)$ is the

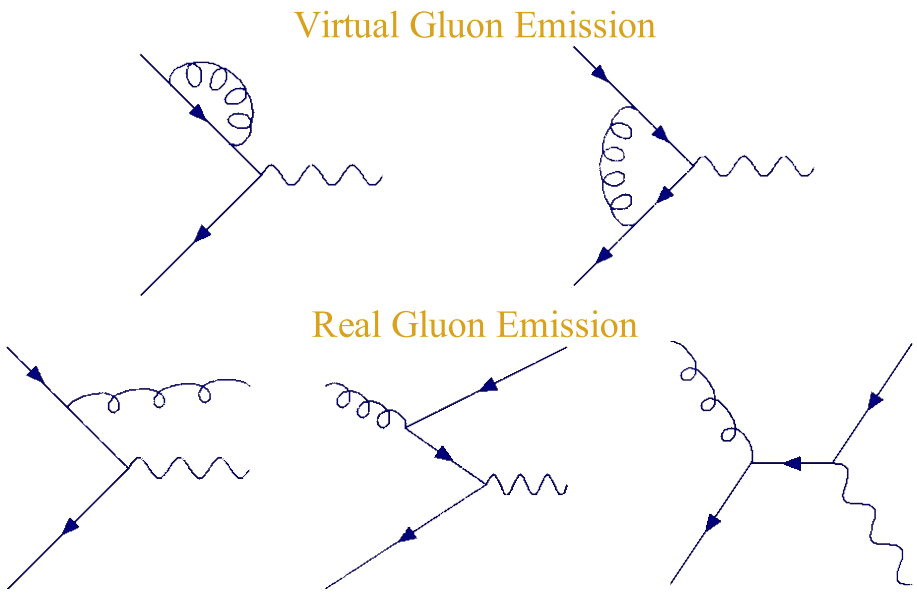

Figure 2.2. Next-to-Leading Order terms that contribute to the W boson cross section.

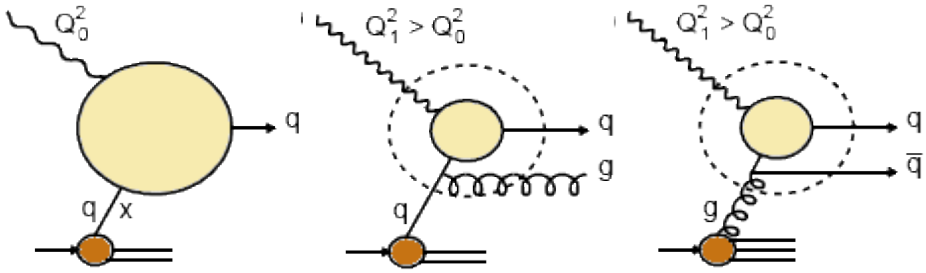

(a) Ultraviolet (b) Infrared (c) Collinear gluon

Figure 2.3. NLO corrections to the W boson cross section cannot be calculated perturbatively because some of the terms diverge. The ultraviolet and infrared divergences are reconciled by using resummation techniques, the collinear gluon emmission terms are determined by experimental measure.

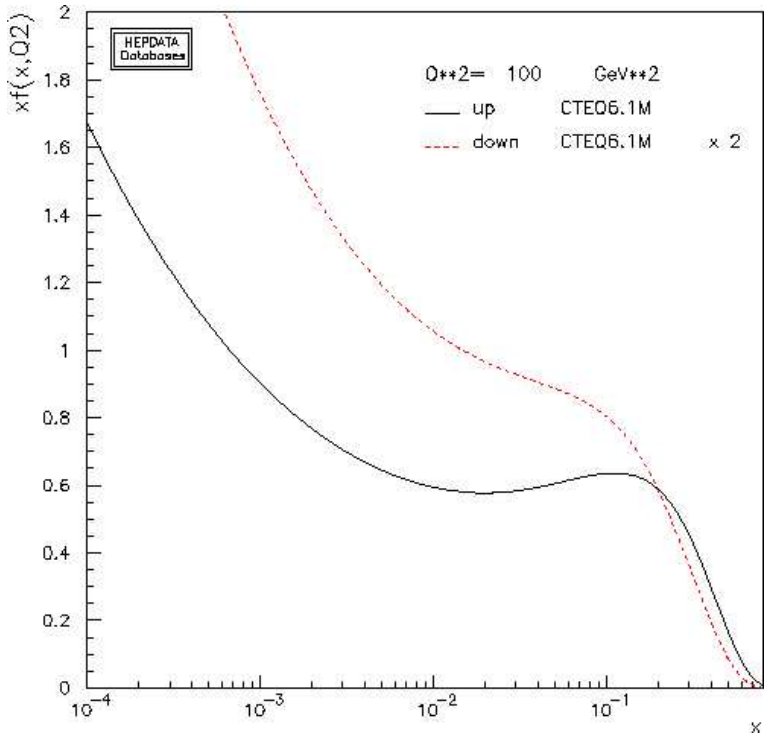

Figure 2.4. Theoretical parton distribution functions at Q^2=100 GeV; $xf(x)$ vs. x. The function $xu(x)$ has been scaled by a factor of 2 to demonstrate that $u(x) \neq 2d(x)$.

probability of finding parton i in the proton with $x_i = |\boldsymbol{p}_i|/|\boldsymbol{P}|$, where $\boldsymbol{P}$ is the momentum of the proton. The function $f_j(x_j)$ is the same probability for the antiproton.

Since there are two u and one d quarks in the proton, $\int f_u(x)dx = 2$ and $\int f_d(x)dx = 2$. It would be reasonable to expect that $f_u(x) = 2f_d(x)$ for all x. Experiments show that this is not the case; that $f_u(x)$ peaks at a slightly higher value of x (see Figure 2.4). The reason for this is not well-defined: it is "hidden" in the non-perturbative nature of the functions.

These functions, called Parton Distribution Functions (PDF), are incalculable, but can be probed experimentally. Additionally, once these functions are deter-

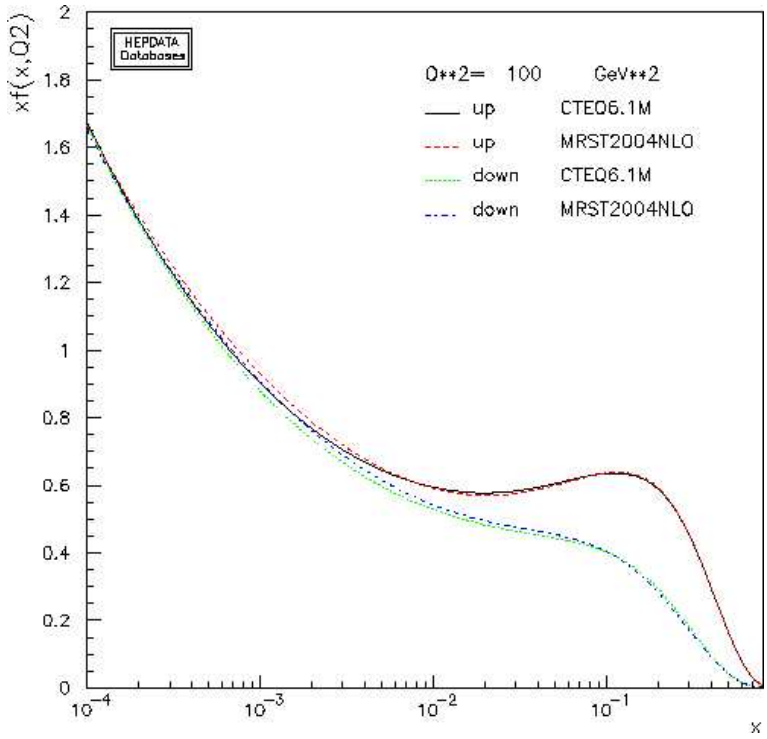

Figure 2.5. PDF distributions for u and d from CTEQ and MRST at $Q^2 = 100GeV$. The distributions are very similar; dissimilarity is confined to the region $x < 10^{-1}$ $(y > 2)$.

mined for one value of x and Q^2 (square of the momentum transfer), they can be perturbatively evolved to other moderate ($x \approx 0.1$) x and Q^2 using Alterelli-Parisi equations [8].

Experiments designed to study PDF do not directly measure the functions $u(x)$ and $d(x)$. Deep Inelastic Scattering (DIS) experiments measure Structure Functions that are functions of the PDF [9]. The W boson charge asymmetry measures the slope of the ratio $d(x)/u(x)$. It is the work of collaborations of high energy theorists to extract from these experimental measures the underlying PDF.

The two most prominent of these collaborations are CTEQ (Coordinated Theoretical-Experimental Project on QCD) and MRST (Martin-Roberts-Ryskin-

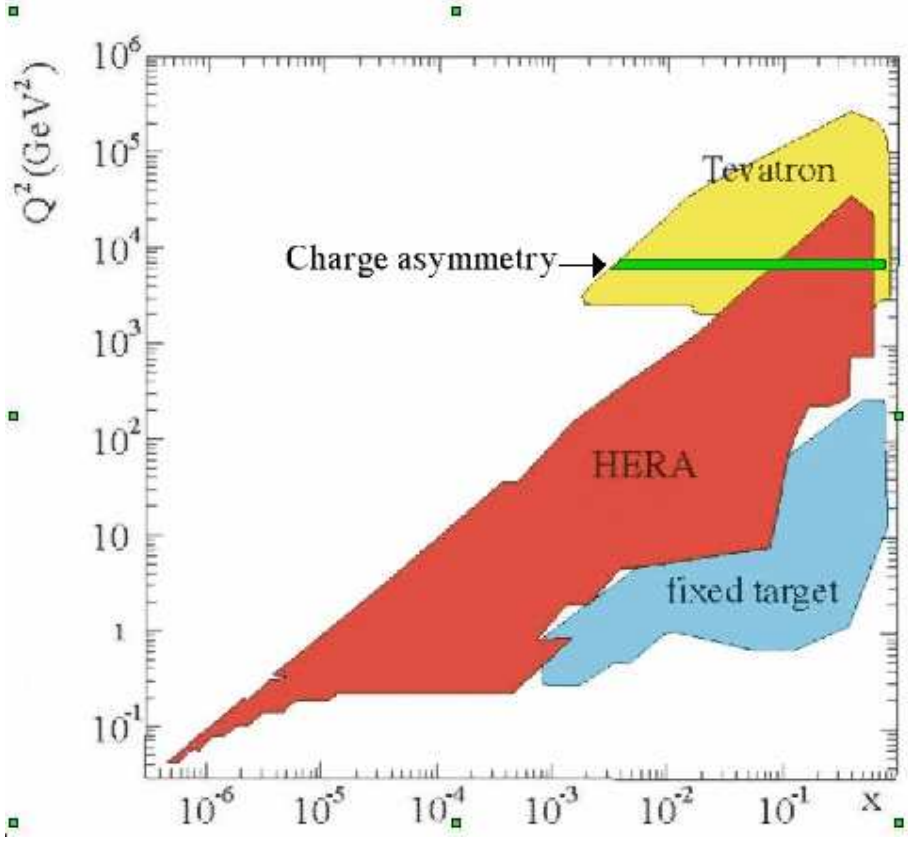

Figure 2.6. Range of x and Q^2 probed by traditional fixed target experiments, HERA collider experiments, and the Tevatron. The region probed by the W boson charge asymmetry is shown in green.

Stirling). The two collaborations produce PDF that are remarkably similar (see Figure 2.5), despite the many differences in the collaborations' techniques, including:

- experimental data used
- treatment of disparate experimental results
- fit tolerance
- factorisation/renormalisation scheme/scale

- treatment of heavy flavours
- theoretical assumptions about $x \to 0, 1$ behaviour
- theoretical assumptions about sea flavour symmetry
- evolution and cross section codes

As seen in Figure 2.6, DIS experiments probe a wide range of x, Q^2 space. However, the Q^2 at the Tevatron tends to be higher than at DIS experiments. The W boson charge asymmetry, unlike DIS, provides a direct probe of the PDF at the high Q^2 of Tevatron interactions.

2.2 W Boson Production

At $p\overline{p}$ colliders, W bosons are most often produced by the annihilation of an u quark from the proton and a $\overline{d}$ quark from the antiproton or a d quark from the proton and a $\overline{u}$ quark from the antiproton. Conservation of charge requires that the $u\overline{d}$ combination produce a W boson with positive electric charge. The u quark generally carries more momentum than the d quark, such that the resultant W^+ boson is boosted in the direction of the proton. Similarly, the combination $d\overline{u}$ produces a negatively charged W boson, which is boosted in the antiproton direction (Figure 2.1). The W boson charge asymmetry, defined as

$$A(y) = \frac{\frac{d\sigma_{W+}}{dy} - \frac{d\sigma_{W-}}{dy}}{\frac{d\sigma_{W+}}{dy} + \frac{d\sigma_{W-}}{dy}} \tag{2.2}$$

where y is the rapidity as defined below, is a measurement of the differences in these boosts.

2.3 Rapidity

Both the proton and antiproton beams are highly relativistic, as are many of the particles produced when they interact. It is convenient to measure the boost of the W boson in a Lorenz invariant dimension.

Since the beams only have momentum in one dimension, coordinates can be defined such that all of the momentum lies along one axis, say here the z-axis. Consequently, any relativistic boost of the interaction products is strictly along the z-axis.

The rapidity, y, is a quantity that is Lorenz invariant under transformations along the z-axis. It is defined in terms of the z-momentum, p_z, and energy, E, of a particle:

$$y = \frac{1}{2} ln \frac{E + p_z}{E - p_z}. \tag{2.3}$$

2.4 Relationship of Rapidity and Momentum Fraction

In the interaction $q\overline{q} \rightarrow X$, momentum and energy must be conserved. Energy is a scalar sum, $E_X = E_q + E_{\overline{q}}$. Since $m_q << E_q$, the approximation $E_q = |\boldsymbol{p}_q| = p_q$ is used, such that

$$E_X = p_q + p_{\overline{q}}. \tag{2.4}$$

All the momenta are restricted to the z-axis, with the beam momenta in opposite directions, such that the vector sum of the momenta, $\boldsymbol{p}_X = \boldsymbol{p}_q + \boldsymbol{p}_{\overline{q}}$, reduces to

$$p_X = p_q - p_{\overline{q}}. \tag{2.5}$$

Substituting (2.4) and (2.5) in (2.3) for the W boson rapidity produces:

$$y_X = \frac{1}{2} ln \frac{p_q}{p_{\overline{q}}}. \tag{2.6}$$

Consider the quark and anti-quark to have momentum fractions of

$$x_q = \frac{|\boldsymbol{p}_q|}{|\boldsymbol{P}|} \tag{2.7}$$

and

$$x_{\overline{q}} = \frac{|\boldsymbol{p}_{\overline{q}}|}{|\boldsymbol{P}|}, \tag{2.8}$$

respectively, where $\boldsymbol{P}$ is the momentum of the proton, E_{beam}. Substitution into (2.6) yields

$$e^{2y_X} = \frac{x_q}{x_{\overline{q}}} \tag{2.9}$$

which shows that the rapidity of the W boson is an indicator of the relative momenta of the partons. More explicitly, the relationship

$${E_X}^2 = {m_X}^2 + {p_X}^2 \rightarrow x_q x_{\overline{q}} = \frac{{m_X}^2}{s} \tag{2.10}$$

where $\sqrt{s} = 2E_{beam}$, can be used to solve for x_q and $x_{\overline{q}}$:

$$x_q,\ x_{\overline{q}} = \frac{m_X e^{\pm y}}{\sqrt{s}}. \tag{2.11}$$

The significant experimental variable here is the rapidity. This equation makes it clear that the wider the range of rapidities probed, the wider the range of x.

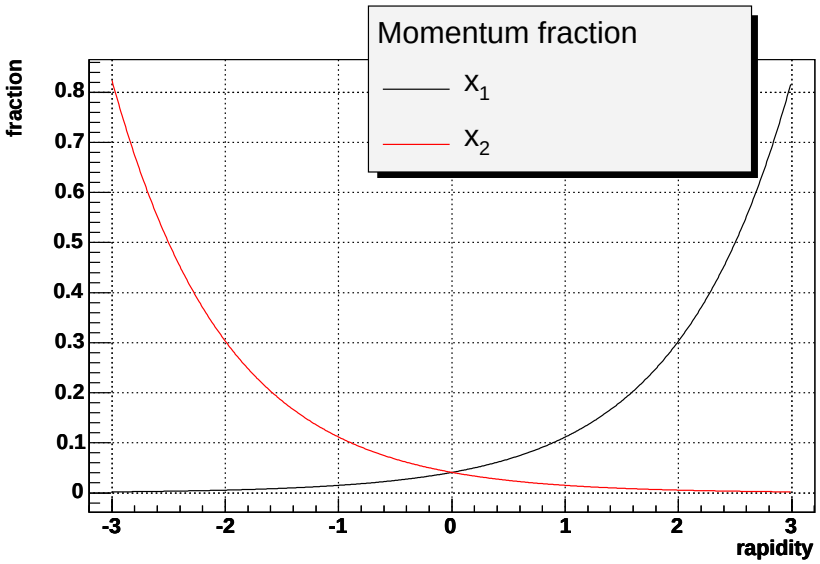

Figure 2.7. The values of x probed by the charge asymmetry as a function of rapidity, as obtained by Equation (2.11), with $m_X e^{\pm y} = 80.41$ GeV and $\sqrt{s} = 1.96$ TeV. For the rapidity range $-3.0 < y < 3.0$, the momentum fraction range is $0.002 < x < 0.8$.

Equation (2.11) was used to make the distributions in Figure 2.7, which shows the x values probed as a function of rapidity.

2.5 Hadronic Cross Section

Recall from Section 2.1 that Equation (2.1), a convolution of the partonic cross sections and the momentum distribution of the partons, can be used to calculate the cross section for a generic $p\overline{p}$ process. When the process is specified to be W boson production, sea quark contribution to the cross section is negligible such that W^+ bosons are considered to be produced solely by the annihilation of an u and $\overline{d}$ quark, and the sum reduces to:

$$\sigma_{P+\overline{P}\to W^+} = \int d\boldsymbol{p}_u d\boldsymbol{p}_{\overline{d}} \cdot f_u(x_1) f_d(x_2) \sigma_{u\overline{d}\to W^+}(\boldsymbol{p}_u, \boldsymbol{p}_{\overline{d}}) \tag{2.12}$$

For the sake of simplicity, $f_u(x)$ will be known as $u(x)$, and $f_d(x)$ will be known as $d(x)$. It is assumed that $u(x) = \overline{u}(x)$, etc.

In the limit that the W boson mass resonance has no width, $\sigma_{u\overline{d}\to W^+}(\boldsymbol{p}_u, \boldsymbol{p}_{\overline{d}})$ only has value when the center of mass energy of the $u\overline{d}$ system, $\sqrt{\hat{s}}$, is M_W, as described by Equation 2.13.

$$\sigma_{u\overline{d}\to W^+}(\boldsymbol{p}_u, \boldsymbol{p}_{\overline{d}}) = k\delta((p_u + p_{\overline{d}})^2 - M_W^2) \tag{2.13}$$

Converting from momentum to momentum fraction using the relationships in Equations 2.7 and 2.8, this becomes

$$\sigma_{u\overline{d}\to W^+}(\boldsymbol{p}_u, \boldsymbol{p}_{\overline{d}}) = k'\delta(x_1 x_2 - \frac{M_W^2}{s}), \tag{2.14}$$

and Equation 2.12 becomes

$$\sigma_{P+\overline{P}\to W^+} = K \int dx_1 dx_2 \cdot u(x_1) d(x_2) \delta(x_1 x_2 - \frac{M_W^2}{s}). \tag{2.15}$$

Integration with respect to dx_2 produces a constant:

$$\sigma_{P+\overline{P}\to W^+} = K' \int dx_1 \cdot u(x_1) d(x_2) \tag{2.16}$$

Substituting Equation 2.11 and differentiating with respect to y yields:

$$\frac{d\sigma_{P+\overline{P}\to W^+}}{dy} = K' \cdot u(x_1) d(x_2). \tag{2.17}$$

This equation, along with its conjugate, the differential cross section for production of W^- bosons, is substituted into (2.2) to produce:

$$A(y) = \frac{u(x_1)d(x_2) - u(x_2)d(x_1)}{u(x_1)d(x_2) + u(x_2)d(x_1)} \tag{2.18}$$

This equation can be rearranged to clarify that the asymmetry is a probe of the slope of $d(x)/u(x)$:

$$A(y) = \frac{u(x_1)/d(x_1) - u(x_2)/d(x_2)}{u(x_1)/d(x_1) + u(x_2)/d(x_2)} \tag{2.19}$$

2.6 W Boson Decay

It is impossible to directly detect W bosons at DØ: not only do they have an extremely short mean life ($\approx 3 \times 10^{-25} s$) but their momentum is along the z-axis which is within the beam pipe and uninstrumented. Instead, W bosons are identified by their decay products.

Almost 70% of the time, W bosons decay hadronically, but it is nearly impossible to separate $W \rightarrow q + \overline{q}$ from the direct production of quark-antiquark pairs. The remaining 30% of the time, W bosons decay to a lepton and neutrino, which produces a relatively distinct signal of a lepton and missing energy. While W bosons decay equally into all the lepton channels, this analysis studies the electron channel exclusively.

Naively, it could be expected that when the W boson decays, the lepton and neutrino momentum may have any direction, as long as momentum is conserved. However, the leptonic decay of the W boson is governed by a V-A coupling [10], which constrains the angular distribution of the electrons by placing restrictions on the *helicity* of the particles involved.

Helicity is the relationship between a particle's momentum and its angular spin, defined as

$$H \equiv \frac{\boldsymbol{s} \cdot \boldsymbol{p}}{|\boldsymbol{s} \cdot \boldsymbol{p}|} \tag{2.20}$$

where $\boldsymbol{s}$ is the angular momentum vector. It is clear that when $\boldsymbol{p} = 0$, the helicity is undefined. When momentum and spin are aligned ($H = 1$), a particle is said to be "right-handed"; when they are counter-aligned ($H = -1$), a particle is "left-handed."

The nature of the electroweak theory requires that W bosons couple exclusively to left-handed quarks and leptons or right-handed antiquarks and antileptons. This requires that to produce a W^+ boson, the u must be left-handed, and the $\overline{d}$ right-handed, as in Figure 2.8-a. Similarly, in Figure 2.8-b, when the W^+ boson decays electronically[1], the e^+ (an antiparticle) must be right-handed and the ν_e left-handed.The direction of motion of the e^+ is **antiparallel** that of the proton, whereas the direction of the W^+ boson tends to be parallel to it. This means that the electron decay of the W boson is asymmetric and this asymmetry tends to cancel the production asymmetry.

The *measured* electron asymmetry, as defined in Equation 2.21, is a convolution of the decay asymmetry and the production asymmetry (Figure 2.9).

$$A(y_e) = \frac{d\sigma(e^+)/dy - d\sigma(e^-)/dy}{d\sigma(e^+)/dy + d\sigma(e^-)/dy} \tag{2.21}$$

Luckily, the lepton decay distribution is well-understood, such that measurement of the electron asymmetry provides information about the slope of $d(x)/u(x)$ com-

[1]The argument here can be generalized to all leptonic decays. The electron channel is used as an example because it is the one measured in this analysis.

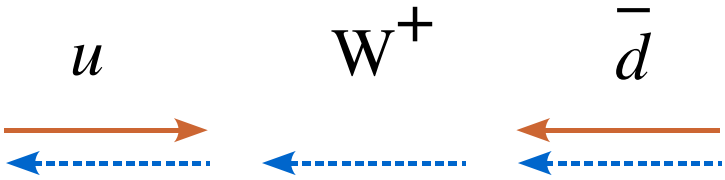

(a) W^+ boson production in $p\overline{p}$ collisions.

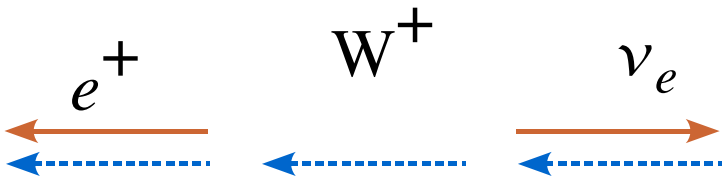

(b) Leptonic decay of W^+ bosons.

Figure 2.8. The momentum (solid lines) and spin (dashed lines) of particles in W^+ boson production and leptonic decay. If the momentum vector of the e^+ is reversed, its helicity becomes negative, which is not allowed. Reversing the direction of the momentum vector **a**nd the spin vector would maintain the positive helicity required, but reversal of the spin vector is not allowed, because angular momentum must be conserved. Figure adapted from [11].

mensurate with that which could be obtained by measuring the W boson asymmetry.

2.6.1 Experimental Formulae

The formula used in the experimental measure of cross sections is:

$$\sigma(X) = \frac{N_X}{\mathcal{L}\mathcal{A}_{\mathcal{X}}\varepsilon_{\mathcal{X}}} \tag{2.22}$$

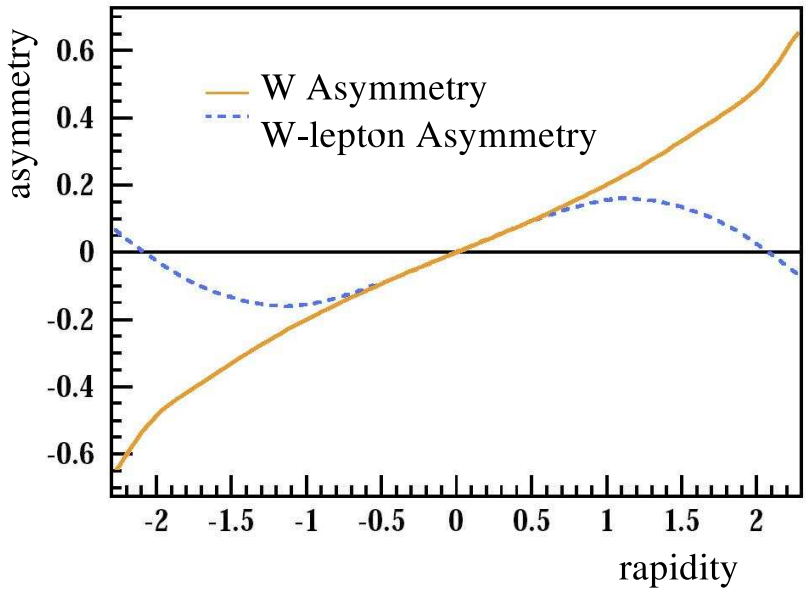

Figure 2.9. The measured lepton rapidity is a convolution of the W boson production asymmetry and the V-A decay asymmetry of leptons. The V-A decay asymmetry is a function of $cos(\theta_e)$ where θ_e is the angle between the electron momentum and the proton momentum. The sign change of the measured asymmetry at $y \approx 2$ is a result of the $cos(\theta_e)$ dependence. Schematic diagram adapted from [7].

where N_X is the number of X events, A_X is the acceptance of the detector, $\mathcal{L}$ is the luminosity[2] and ε_X is the efficiency for identifying X. Note that the luminosity is independent of X, and cancels when equations 2.22 and 2.21 are combined. Similarly, if A_X and ε_X are charge independent[3], the asymmetry measurement is reduced to a counting experiment:

$$A(y_e) = \frac{N_{e^+}(y) - N_{e^-}(y)}{N_{e^+}(y) + N_{e^-}(y)}. \tag{2.23}$$

[2]Essentially, luminosity is the intensity of the beam as defined by the number of particles and their distribution, and the frequency of interactions.

[3]Evidence for this position will be given in a later chapter.

This thesis produces the $A(y_e)$ distribution from $\approx 300 pb^{-1}$ data collected by the DØ Collider Detector at Fermilab from August 2002 to June 2004. This distribution is compared to the asymmetry predictions of theoretical PDF distributed by the CTEQ and MRST collaborations.

CHAPTER 3

THE TEVATRON

In 1930, when John Cockcroft and Ernest Walton rigged together a 200-kilovolt transformer to accelerate protons down a straight discharge tube, their apparatus sat on a lab table and cost about £500. In the quest to achieve the higher energies that produce heavier and more exotic particles, particle accelerators have grown in complexity, volume and cost. The highest-energy accelerator in operation is the Tevatron at Fermilab (Fermi National Accelerator Laboratory) which occupies 6,800 acres of former farmland in Batavia, Illinois, about 40 miles west of Chicago.

The accelerator at Fermilab is called the Tevatron in honor of its ability to produce center of mass energies[1] ($\sqrt{s}$) of tera electron volt (TeV) magnitudes. The Tevatron is a circular proton-antiproton ($p\overline{p}$) superconducting synchrotron.

3.1 Design Choices

Circular colliders are not without their disadvantages, not the least of which is that beams are depleted of energy by synchrotron radiation, a result of the radial acceleration component required to move a charged particle on a circular trajectory. Using protons helps reduce the problem; synchrotron radiation is a function of mass, and protons are massive relative to electrons, which is the other

[1] The center of mass energy is the effective energy of the collision.

charged particle frequently used in high energy accelerators. Further compensation is made by the ability to accelerate the beam through the same section of beam pipe multiple times. Particles can be accelerated over much greater distances than could ever be practical for an accelerator of linear design and beams can be reused simply by circulating them in the accelerator. In linear colliders, the amount of energy required to re-target particles that don't interact in an initial crossing is larger than that required to regenerate the beam, so it is simply dumped.

While fixed-target varieties of accelerator produce a single beam that is targeted at a fixed block of material to produce particle interations, a collider produces two beams of particles and targets them at each other to produce interactions. This offers the clear advantage that each of the particles in the interaction carries the energy of being accelerated. Because the particles involved are highly relativistic, the center-of-mass energy gets a quadratic boost[2] in collider mode.

Protons are abundant in everyday matter and easily extracted from hydrogen atoms by stripping them of their electrons. Producing antiprotons is a difficult and expensive process, but there are distinct benefits of colliding particle-antiparticle pairs. Since they have the same mass and opposite charge, they can be circulated in the Tevatron simultaneously in opposite directions with the same set of bending magnets. At center of mass energies up to about 3 TeV, the production rate for some processes is higher for $p\overline{p}$ collisions than pp collisions.

[2]In fixed target mode, $\sqrt{s} \propto \sqrt{E}$. In collider mode, $\sqrt{s} \propto E$.

3.2 History

The Tevatron first produced $p\overline{p}$ collisions in 1985. By 1988, $\sqrt{s}$=1.8 TeV had been achieved, and the collider would run at this energy throughout Run I (1992-1996), delivering 130 pb^{-1} to each of the collider detectors. In recent years the Tevatron was upgraded to become the world's highest energy collider at $\sqrt{s}$=1.96 Tev. In 2001 it began delivering luminosity for Run II, which will continue at least until the Large Hadron Collider at CERN begins operation toward the end of the decade.

3.3 The Tevatron Today

Though often referred to as "the Tevatron," the Fermilab accelerator is actually a multi-stage system of accelerators, of which the Tevatron is the terminating element. The full system is shown in figure 3.1.

The colliding beams of the Tevatron originate as an ordinary "C" size cylinder of compressed hydrogen gas (H_2). The hydrogen atoms are ionized by the addition of electrons. This gives the resultant H^- ions the net charge required to route them through the system electromagnetically. The H^- ions are fed into a Cockroft-Walton preacclerator, where they are accelerated to 750 keV, then bunched and led into a 150 m long Alvarez-type linear accelerator (Linac). The oscillating electric fields of the Linac accelerate the ions to 400 MeV.

Passing the H^- ions through a carbon foil stripsto re-target particles that don't interact in an initial crossing them of their electrons, at which point they cease being hydrogen atoms and become naked protons. The protons are directed into the Booster, a 475 m circumference synchrotron. Protons take 16,000 turns

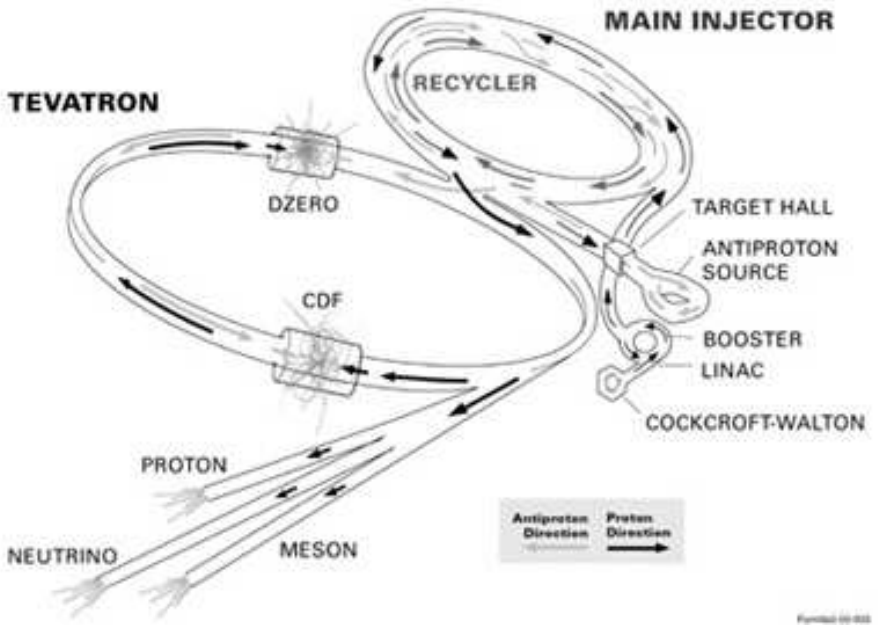

Figure 3.1. Fermilab accelerator complex.

around the Booster, accelerating to 8 GeV in 0.033 second before they are guided into the Fermilab Main Injector (FMI).

The FMI is an irregularly shaped oval synchrotron with a circumference of 3.3 km that accelerates the beam to 120 GeV (for antiproton generation) or 150 GeV (for injection into the Tevatron). As part of the Run II upgrade to the Tevatron, the Fermilab Main Ring, which had operated for 25 years, was decommissioned and replaced by the FMI. The circumference of the new FMI ring is approximately half that of the Main Ring, but uses all 18 of the Main Ring's RF quadrupoles, effectively doubling the rate at which protons can be accelerated.

Some of the protons from the FMI are diverted to the antiproton generation cycle. The Anti-Proton Source consists of three major components: the Target Station, the Debuncher, and the Accumulator.

At the Target Station, a beam of 120 GeV protons from the Main Injector is focused on a nickel target, generating various products, a small fraction of which are antiprotons[3]. The product particles are then collimated by a lithium lens and unwanted particles are filtered away by sending the beam through a pulsed magnet which acts as a charge-mass spectrometer.

Because the $\overline{p}$ beam was created with a bunched p beam, the $\overline{p}$ beam is bunched. In addition, antiprotons come off the target at various energies. This large spread in energy of the antiprotons is difficult for downstream accelerators to accept. The Debuncher accelerator is an 8 GeV synchrotron used to exchange the large energy spread and narrow time spread into a narrow energy spread and large time spread. Antiprotons with different energies reach the Debuncher's RF cavities at slightly offset times. Thus the RF phase that they are exposed to will be slightly offset. Lower energy antiprotons arrive at a phase where the RF provides a boost, and conversely for higher energy antiprotons. After multiple cycles, the large energy spread has been traded for a large time spread. The debunching process takes about 100 milliseconds. They are then stochastically cooled [12] until they are injected into the Accumulator (1.5 s).

The Accumulator is another 8 GeV synchrotron that shares a triangular "ring" with the Debuncher. As the name suggests, the purpose of the Accumulator is to store the accumulating antiproton stack. About 5 x 10^{12} antiprotons are required to generate a beam. Stacked at a rate of 10^{11} protons/hour, this process can

[3]For every 1 million protons that hit the target, only about twenty usable antiprotons are produced.

take hours or days. Stacking and storing is accomplished by momentum stacking successive pulses of antiprotons using RF and stochastic cooling systems. As the stack increases, the stacking rate decreases. To keep the Accumulator stacking efficiently, the stack is periodically dumped into the Recycler.

The Recycler is a fixed-energy storage ring placed in the Main Injector tunnel directly above the Main Injector beamline, near the ceiling. In addition to acting as storage for antiprotons coming out of the Accumulator, the Recycler can accept 980 GeV antiprotons from the depleted beam at the end of a Tevatron store. The Recycler cools these antiprotons to 150 GeV and transfers them to the FMI. The FMI decelerates the beam to 8 GeV and returns them to the Recycler stack. Since as little as 25% of the antiprotons in the beam are consumed in collisions, this increases the effective stacking rate dramatically.

The Fermilab Tevatron was the world's first superconducting synchrotron. The large magnetic fields (up to 4.2 Tesla) required to bend and focus high energy proton and antiproton beams contraindicates the use of conventional copper-wire electromagnets, as the amount of electrical energy dissipated as heat is prohibitive. Because superconducting wire provides no electrical resistance, there is no heat energy lost. Significant resources (13 MW) are required to keep the Tevatron's magnets at superconducting temperature (4.3 Kelvin) but the trade-off remains a positive one.

Thirty-six bunches of protons from the FMI and 36 bunches of antiprotons from the Recycler are injected into the Tevatron and circulate in opposite directions. Once the beams have been accelerated to 980 GeV, they are bent by quadrupole magnets to cross at interaction points B0 (CDF) and D0 (DØ) at a rate of 1 crossing per 396 ns (2.5 million crossings per second, about half of which involve

a populated bunch to produce an interaction rate of ≈1.7 MHz). Interactions deplete the proton and antiproton populations and reduce the likelihood that a beam crossing will produce interactions. After several (10-20) hours of collisions, it is no longer efficient to circulate the depleted beams, and the stores are recycled or "dumped" (redirected into a block of absorbing material). Generally, while one store is colliding, another is being prepared so that the down time between stores is minimal.

CHAPTER 4

THE DØ COLLIDER DETECTOR

Data for this thesis was collected by the DØ Experiment at Fermilab. Comprised of roughly 650 students and scientists from 70 institutions in 19 nations, the DØ Collaboration is resposible for building and maintaining the DØ Collider Detector. Approximating a 4-story cube and weighing in at 5500 tons, the DØ Detector is the slightly smaller of the two detectors at Fermilab, the other being CDF (Collider Detector at Fermilab).

The challenge of building a collider detector is to get a bevy of particles (hadrons, leptons, bosons) to deposit the entirety of their energy electromagnetically, in such a manner that the properties of the particles (momentum, energy, charge) can be determined. Typically this challenge is met by employing a combination of tracking detectors, which have fine position resolution and coarse energy resolution; and calorimeters, which trade position resolution for energy resolution. With no less than three trackers and three calorimeters, the DØ detector is no exception.

The DØ detector is built concentrically around the beampipe, (Figure 4.1) trending from fine to coarse position resolution. Closest to the beamline is the central tracking: the Silicon Microstrip Tracker (SMT), the Central Fiber Tracker (CFT), a 2 T superconducting solenoidal magnet, and Central and Forward Preshower (CPS, FPS) detectors. Next to the central tracking is a layer of calorimetry: the

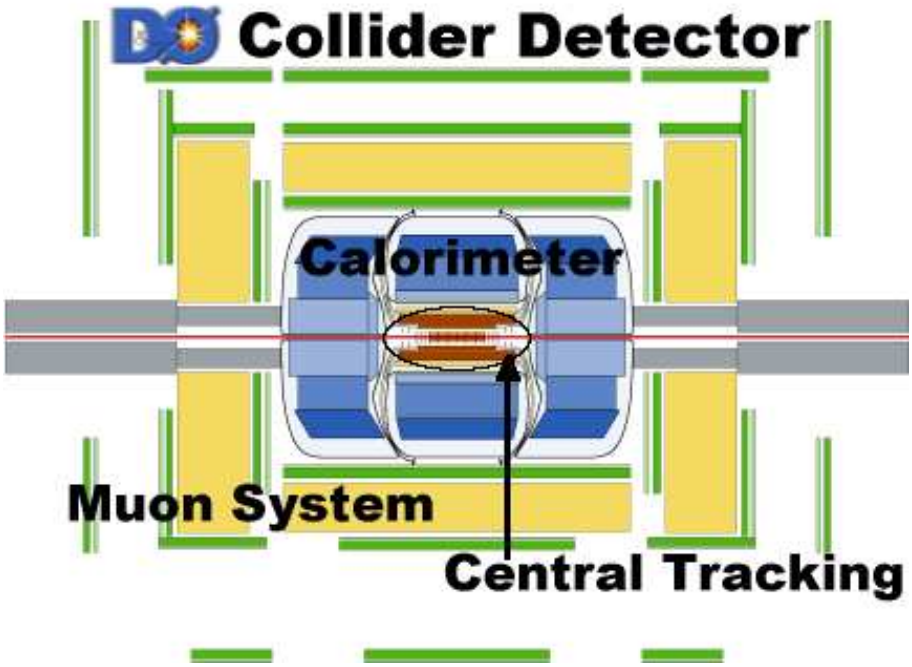

Figure 4.1. The DØ Collider Detector is built concentrically around the beam pipe (shown here in red).

Central Calorimeter (CC) and two End Calorimeters (EC), all housed in separate cryostats. The exterior of the detector is a muon system that consists of a layer of tracking detectors and scintillation trigger counters, a layer of 1.8 T toroids, and two more layers of detectors after the torroidal magnets.

4.1 DØ Coordinate System

The base coordinate system at DØ is right-handed cartesian in which the z-axis is along the proton direction and the y-axis points upward (Figure 4.2). Measurement of the 4-momenta of particles are made relative to this coordinate system. However, because all the particles in these collisions are highly relativistic,

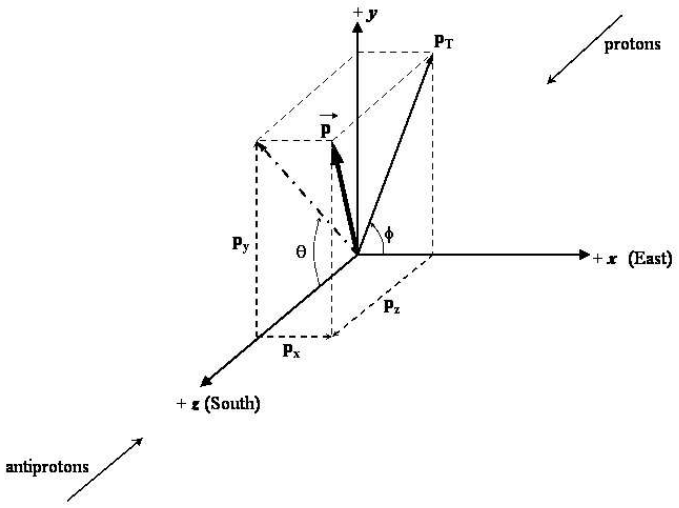

Figure 4.2. The DØ coordinate system.

it is often advisible to use a Lorentz invariant coordinate system. Conveniently, the definition of the cartesian coordinate system restricts the relative motion between the lab frame and the particle frame to the z-axis such that the rapidity, y,

$$y = \frac{1}{2} ln \frac{E + p_z}{E - p_z} \tag{4.1}$$

is Lorentz invariant. Locating a point uniquely in three-dimensional space requires a third coordinate, ϕ, which is the projection angle in the x-y plane where ϕ=0 is coincident with the positive x-axis.

While y, ϕ and z fully define a coordinate space, oftentimes the energy and momentum of a particle are not well known. A convenient approximation of the rapidity is the pseudorapidity, η,

$$\eta = -ln(tan(\frac{\theta}{2})) \tag{4.2}$$

where θ describes the angle in the y-z plane of projection with θ=0 in the proton direction. This approximation is valid in the case that $p >> m$ and $\theta >> mc^2/E$ [13]. In the limit $m/E \rightarrow 0$, rapidity and pseudorapidity are equivalent.

It is important to note here the difference between detector coordinates and physics coordinates. Essentially, they are the same coordinate system but with different origins; one fixed in the lab frame at the intersection of the beam line and the line of left-right symmetry of the detector, the other differing from event to event according to the reconstructed interaction point. Ideally, the interaction would always occur at the lab origin, and the systems would be identical. In reality, the interaction point is distributed around the lab origin (Figure 4.3). This is corrected for by recalculating the coordinates using the offset origin.

As may be expected, detector coordinates are appropriate for describing the detector. These are also the coordinates used for making cuts related to the topology of the detector.

When defining the position of a reconstructed particle, it is appropriate to use physics coordinates. In this thesis, use of physics coordinates is assumed, and references to detector coordinates will be noted by the subscript *det*.

4.2 Run II Upgrade [14]

In addition to increasing the center-of-mass energy, the upgrade of the Tevatron between Run I and Run II increased the bunch occupancy and crossing frequency[1], making it necessary to upgrade the detector's trigger system and readout electronics.

[1]By a factor of 2 and 10 respectively.

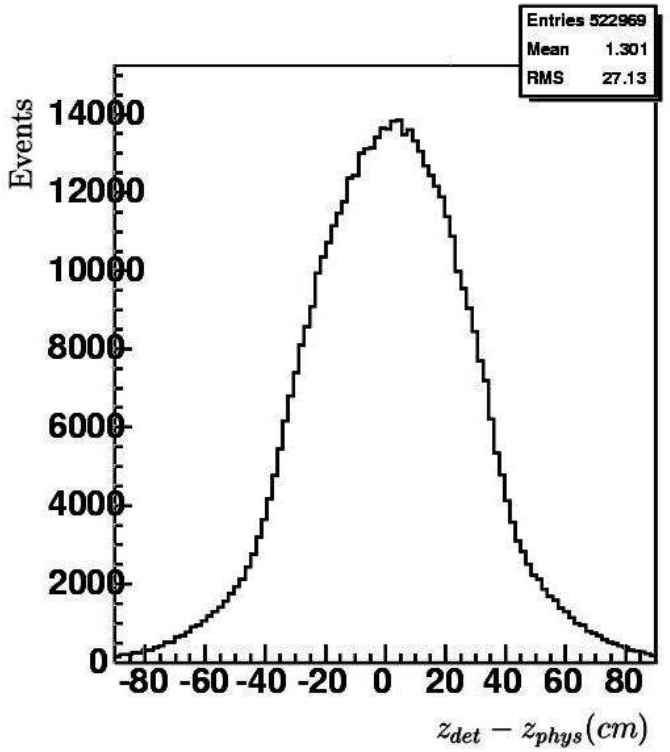

Figure 4.3. Distribution of the z coordinate of the interaction point relative to the lab origin.

Advances in technology made it possible to introduce a superconducting solenoid into the Run I central tracking volume by compacting the central tracker. The addition of magnetic tracking, while useful for many analyses, is indispensable to this one, as it is critical to determining the charge of electrons.

Addition of the solenoid dramatically altered the materials density structure of the inner tracking. Particles shower sooner, degrading the energy resolution and background rejection of the calorimeter. Preshower detectors were added between the solonoid and the calorimeter to compensate.

4.3 Central Tracking Volume

At DØ , tracking is employed to measure the trajectory of charged particles in a radius ≈ 75 cm around the beam pipe. These trajectories curve in the plane of the uniform magnetic field produced by the solenoid according to their charge and momentum

$$R = \frac{p_T}{|q|B_T} \tag{4.3}$$

making it possible to determine the charge and momentum of a particle by measuring its radius of curvature.

Effort is made to reduce the amount of material that induces particles to convert their energy into the bifurcating cascades of particles known as showers. Showers in the tracking volume not only obscure the trajectory of the originating particle, but result in a dumping of energy in the solenoid, where it cannot be measured. Thus the tracker is built out of materials such as silicon, acrylic, and carbon fiber, which have long radiation and nuclear interaction lengths.

4.3.1 Silicon Microstrip Tracker [15]

The SMT, sometimes called the Silicon Vertexing Tracker, is the innermost detector in the DØ system (Figure 4.4). The SMT was designed to be able to resolve the highly colinear tracks within jets, as well as cluster the track origins so well as to be able to resolve multiple vertices. Vertex resolution is important in assigning the "physics" coordinate system to an event. The very fine resolution of the SMT can assist in b quark identification through precise measurement of secondary vertex positions. For example, b quarks are produced in top quark decays, and give rise to B mesons which travel a short distance before decaying.

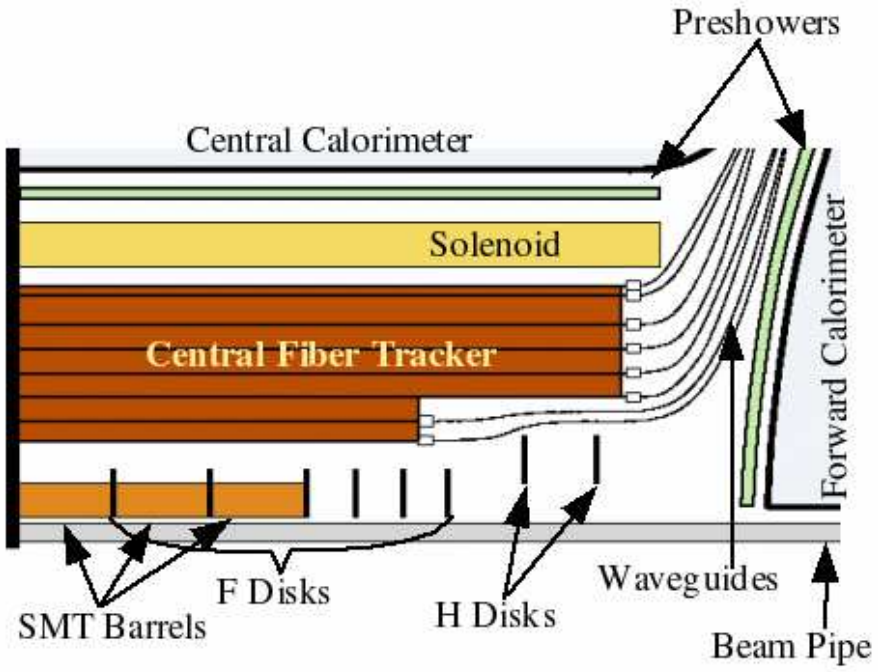

Figure 4.4. Arrangement of the SMT, CFT, solenoid and preshower tracking elements of the DØ central tracking volume. Shown here is one longitudinal quadrant.

The location of this decay is measurable as a secondary vertex, and is evidence of the presence of a b quark in the event.

The SMT surrounds the interaction region. Beam collisions are most likely to occur at the center of the detector, however, the typical width of the interaction "point" extends 25 cm in the z direction. To detect charged particles emanating from a collision not at the center of the detector, the SMT has a hybrid design.

It is difficult to build the SMT such that all particles' tracks are perpendicular to the detector, due to the extended interaction point. The solution is to build barrel detectors to measure primarily the $r - \phi$ coordinate, and disk detectors to measure $r - z$ as well as $r - \phi$. At high values of η, vertices for particles are reconstructed in three dimensions by the disks, and at small η the vertices are

determined by the barrels. The detector has six barrels along the z-axis, with four detector layers per barrel. There are twelve small diameter double-sided "F" disks, and four large diameter single-sided "H" disks. Four F disks are placed between barrels, except at $\eta = 0$. The remaining eight are placed at the ends of the barrels. The H disks sit at the furthest distance from $z = 0$, approximately 1.2 m away, and allow coverage out to $\eta \approx 3$. During the data-taking period used for this analysis, the H disks were not used.

The barrels and F disks are composed of 300 μm-thick silicon microstrip detectors. In all, the SMT has approximately 800,000 individual strips. This allows a spatial resolution of approximately 10 μm, and the pattern recognition necessary to reconstruct tracks inside jets.

4.3.2 Central Fiber Tracker [16]

Exterior to the SMT, the CFT trades spatial resolution for reduced materials and fiscal budgets. In the region covered by the CFT, 19.5-51.5 cm from the center of the beam pipe, there is increased spatial separation of tracks, so hit resolution can be reduced without significantly altering the track resolution. The active component of the CFT–scintillating optical fiber–is cheaper and significantly less dense than the silicon used in the SMT.

The CFT has 77,000 channels of 835 μm optical fiber completely covering 8 concentric carbon-fiber support cylinders occupying the radial space from 20 to 50 cm. The two innermost support cylinders extend to $z = \pm 83$ cm, the remaining cylinders to $z = \pm 126$ cm. The pseudorapidity coverage for hits is a function of cylinder (see Table 4.1); the coverage for tracks is said to be $|\eta_{det}| < 2.0$.

TABLE 4.1

CFT CYLINDER PROPERTIES

Cylinder	Radius (cm)	Length (cm)	$\lvert\eta_{det}\rvert$ (single hit)	Stereo Layer $u = +3^o$, $v = -3^o$
A	19.5	166	2.1	u
B	23.4	166	2.0	v
C	28.1	252	2.2	u
D	32.8	252	2.1	v
E	37.5	252	1.9	u
F	42.1	252	1.8	v
G	48.8	252	1.7	u
H	51.5	252	1.6	v

The pseudorapidity coverage for hits in the CFT is a function of cylinder radius and length. Alternating the stereo angle improves the z resolution by providing a veto angle double the individual angle.

The fiber material used in the CFT are of two forms: scintillating and clear. The mechanical structure of the two types of fiber are identical: a 770μm polystyrene core surrounded by claddings of polymethylmethacrylate and fluoro-acrylic. This gives a refractive index structure of 1.59-1.49-1.42, and traps 5.3% of point source light by total internal reflection (as opposed to 3.1% in similar single-clad fibers).

The polystyrene core of the scintillating fiber has been doped with two materials, paraterphenyl (PTP) and 3-hydroxyflavone (3HF), that serve to convert ionizing radiation to an optical signal. PTP enhances the ionization structure of the polystyrene, but emits light at a wavelength (λ = 340 nm) that is readily reabsorbed. The 3HF absorbs this light and reemits it at a longer wavelength (λ

= 530 nm) that can be propagated over 5 m of scintillating fiber and 10 m of clear fiber.

The scintillating fibers are arranged in "doublet ribbons" (Figure 4.5) of 256 channels. One layer of doublets is mounted axially (parallel to the beam) on the support cylinders. A second doublet layer, mounted in alternating stereo layers of $\pm 3^o$ constrains the z position of track hits, providing for 3-D tracking. Each scintillating fiber is mated via an optical connector to a clear fiber waveguide (Figure 4.8) which pipes the scintillation light to a Visible Light Photon Counter (VLPC) (Figure 4.9).

The VLPC is a silicon-avalanch device that has approximately 80% quantum efficiency, and a gain of at least 20,000. The VLPC operate at around 10 K to reduce the background from electronic noise, and have a rate capability of at least 10 MHz.

The VLPC are mounted on readout boards, where the signal is sampled by a discriminator called the SIFi Trigger (SIFT) chip. The VLPC signal is also simultaneously sent to a Silicon VerteX (SVX) chip and to the CFT trigger system. This signal is stored in the SVX chip within a analog pipeline until a trigger decision is made or 32 beam crossings have occurred since the signal was produced. If the trigger system issues an accept, then the SVX digitizes the signal and reads it out.

The CFT participates in the trigger system primarily as a background veto, though implementation of track-based tau triggers is ongoing. Coincident hits in the eight axial layers are required to form a trigger track. These tracks are typically combined with trigger information from other subdetectors to determine if an event should be written to tape. The very short readout and recovery interval

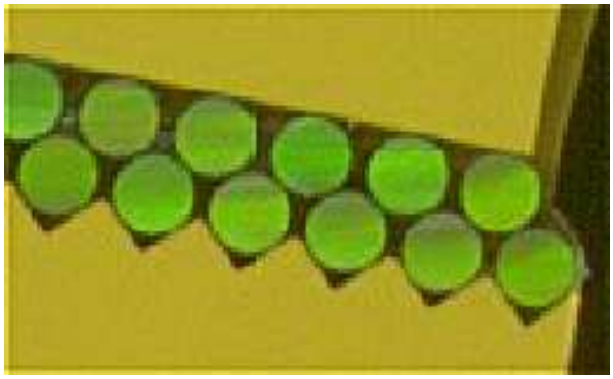

Figure 4.5. Close-up end view of a scintillating fiber doublet ribbon. Each 830 μm fiber's position must be known to an accuracy better than 50 μm.

of the scintillator allows for implementation of the track trigger at Level 1, the first and fastest element in the triggering heirarchy.

4.3.3 Preshower Detectors [17, 18]

The central and forward preshower (CPS and FPS) detectors are designed to occupy minimal volume while distinguishing between electrons and charged pions and improving the energy resolution of electromagnetic particles. Most particles, including electrons, begin to shower in the solenoid mass. Muons and charged pions do not, but the pions quickly shower in the calorimeter, mimicking electrons. This pionic background can be removed by requiring there be energy deposition in the preshowers, which are located between the solenoid and the calorimeter (see Figure 4.4).

While counted part of the tracking system because they share a readout electronics system with the CFT, the preshower detectors are closer in design to a sampling calorimeter (Section 4.4). A thickness of lead tapered to produce uni-

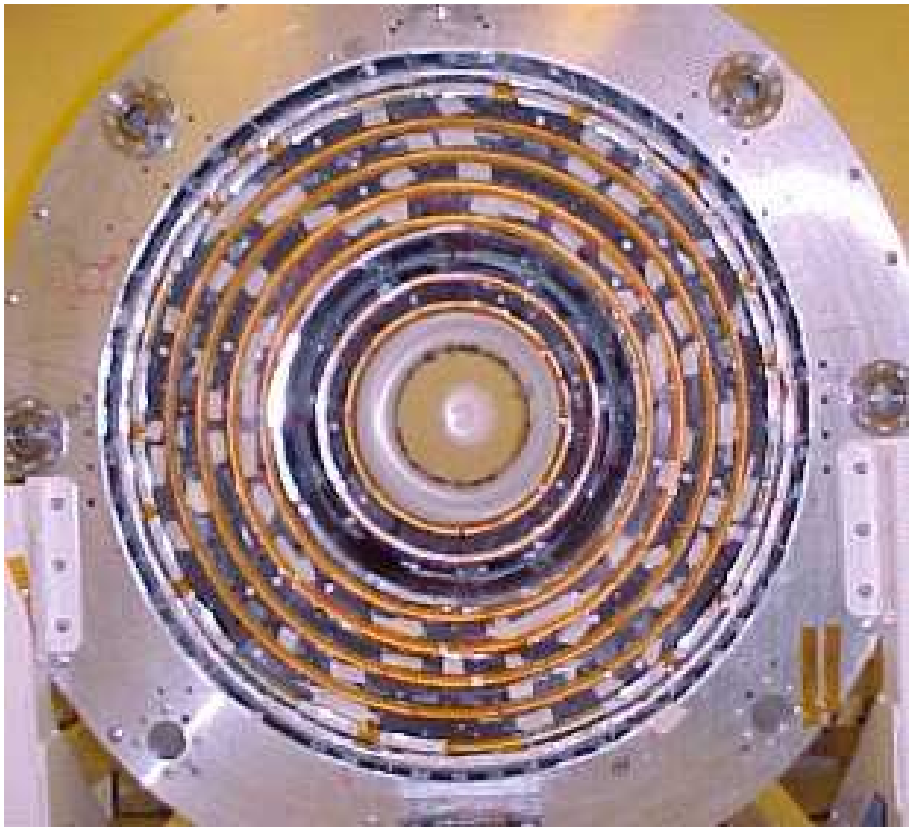

Figure 4.6. End view of the DØ central fiber tracker.

Figure 4.7. The CFT was constructed remotely and then inserted into the DØ detector, inside the calorimeter.

Figure 4.8. After installation, the clear fiber waveguides were connected to the scintillating ribbons and routed out of the detector volume to a nearby electronics platform, where they were attached to the VLPC cassettes. The author participated in this installation, and is pictured here in the background.

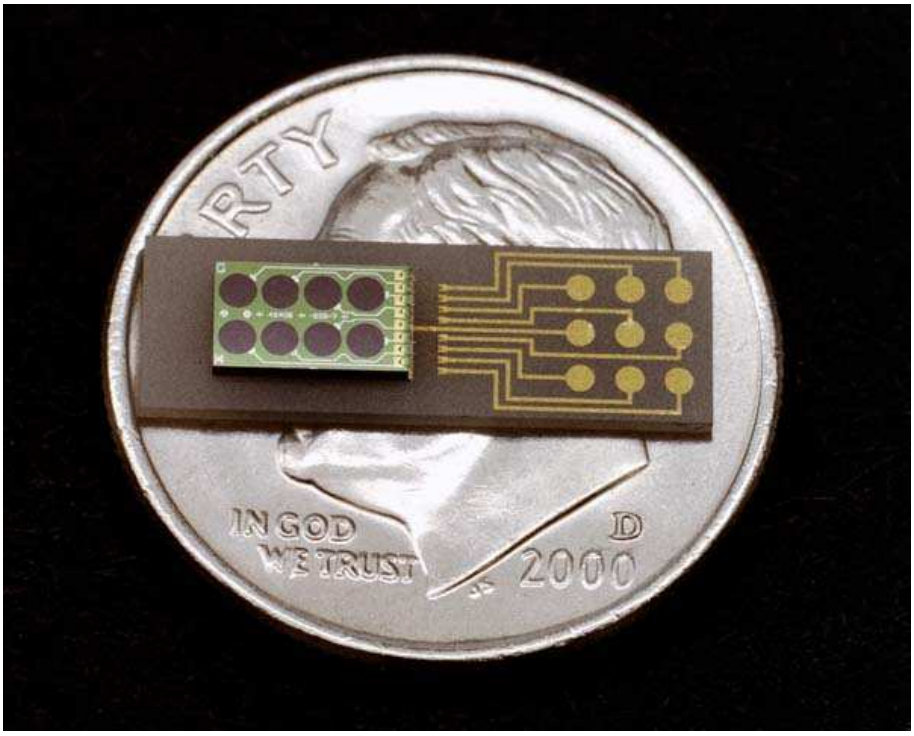

Figure 4.9. Each VLPC has eight channels. The circles on the left are mated to the waveguides, those on the right provide electronic readout.

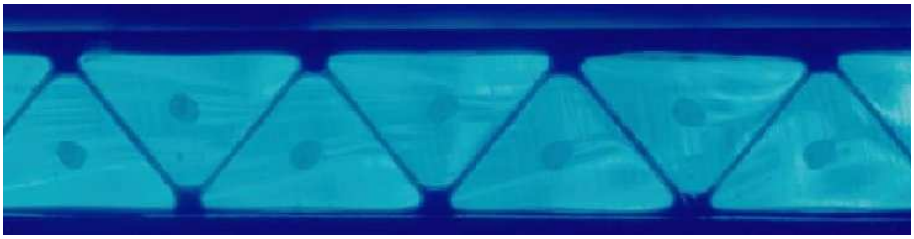

Figure 4.10. The preshower scintillator is a triangular strip embedded with a waveshifting optical fiber. The position resolution of this design is finer than that of a similar design using square strips because of energy sharing between adjacent strips.

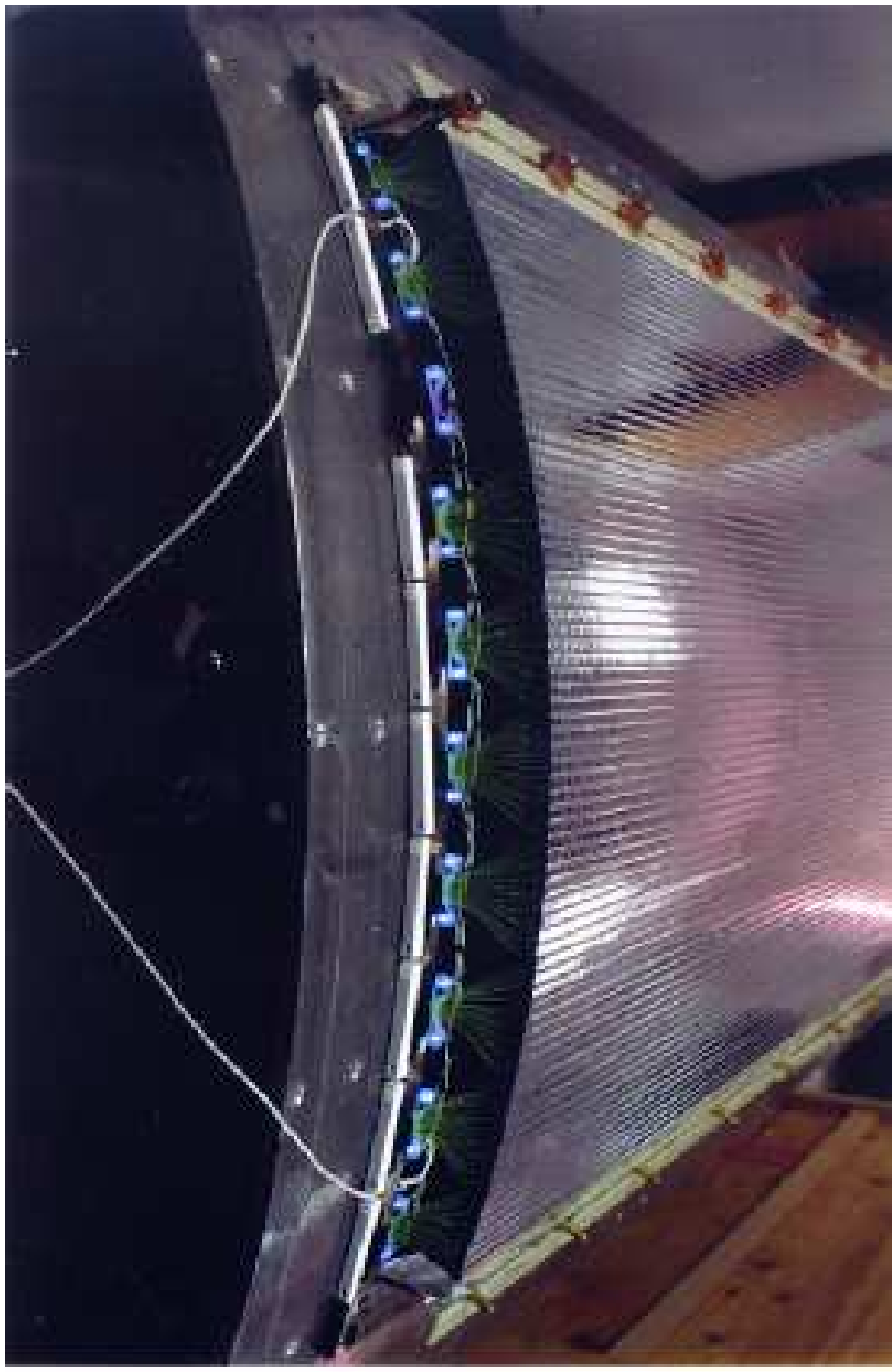

Figure 4.11. A portion of the DØ central preshower detector, a thin cylindrical detector designed for pion rejection.

form materials density at all pseudorapidities induces showers that are registered in a volume of scintillator.

The scintillator is in the form of strips whose triangular cross-section has a base of 7 mm and a 1 mm hole containing a single wavelength-shifting optical fiber. The strips are arranged in a sawtooth manner to form a plane (Figure 4.10).

The CPS consists of three planes of scintillator nestled in the 51 mm gap between the solenoid coil and the central calorimeter cryostat to form a cylinder. The three layers are mounted in axial, u and v configurations much like the ribbons of the CFT, but with a stereo angle of 23^o. The CPS has a radius of approximately 72 cm, covering the region $|\eta| < 1.2$.

For the FPS, the scintillator planes are combined into u-v doublets. Two of these doublets are mounted to the inner faces of each of the end calorimeter cryostats, providing coverage to the regions $1.4 < |\eta| < 2.5$.

Readout of the preshowers is the same as readout of the CFT. Preshower information is incorporated into the CFT trigger system.

4.4 Calorimetry [19, 20]

The calorimeter is designed to accurately measure the energy of particles by inducing them to shower, and then sampling the energy the shower deposits. Modules composed of heavy-material absorber sandwiching alternating layers of active and readout material (Figure 4.14) are stacked into towers along lines of constant η_{det}. Though only a fraction of a shower's energy is deposited in the active material, successive sampling of the shower energy is used to infer the total

Figure 4.12. Installation of the DØ calorimeter.

energy of a particle. The shape and radial location of energy deposition is relevant to establishing the identity of the originating particle.

4.4.1 Particle Showering

Electrons entering the calorimeter interact with the absorber plates through the Bremsstrahlung mechanism, in which they emit a photon as they pass through the Coulomb field of a nucleus in the absorber. Photons interact predominantly via pair production, when a photon converts into an electron-positron pair in the

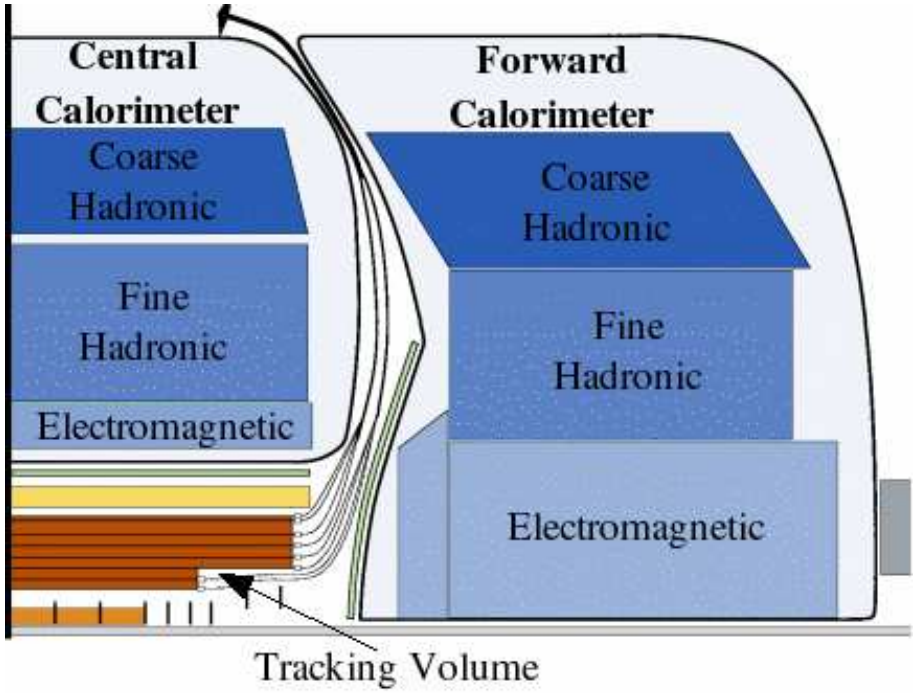

Figure 4.13. Schematic of one longitudinal quarter of the DØ calorimeter. The calorimeter is housed in three cryostats; each cryostat holds electromagnetic, fine hadronic, and coarse hadronic layers.

vicinity of a nucleus. The secondary particles emitted in these interactions can undergo these same interactions themselves. This process, called an electromagnetic (EM) shower, repeats itself until the energies of all the secondary particles fall below the threshold for pair production. The particles will then continue to lose energy, mainly through ionization. Electromagnetic showers have a shape that fluctuates within comparatively narrow limits; the width of the shower scales with the radiation length of the intervening material.

Hadronic particles lose energy in the calorimeter mainly through inelastic collisions with atomic nuclei. The secondary particles produced in these collisions can also lose energy through inelastic collisions. This process is called a hadronic shower. Though hadronic showers generally have an electromagnetic component,

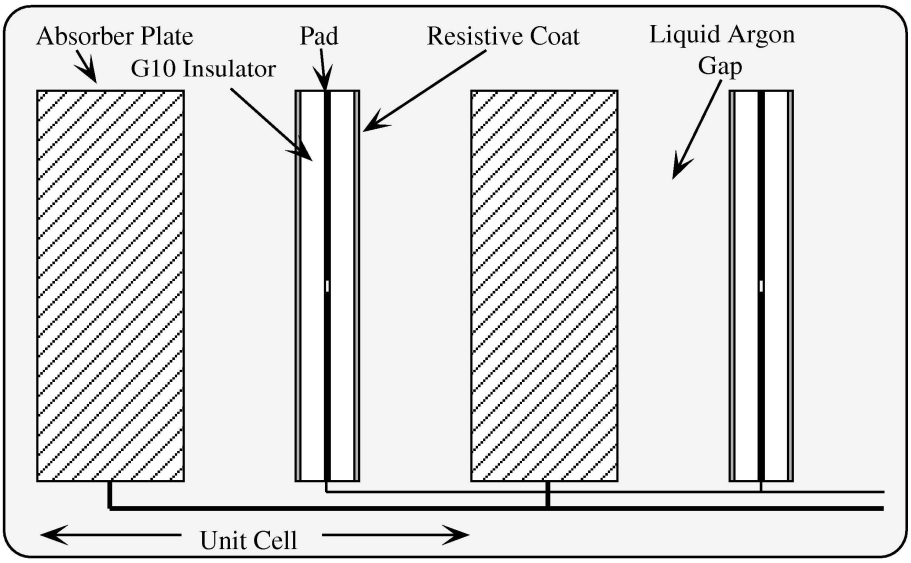

Figure 4.14. A DØ calorimeter cell with alternating layers of absorber plates, liquid argon, and signal boards. Many cells form the layers of the calorimeter. Absorber plates can vary in size, but the gap between the absorber plate and the signal board is always 2.3 mm.

they are a function primarily of the nuclear interaction length of a material. Thus they tend to be spatially diffuse, and to contain them, calorimeters need to extend beyond what is necessary to contain EM showers. These additional layers of calorimetry are specifically designed to encourage nuclear interaction.

4.4.2 The DØ Calorimeter

The DØ calorimeter is virtually hermetic to all particles but muons and neutrinos. Each of electromagnetic, fine hadronic and coarse hadronic sampling calorimetry is housed in three cryostats:a cylinder for the central region (CC, $|\eta_{det}| < 1.2$) and curved disks for the end regions (EC, $1.3 < |\eta_{det}| < 4.5$). The sampling material is liquid argon, which is dense, radiation-hard, and reliable; providing a uniform, linear response.

The functional components of the detector are defined by segementation and absorber material. The electromagnetic modules use depleted uranium, the fine hadronic modules use depleted uranium with 1.7% niobium, and the coarse hadronic modules use copper or stainless steel. In addition to its effectiveness as a compact absorber, the uranium equalizes response to EM and hadronic interactions because it will fission when hit with slow neutrons.

Energy sampling is done by grounding the absorber plates and maintaining a voltage approximately 2 kV on the copper pads on the signal boards. Charged particles passing through the liquid argon ionize electrons in the argon. The ionized electrons are drawn across the potential difference to the signal boards, where they induce a signal on the copper pad. This signal is proportional to the amount of energy lost by the originating particle as it ionized the argon.

The signal is carried out of the detector via coaxial cables to preamplifiers and signal shaper electronics and then split and sent down two different paths. One path goes the Level 1 calorimeter trigger. The other path leads to the baseline subtraction system (BLS). The BLS function is to clean and remove noise from the signal before it is sent to be digitized. Subtracting the baseline from the current signal reduces noise caused by long time constants intrinsic in some of the electronics used within the calorimeter. Following a trigger decision, output from the BLS is read out and digitized by Analog-to-Digital Converters (ADC). This digital signal is merged with signals from other detector systems and used to form an event.

4.4.3 Intercryostat and Massless Gap Detectors

Between the CC and EC the calorimeters, in the region of $1.1 < |\eta| < 1.4$, there is a large amount of uninstrumented material. Cryostat walls, calorimeter support, and cabling for the detector readout constitute the majority of this material. To instrument this region, scintillation detectors have been mounted on each face of the EC cyrostat walls. Each intercryostat detector (ICD) is made of 384 scintillating tiles each of size $\Delta\eta = \Delta\phi = 0.1$, which exactly matches the calorimeter cells. Additionally, there are separate single calorimeter-like readout cell structures, called massless gaps, installed in both the EC and CC calorimeters. In combination, the ICD and massless gap detectors provide a good approximation to the standard calorimeter readout.

4.5 The Muon System [21–23]

As described in section 4.4.2, the DØ calorimeter is not hermetic to muons. Energy loss by bremsstralung radiation in muons is limited by their mass, which is about 200 times that of the electron. Muons will ionize detector media, producing a signal in the tracking and calorimetry, but this low energy loss absorption process is not enough to fully deplete the muon of its energy. Detectors specialized to the detection and measurement of muons are constructed exterior to the calorimeter, forming the outermost layer of the DØ detector.

There are three major components making up the DØ Muon system, as shown in Figure 4.15. The Wide Angle MUon Spectrometer (WAMUS), covering a range of $|\eta| < 1$, is complemented by the Forward Angle MUon Spectrometer (FAMUS), covering a range of $1 < |\eta| < 2$. A solid iron toroid magnet producing a 1.8 Tesla field provides magnetic tracking for momentum measurement of muons.

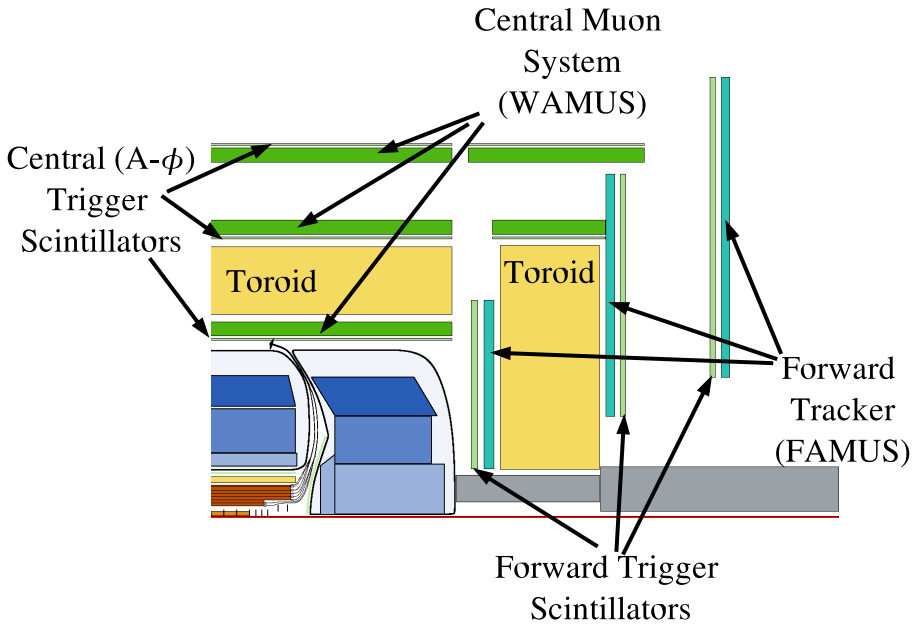

Figure 4.15. Schematic of one longitudinal quarter of the DØ muon system.

The toroid is a remnant of Run I design: there was no magnetic field in the central tracking region, so the sole muon momentum measurement was done using the toroid. Now the muon momentum is predominantly found using the upgraded central tracking system, but the muon system toroid stills allows for an independent measurement. In the future, combining momentum information from the toroid with that from the central tracking systems may further improve the overall momentum measurement for muons at DØ.

4.5.1 The Central Muon System

The WAMUS consists of three detection layers, increasing radially outward and labeled with the convention: A, B and C. Layer A resides between the calorimeter and the toroid magnet, while the B and C layers are positioned outside the toroid.

Figure 4.16. Construction of the muon forward trigger scintillators.

A combination of proportional drift tube (PDT) chambers and scintillators make up each layer within the WAMUS. The PDT chambers are constructed of extruded aluminum tubes of varying size, with the largest being around 250×575 cm^2. Each chamber consists of three to four decks of tubes, four decks for the A-layer and three decks for the B-layer and C-layer. Tubes are 10.1 cm across and 5.5 cm high, with around twenty-four tubes making up a chamber. Inside each tube is an anode wire at its center which runs the length of the tube. These anode wires are oriented along the magnetic field lines in order to provide a position measurement for momentum determination. Besides the wire, two vernier pads, along the top

and the bottom of the tube, are used as cathodes. Each tube is filled with a non-flammable gas mixture of 80 percent argon, 10 percent CH_4 and 10 percent CF_4. At the operational voltage of 2.5 kV for the pads and 5.0 kV for the wire, the drift velocity in this gas is about 10 cm/μs, with a maximum drift time of 500 ns. Hit position uncertainty due to diffusion in this gas is around 375 microns.

Scintillators for the WAMUS are broken up into two categories, the A-ϕ counters and the Cosmic Caps. The A-ϕ counters cover the A-layer PDTs. They are segmented in ϕ slices of 4.5 degrees having a length of around 85 cm along the z direction. Each scintillator slice is embedded with a wavelength-shifting fiber coupled to a photo-multiplier tube (PMT), which is used for readout. These scintillators have a timing resolution of $\sim$4 ns. This fast signal is used for triggering and rejecting out-of-time muons from cosmic rays and backscattered particles from the forward regions.

The Cosmic Cap scintillators are located outside the B-layer and C-layer PDTs. This covers the top, sides, and part of the bottom of the muon system. As with the A-ϕ scintillators, the Cosmic Cap scintillators are read out with a WLS and PMT system. Cosmic Cap scintillators' time resolution is $\sim$5 ns, which can be improved by offline corrections to 2.5 ns. This provides a fast signal used to identify cosmic ray muons. Together with the A-ϕ counters, this signal gives a timestamp determining which beam crossing the muon is associated with.

4.5.2 The Forward Muon Tracking Detectors

The FAMUS consists of three layers, again called A, B and C. Each layer is made up of a combination of Iarocci mini-drift tube (MDT) sections and scintillation pixel counters (Figure 4.16). The MDT sections are made up of three to four

planes of tubes, four planes for the A-layer and three planes for the B-layer and C-layer. Each plane is divided into eight octants and consist of tubes, each having eight cells. The individual cells have an internal cross-sectional area of 9.4×9.4 mm^2 and each contain a 50 μm tungsten-gold anode wire. A gas mixture of 90 percent CF_4 and 10 percent CH_4 is used in the MDT cell. With this mixture of gas and a cathode voltage of 3.1 kV a maximum drift time of near 60 ns is achieved. The position resolution in the drift plane for this configuration is around 0.7 mm.

Mounted on the face of each of the MDT layers are single planes of scintillator, called the pixel counters. Each plane is divided into eight octants with each octant consisting of ninety-six tiles of scintillator (Figure 4.16). The pixel counters have a ϕ segmentation of 4.5 degrees with a η segmentation of 0.12 for the outer nine rows and 0.07 for the inner three rows. Just as with the WAMUS scintillators, the FAMUS pixel counters are readout with a WLS and PMT system.

Stacks of 50 cm thick iron and 15 cm thick polyethylene are skinned in 5 cm of lead form sheilding around the accelerator beam pipe in the forward region ($2.5 < |\eta| < 3.6$) behind the EC cryostat wall. The shielding was designed to reduce backgrounds from interactions of the beam with the quadrupole magnets and beam pipe by a factor of two to four.

4.6 Neutrino Detection

With the inclusion of the muon system, only one type of particle escapes the DØ detector unmeasured: the neutrino. Neutrinos do not interact electromagnetically, and their lack of mass provides a very small weak force coupling. They simply do not interact with matter enough to provide any sort of reliable detection.

However, their presence and energy may be inferred by their absence. The $p\overline{p}$ collisions at Fermilab have no transverse net energy. Conservation of energy requires that the transverse energies of the particles resulting from the collision also sum to zero. Since neutrinos exit the detector, taking their energy with them, an initial vector sum of energy deposition will be unbalanced. The vector required to balance the sum is called "missing transverse energy" (MET or $\not\!\!E_T$). A large $\not\!\!E_T$ vector indicates the presence a neutrino, and is used as an estimate of its transverse mass.

CHAPTER 5

THE DØ TRIGGER AND DATA ACQUISITION SYSTEMS [24, 25]

Even if it were technologically feasible, recording all 1.7 MHz Tevatron events is not entirely desirable. Most events are not relevant to the physics being studied at DØ . As uninteresting events simply consume resources that could be applied elsewhere, it is best they be discarded as quickly as possible. Technological considerations define "as quickly as possible" as "less than 13 μs," though only about 0.05% of events are allowed to make it past the first .4 μs.

Decisions about whether an event is discarded is made by the DØ triggering system, which is a three-tier pipelined, buffered system. The first tier (level 1) processes fast detector pick-off signals in a hardware/firmware based system to reduce the event rate to about 1. 5kHz. The second tier (level 2) uses information from level 1 and forms simple physics objects to reduce the rate to about 850 Hz. The third tier (level 3) uses full detector readout and event reconstruction on a filter farm to reduce the rate to 20-30 Hz. The Trigger Framework coordinates information between subdetectors and triggers.

The DØ trigger menu contains a wide variety of triggers. While the emphasis is on triggering on generic lepton and jet final states, there are also trigger terms for specific final state signatures.

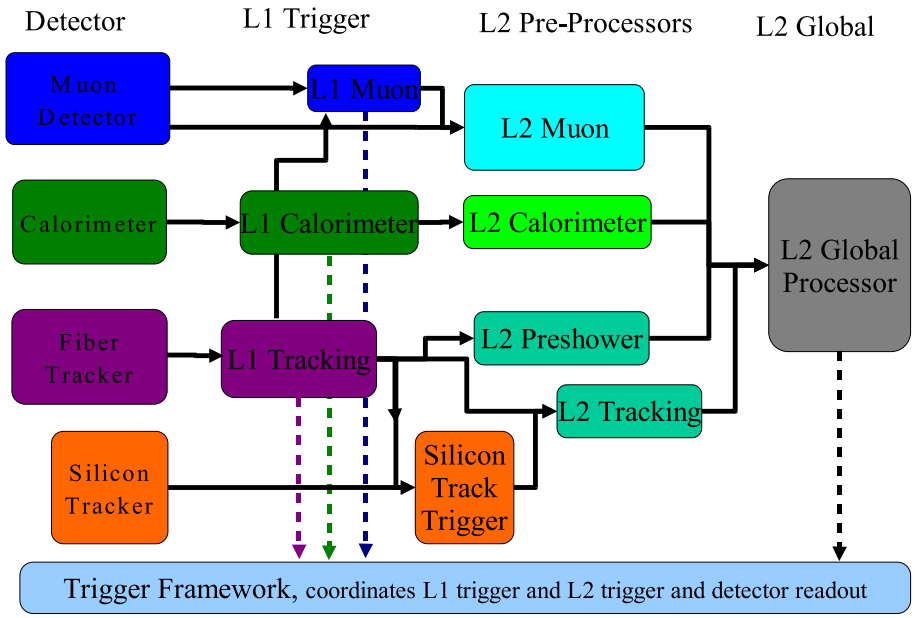

Figure 5.1. A schematic illustration of Level 1 and Level 2 trigger systems. Adapted from [24].

5.1 Level 1 and Level 2 Trigger System

Neither Level 1 nor Level 2 triggers require readout from the entire detector. At Level 1, the triggers from various subdetectors are independent, developing raw data in parallel, except for the ability to match muons to central tracks. These subdetector-specific trigger objects are combined at Level 2 into simple physics objects. Level 2 can also compute some simple event-wide variables, such as the total transverse energy E_T and ϕ separation between objects. A schematic representation of the Level 1- and 2 trigger flow is shown in Figure 5.1.

5.2 Level 3 Trigger System and Data Acquisition

If a Level 2 Trigger accept is issued, the DØ detector is read out. This includes reading out all of the detector elements as well as the trigger Level 1 and

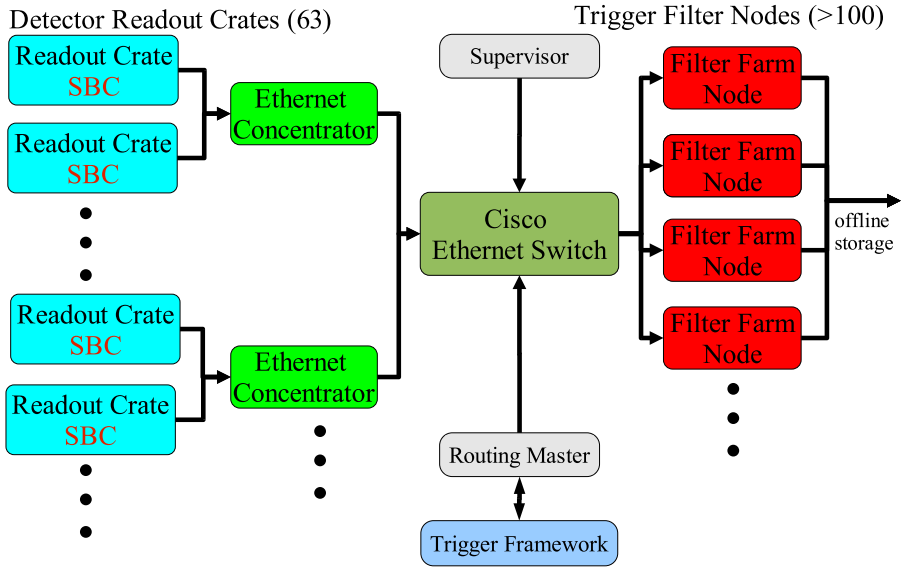

Figure 5.2. A schematic illustration of DØ Level 3 trigger system. Adapted from [24].

Level 2 systems themselves. This information is piped into the Level 3 Trigger, an overview of which is shown in Figure 5.2.

The hit and pulse height information from each detector readout crate is collected in single-board-computers (SBC), which send this information to a PC node on the filter farm through a commercial Ethernet switch. The flow of information from the readout crates to the filter nodes is controlled by the routing master. The trigger programming is loaded onto the filter nodes by the supervisor node. The routing and filter node programming occurs over the same Ethernet links that are used in the data transfer.

Each event is fully reconstructed at Level 3 with algorithms that are similar to those used in the offline event reconstruction. This allows the Level 3 system to accomplish a large rejection factor of 20 that is required to limit the output rate to less than 50 Hz.

The flexibility of the trigger programming is expanded further at level 3. There are 256 individual trigger bits available at level 3, each coupled to one of the level 1/level 2 triggers. Each can be programmed to filter on combinations of simple objects such as electrons, muons, or jets, as well as event-wide variables and correlations. Level 3 also provides the ability to select b-tagged jets based on tracking and silicon detector information.

Upon Level 3 accept, the data that has been buffered in the PC farm is transfered to Fermilab's Feynman Computing Center to be permanently stored on magnetic tape drives.

CHAPTER 6

DATA RECONSTRUCTION

Once an event has fired a trigger, the electronics have been read out, and the output of the electronics written to tape, it is then necessary to process the output from a million electronics channels into, among other things, tracks, jets, muons and EM objects. A complete description of the reconstruction process is well beyond the scope of this thesis. Much more information is available from the Run II Software Algorithms website at http://www-d0.fnal.gov/computing/algorithms/. The treatment here is to give an overview at the most general level.

6.1 Reconstruction Algorithms

Reconstructing raw electronics data into the higher-level objects that form the physics event is done in several hierarchical steps. First, unpackers specific to each subdetector process the raw data by unpacking individual detector data blocks. They decode the raw information, associate electronics channels with physical detector elements and apply detector specific calibration constants. For many of the detectors, this information is then used to reconstruct cluster (for example, from the calorimeter and preshower detectors) or hit (from the tracking detectors) objects. These objects use geometry constants to associate detector elements with physical positions in space.

The second step in the reconstruction focuses on the output of the tracking detectors. Hits in the silicon (SMT) and fiber tracker (CFT) detectors are used to reconstruct global tracks. This is one of the most CPU-intensive activities of the reconstruction, and involves running several algorithms. The results are stored in corresponding track chunks

The track chunks are used as input to the third step in processing, vertexing. First, a primary vertex, which establishes the coordinates of $p\overline{p}$ interactions is located. The primary vertex is essential to the calculation of various kinematic quantities. Then secondary vertices, which are displaced because they are associated with the decays of long-lived particles, are identified.

Finally, particles are assembled from these reconstructed objects. This step produces the objects most associated with physics analyses and is essential for successful physics results. Using a wide variety of sophisticated algorithms, information from each of the preceding reconstruction steps are combined and standard physics object candidates are created. First the reconstruction algorithm finds electron, photon, muon, neutrino ($\not\!\!E_T$) and jet candidates, which are based on detector, track and vertex objects. Finally, using all previous results, candidates for heavy-quark and tau decays are identified.

6.2 DØ Software

All of the software required to reconstruct the data is developed by the DØ Collaboration on an ongoing basis. The official DØ Software programming language is C++, though there are some remnants of the Run I standard Fortran, "wrapped" to interface with the DØ Framework.

TABLE 6.1

MAIN COMPONENTS OF DØ SOFTWARE RELEASES

DØGSTAR and DØSIM	Full detector simulation
PMCS	Fast detector simulation
TRIGSIM	Simulates the response of the trigger system; for use with data or Monte Carlo
RECO	Processes electronic signals into physics objects stored in various formats
TMBfixer	Re-reconstructs events from events reconstructed into the thumbnail format
DØcorrect	Calls all the post processing codes (corrections, certifications) for EM, muon, jet and $\not\!\!E_T$

The DØ Framework is an object-oriented founded system for linking independently developed components into a coherent whole. The framework defines how data flows through the components, and provides a standard interface for adding modules.

While individual users may compile DØ Code in any configuration and with any modifications they wish, periodically official binary executables will be compiled. These official releases include executables for the programs in Table 6.1.

Every year or so, a new one of these releases is selected to provide the reconstruction code for all new data.

CHAPTER 7

MONTE CARLO

"Monte Carlo" is defined in very general terms as a problem-solving technique based on the use of random numbers and probability statistics.

In high energy physics, the technique is most often used to simulate particle interactions and detector response. This analysis uses a Monte Carlo simulation to produce asymmetry distributions from the theoretical Parton Distribution Functions.

In general, high energy Monte Carlo simulations have three main components: production, decay, and detector response. In the production phase, the hadronic interaction (the cross section) is modeled. This is where the PDF come in: it is critical to know the momentum distribution of the partons to accurately calculate the cross section.

Since most interesting particles are identified by their decay products, it is necessary to model how the particle decays into those products. In the case of W boson decay, this is where the V-A distribution comes into play. Particle generation and decay are often modeled together in a single program.

Even the decay products, though, are not observed in their "true" form. The detector is neither 100% hermetic nor 100% efficient. Particles may be incident on non-hermetic gaps and go undetected. Tracks may be measured improperly

because of the hit resolution, etc. The detector simulation attempts to model all of these inefficiencies.

In this analysis, the data are compared to PDF using the generator ResBos-A with detector simulator PMCS[1]. Monte Carlo generated by Pythia and smeared using DØGSTAR and DØsim is also used for the measurement portions of this analysis. All of these programs are described below.

7.1 Generators

Selection of a Monte Carlo generator is based on purpose and speed. Some generators can be adapted to model a wide range of processes, but they are the behemoths of high energy Monte Carlo generators: big and slow. Their generalized nature usually means they provide a lot of information unneccessary to the task at hand, which consumes storage and analysis resources. Often, a generator specific to the relevant process will be faster and retain only the most pertinent information.

7.1.1 ResBos-A

The event generator (and decay propagator) chosen for the PDF comparison portion of this analysis is ResBos-A, which is an extension of ResBos, Monte Carlo for RESummed BOSon Production and Decay. It was written and is maintained by Csaba Balazs and C.-P. Yuan at the Department of Physics and Astronomy, Michigan State University[26].

ResBos computes the fully differential cross section for processes $h_1 + h_2 \rightarrow B(+X) \rightarrow l_1 + l_2(+X)$ where the h are hadrons, the B a boson, the l leptons,

[1]For details see Appendix B.

and the X hadronic recoil. Production can be made at leading order (LO) or with next-to-leading order (NLO) QCD corrections, or with soft-gluon resummed initial state QCD corrections included.

The ResBos-A modification improves on the phase integration methods of ResBos, and incorporates NLO final state corrections.

PDF input into ResBos-A is made by incorporation of grid files[2] generated using a code called Legacy, also written by C. Balazs, and C.-P. Yuan, with G. Ladinsky, P. Nadolsky. For more information on Legacy, see [27].

Grid files compatible with ResBos-A are available for CTEQ and MRST collaboration PDF. The most recent PDF available for $\sqrt{s} = 1.96$ TeV are CTEQ6.1M and MRST(2004)[28]. Also available are the grid files to model the $1-\sigma$ error on CTEQ6.1M.

For each of MRST(2004) and the CTEQ6.1M central value, 25 million events were generated. For each of the 40 CTEQ6.1M error PDF, 5 million events were generated.

7.1.2 Pythia

Developed by the Lund University theory group beginning in 1978, Pythia is a well-established general-purpose generator [29]. In addition to modeling hadronic interactions, Pythia may be used to model leptonic and lepton-hadron interactions. Pythia contains theory and models for a number of physics aspects, including hard and soft interactions, parton distributions, initial and final state parton showers, multiple interactions, fragmentation and decay.

[2]Grid files are essentially spreadsheets that encode the theoretical cross section under different production scenarios.

Pythia events used in this analysis were generated by the DØ Monte Carlo Production group [30] for the Collaboration. Event sets consist of 247500 $Z \rightarrow e^+e^-$ events and 500k $W \rightarrow \tau\nu$ events.

7.2 Detector Simulations

At DØ, detector simulation is done in one of two ways: full and fast. The full simulation uses a complex detector map to simulate energy deposition and electronic response. These individual channel responses are then built into analysis objects in the same way (and with the same code) as the actual detector responses are.

Alternately, a simulator can take the output of the generator and build idealized analysis objects, which are then smeared. The smearing is "tuned" such that relevant Monte Carlo distributions match those produced in data. This method is much faster, but because it is performed on high-level objects, it is generally not convenient to process the Monte Carlo into the data format.

7.2.1 PMCS

PMCS, the Parameterized Monte Carlo Simulation, has been developed "in house" by the DØ Collaboration, with the University of Maryland group taking the lead. While PMCS can be configured to provide a full simulation suitable for use in the data reconstruction programs, priority is put on maintenence and development of the fast simulation configuration. It is the fast simulation that is used in this analysis.

PMCS is available as official DØ released code. The Electroweak (WZ) working group has developed a variation of the release that is specifically tuned to the

electrons from W boson decays, wz_epmcs. Detector simulation of the ResBos-A Monte Carlo is done with the latest version (v01-00-34) of the wz_epmcs package. Since the efficiency $\times$ acceptance is expected to cancel in Equation (2.22), only the following three effects are applied in the detector simulation:

- Electron energy resolution and scale
- Missing transverse energy resolution and scale
- Vertex Z smearing

7.2.2 DØGSTAR and DØsim

Full simulation of Monte Carlo at DØ is done by DØGSTAR and DØsim.

DØGSTAR is a wrapper for GEANT, a CERN-maintained program that describes the passage of elementary particles through matter. DØGSTAR determines how much energy is deposited in the active areas of the detector.

DØsim simulates the electronics response to the energy deposition determined by DØGSTAR. It also handles pileup of any additional minimum bias interactions that occur in the same beam crossing as the signal event.

Pythia Monte Carlo produced by the DØ Monte Carlo Production group has been processed with DØGSTAR and DØsim.

CHAPTER 8

EXPERIMENTAL TECHNIQUE

The $W \rightarrow e\nu$ signal, an electromagnetic object and $\not\!\!E_T$, is not pure. Events with similar topologies contaminate the sample set; these background events must be corrected for when measuring W boson properties.

The largest sources of background contamination come from $W \rightarrow \tau\nu$ events where the τ decays to an electron; $Z \rightarrow ee$ events; and QCD events. It will be shown in Section 8.6 that the $W \rightarrow \tau\nu$ and $Z \rightarrow ee$ backgrounds are too small to alter the asymmetry measurement. QCD events provide significant background contamination and must be compensated for. This analysis uses a technique called the Matrix Method to statistically estimate this background.

8.1 The Matrix Method

The Matrix Method gets its name from its use of matrix reduction of independent equations. Consider a sample of events, N_{tot}, that is a mixture of signal, N_{sig}, and background events, N_{bkg}:

$$N_{tot} = N_{sig} + N_{bkg}. \tag{8.1}$$

Here N_{tot} represents an observable, the number of events that pass a particular set of selection criteria.

Suppose there is a cut, d, that provides significant discrimination between signal and background events. Signal events will pass the cut with some efficiency, ε_d, which should tend toward 1. The background events will also pass this cut with some efficiency, f_d, which should tend toward 0. The number of sample events that pass this cut, N_d, is of course the sum of the signal and background events that pass the cut:

$$N_d = \varepsilon_d N_{sig} + f_d N_{bkg}. \tag{8.2}$$

If ε_d and f_d are known, these equations are easily solved for N_{sig} and N_{bkg} using simple substitution or matrix reduction.

In separating W boson signal from QCD background, tracking provides a good discriminating variable. The QCD events that contaminate the W boson sample are events where one of the two hadronic jets has been reconstructed as an electron. Whereas a "real" high-P_T electron is expected to have a high-P_T track associated with it, the "fake" electrons from QCD are not. Equations 8.1 and 8.2 become

$$N_{tot} = N_{trk} + N_{notrk} = N_e + N_{QCD} \tag{8.3}$$

and

$$N_{trk} = \varepsilon_{trk} N_e + f_{trk} N_{QCD}. \tag{8.4}$$

In this thesis, ε_{trk} will be referred to as the *tracking matching efficiency* or just *tracking efficiency*, and f_{trk} as the *fake track rate* or *fake rate*.

The asymmetry measurement requires an extension of this method. In addition to resolving N_{tot} into N_e and N_{QCD}, N_e must be resolved into N_{e^+} and N_{e^-}. This

transition from two unknown variables to three unknown variables requires the addition of a third independent equation:

$$N_{tot} = N_{e^+} + N_{e^-} + N_{QCD} \tag{8.5}$$

$$N_{trk^+} = \varepsilon_{trk^+} N_{e^+} + f_{trk^+} N_{QCD} \tag{8.6}$$

$$N_{trk^-} = \varepsilon_{trk^-} N_{e^-} + f_{trk^-} N_{QCD}. \tag{8.7}$$

where f_{trk^+} is the probability that a positive track be associated with the fake electron and ε_{trk^+} is the probability for matching a positive track with an electron. It does not, however, represent the probability for matching a positive track with an *positive* electron. Thus equations 8.6 and 8.7 are valid only in the case that charge assignment is perfect. At DØ it is not.

Therefore, a third efficiency variable, g, is introduced. This variable is called in this thesis the *charge misidentification rate* or *charge misid*. Charge misid can turn a positive track negative (g_{+-}) or a negative track positive (g_{-+}).

Charge misidentification represents a migration of events between 8.6 and 8.7. Every positive electron assigned a negative charge will appear in the sample N_{trk^-} and *not* appear in the sample N_{trk^+}.

Thus equations 8.6 and 8.7 become:

$$N_{trk^+} = \varepsilon_{trk^+}(1 - g_{+-}) \cdot N_{e^+} + f_{trk^+} \cdot N_{QCD} + \varepsilon_{trk^-} g_{-+} \cdot N_{e^-} \tag{8.8}$$

and

$$N_{trk^-} = \varepsilon_{trk^-}(1 - g_{-+})\cdot N_{e^-} + f_{trk^-}\cdot N_{QCD} + \varepsilon_{trk^+} g_{+-} \cdot N_{e^+}. \quad (8.9)$$

There is no reason to believe that the DØ detector is not charge symmetric such that $f_{trk^+} = f_{trk^-}$, etc. Argument for this position is made in Section 8.5. Here, by assumption, $\varepsilon_{trk^+} = \varepsilon_{trk^-} \equiv \varepsilon$, $g_{+-} = g_{-+} \equiv g$ and $f_{trk^+} = f_{trk^-} \equiv f$, and the equation set can be solved directly for the asymmetry

$$A(y_e) = \frac{N_{e^+} - N_{e^-}}{N_{e^+} + N_{e^-}} = \frac{\varepsilon - f}{\varepsilon(1 - 2\cdot g)} \cdot \frac{N_{trk^+} - N_{trk^-}}{(1-f)\cdot(N_{trk^+} + N_{trk^-}) - f \cdot N_{notrk}} \quad (8.10)$$

where all variables are a function of y. Note that the transformation $N_{tot} = N_{trk}+N_{notrk}$ has been made to preserve the statistical independence of the samples.

8.2 Event Selection

The events used in this analysis are from data collected between run 161973 (August 2002) and run 194566 (June 2004). The data were processed with various builds of p14 RECO into thumbnails [31]. The thumbnails were fixed with version p14.fixtmb.01 or p14.fixtmb.02 of TMBfixer as appropriate [32]. RECO thumbnails preselected by the Common Sample Group to contain at least 1 electron-like object [33] (1-EMLoose skim) were converted to "tuple" format by DØ code wz_analyze version v01-01-03 and DØcorrect version v8 [34].

Runs tagged "BAD" by the SMT, CFT, CAL, or MET subgroups in the offline run database [35] and luminosity blocks declared bad by the JET/MET group [36] or luminosity group [37] have been removed as the data were analyzed. The integrated luminosity for the sample is approximately 300pb^{-1}.

8.2.1 Trigger

Events selected are required to have passed a single electron trigger. The efficiency of the triggers used has been studied in detail for the precision measurement of the W cross-section[38].

The triggers selected for the event samples are single-EM and required to be unprescaled on a run-by-run basis. There is a preference for loose triggers, but because these are often prescaled, tighter triggers are frequently used. Below is the heirarchy of preference of single-EM triggers:

Trigger list global_CMT_8 to 11(runs $\leq$ 178721):

- EM_HI_SH or EM_HI_2EM5_SH
- EM_HI_SH
- EM_HI
- EM_MX_SH
- EM_MX.

Trigger list global_CMT_12 (runs $\geq$ 178722):

- E1_SHT20, E2_SHT20, E3_SHT20 or E1_SH30
- E1_SHT20, E2_SHT20 or E1_SH30
- E1_SHT20 or E1_SH30
- E1_SHT20

For runs $<$ 174845, Level 1 trigger coverage is limited to $|\eta_{det}| < 2.4$. This has a significant effect on the statistical power of the asymmetry measurement at

high rapidity, as approximately 20% of the data were collected in this run range. Level 1 coverage has since been extended to $|\eta_{det}| = 3.2$. Level 3 coverage was extended from $|\eta_{det}| < 3.0$ to $|\eta_{det}| < 3.6$ with the global_CMT_12 trigger set. The restricting factor remains the Level 2 trigger, with a trigger acceptance of $|\eta_{det}| < 3.0$.

Because of the variability of the acceptance, possible acceptance edge effects, and the difficulty in measuring the efficiency in the far forward region, many analyses are restricted to using a subset of the available triggers. This analysis benefits greatly from symmetry: if the trigger system behaves the same for positrons and electrons for a region of the detector, that region is usable.

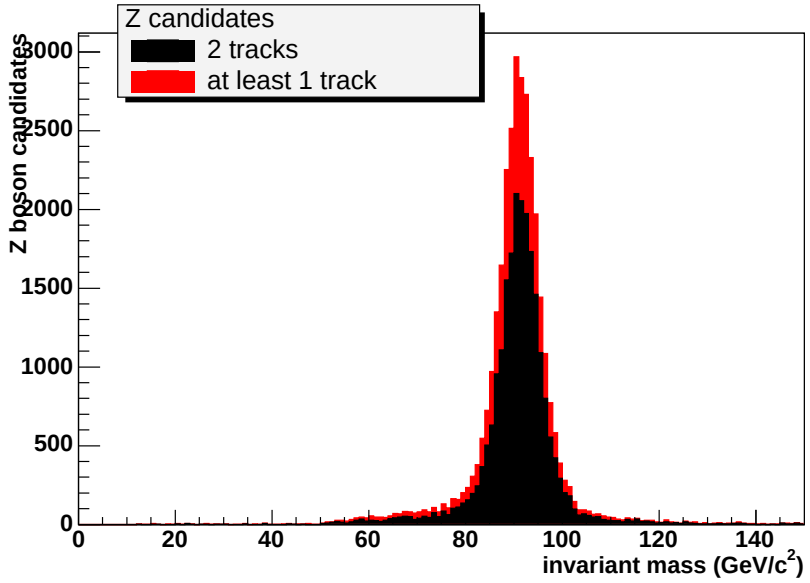

Figure 8.1. Di-electron invariant mass.

8.2.2 Data samples

- Dielectron/Z candidates: The P_T spectrum of electrons from Z bosons is similar to the P_T spectrum of electrons from W boson decays, thus $Z \rightarrow ee$ events, which can be fully reconstructed, provide an excellent sample for measuring the detector and reconstruction algorithm performance. Di-electron events are required to have two electron candidates with $P_T > 25.0$ GeV/c and have a di-electron invariant mass M_{ee} such that: $70\text{GeV}/c^2 < M_{ee} < 110\text{GeV}/c^2$. The invariant mass spectrum is shown in Figure 8.1. Spectra are presented for an event selection requiring two loose electrons where at least one electron candidate also passes the tight selection criteria and an event selection requiring two tight electrons.

- Jet + electron/QCD candidates: Background studies require event samples enriched in "fake" electrons. This selection comprises mainly of QCD di-jet events where one jet has been misidentified as an electron. This sample consists of events with one very well defined jet (as described in Table 8.1) and one electron back-to-back in ϕ. The transverse momentum of the jet is required to be no more than twice that of the electron candidate. A cut on the missing transverse energy, $\not\!\!E_T < 10$ GeV, is used to reduce the contamination from real W boson to electron decays in the sample.

- Single electron + $\not\!\!E_T$ /W candidates: This is the analysis signal sample. Events are required to have one electron with $P_T > 25.0$ GeV/c and missing transverse energy $\not\!\!E_T > 25.0$ GeV. Figure 8.2 shows the transverse mass distribution for this sample.

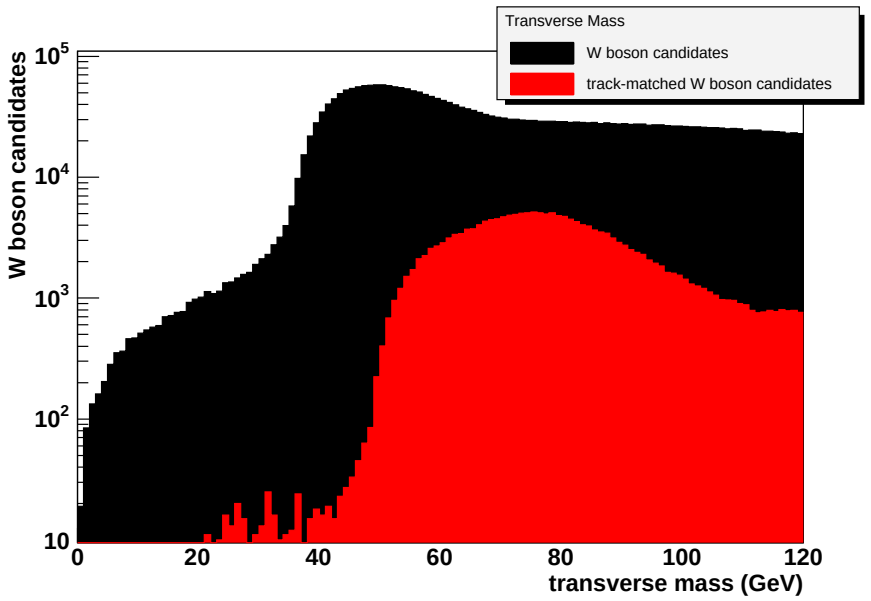

Figure 8.2. Transverse mass of $W \rightarrow e\nu$ candidates with and without a track match. Relaxation of the track match requirement significantly increases the contamination from QCD background/

8.2.3 Object Identification

Definitions of all objects are consistent with those used in the W/Z group to measure the W cross section [38] and summarized in Table 8.1.

This analysis uses the electron selection criteria proposed by the EMID group. In order to be identified as an electron a calorimeter object must pass the quality cuts in Table 8.1.

QCD candidates are characterized by having a single loose electron back-to-back in ϕ with a jet. Jets are identified using the $R = 0.7$ cone algorithm and pass the criteria establised by the Jet-ID group[36].

TABLE 8.1

PHYSICS OBJECT QUALITY CUTS

Calorimeter (loose) electron	Track-matched (tight) electron	Jet
ID = 10 OR ± 11	Loose electron quality and kinematic cuts	$N90 > 1$
EMFraction > 0.9	Track match probability $P(\chi^2) > 0.01$ with E_e/P_T^{trk} element in the CC	0.05 < EMFraction < 0.7
Isolation < 0.15	At least 1 SMT hit	CHF < 0.25
H-Matrix(7) < 12 for CC or H-Matrix(8) < 20	$(P_T)_{trk} > 15.0 GeV/c$	Jet7_hotf <= 5
$E_T > 25$ GeV		F90 < 0.65
Problematic areas of the calorimeter, as described in [38], are removed		$E > 25$ GeV
$\|\eta_{det}\| < 1.1$ OR $1.5 < \|\eta_{det}\| < 3.2$		

8.3 Tracking Efficiency

The tracking efficiency is a convolution of the track finding efficiency and the efficiency for matching found tracks to a calorimeter based electron candidate. It is best described by saying that ε is the probability that a real calorimeter electron will have a track matched to it.

The tracking efficiency is measured using a "tag and probe" method, where the tag is a calorimeter electron and the probe is whether a track was matched to it. To ensure that "real" electrons are tested, the dielectron ($Z \rightarrow ee$) sample set is

used. However, non-Z contributions are significant in the subset of the dielectron sample in which both electrons go unmatched. To eliminate this contamination of the sample and remain unbiased, each electron is tested separately, with the requirement that the non-test electron have a track matched to it. Electrons that fail the probe condition (N_{fail}) and electrons that pass the probe condition (N_{pass}) are binned in rapidity in separate histograms such that for a pure $Z \rightarrow ee$ sample,

$$\varepsilon = \frac{N_{pass}}{N_{pass} + N_{fail}} \tag{8.11}$$

While the *pass* sample is pure (see Figure 8.3), recent analyses ([38]) have shown that a dielectron sample in the Z mass peak in which only one of the electrons is required to have a track contains significant QCD contamination. Events in the *fail* sample all have exactly one track match, and so can be expected to contain background contamination, which systematically reduces the measured tracking efficiency.

Background subtraction is performed bin-by-bin in rapidity, using an exponential as the background distribution hypothesis. The dielectron invariant mass spectrum is fit with a Gauss×Breit-Wigner+exponential function using Minuit (Figure 8.4). The fit is required to converge and have a $\chi^2/\text{dof} < 3.0$.

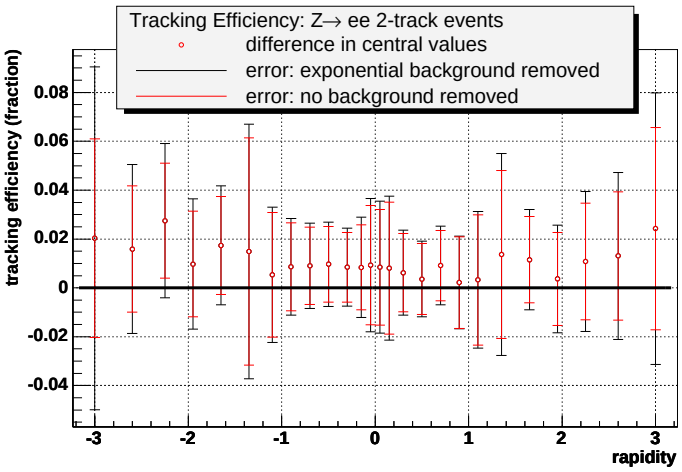

Figure 8.3. A study of background subtraction in the dielectron + 2-track event sample. The tracking efficiency is measured twice: first with background subtracted from both the *pass* (2-track) and $fail$ (1-track) samples; then with background subtracted only from the $fail$ sample. Circles represent the difference between the two measurements; the bars represent the total error associated with each measurement. Background subtraction of the *pass* sample can only reduce the N_{pass}/N_{fail} ratio, so it produces a systematic reduction in the tracking efficiency. However, subtracting the background introduces more uncertainty than it removes.

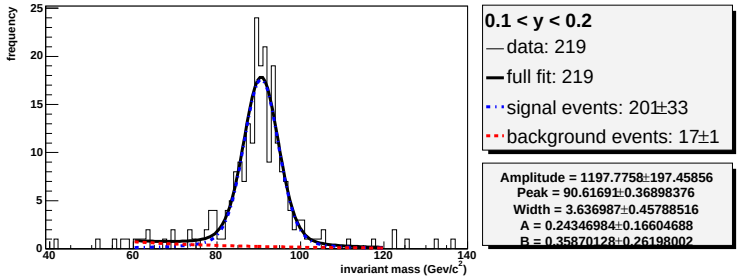

(a)

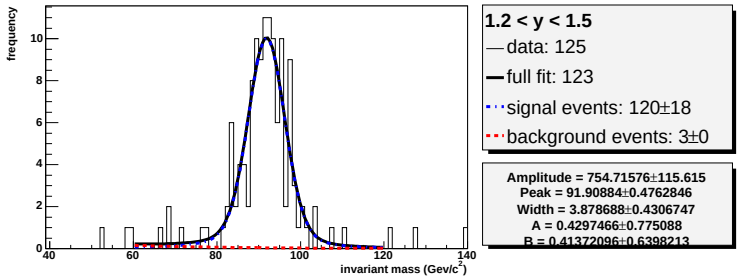

(b)

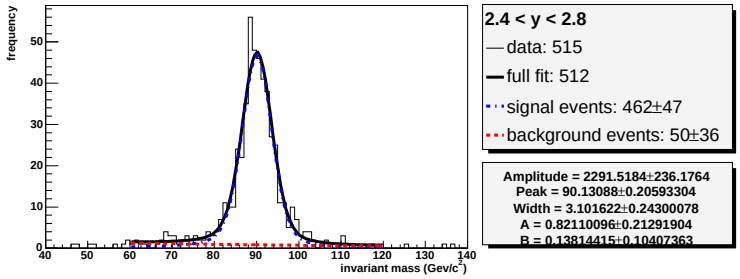

(c)

Figure 8.4. The invariant mass spectrum of the $Z \rightarrow ee$ *fail* sample in three rapidity bins: (a) is in the central calorimeter and expected to have very little background; statistics are reduced in (b) because it is in the vicinity of the calorimeter gap; (c) is a very forward rapidity bin. The parameters *amplitude, peak* and *width* describe the signal shape. The number of signal events is calculated by integrating this shape over the fit range.

The number of signal events is determined by integrating the Gauss×Breit-Wigner function using the parameters determined by the fit. The error on this number is taken from the error matrix produced by the fitter. This error combines both statistical and systematic effects.

Once the *fail* sample has been purified in this manner, Equation 8.11 is valid and the resulting track matching efficiency is shown in Figure 8.5. The error bars depicted in this figure demonstrate the combined statistical and systematic errors assessed on the measured efficiency.

To test the validity of using an exponential background shape, the background subtraction was repeated using a straight line assumption. The difference between the two methods is insignificant when compared with the error derived from the fit (Figure 8.6), so it is not included as a separate systematic error.

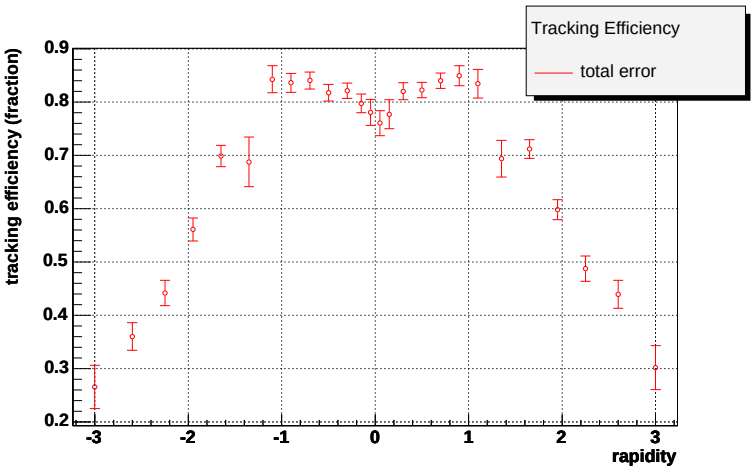

Figure 8.5. Tracking efficiency for electrons vs electron rapidity. The errors shown are a convolution of statistical and systematic errors.

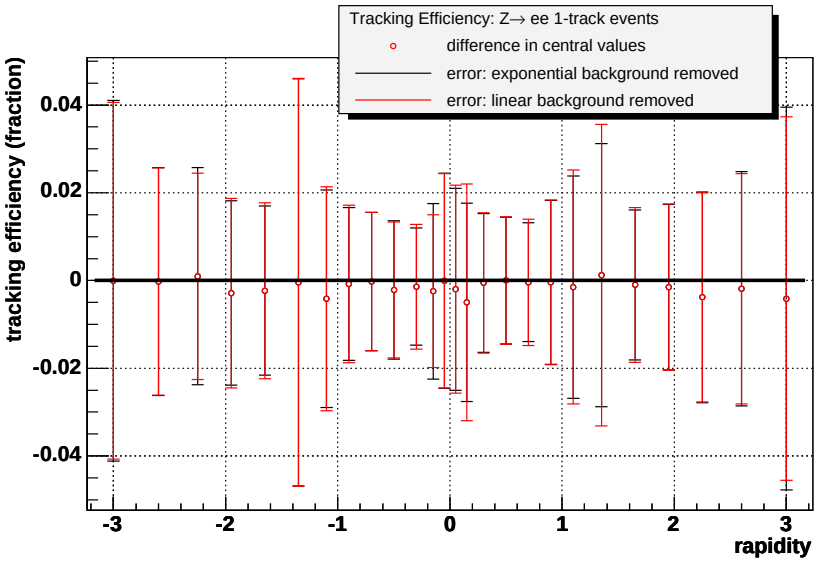

Figure 8.6. Similar to the study explained by Figure (8.3), here the difference between exponential and linear background subtraction in the *fail* sample is explored. The difference between the two methods is small compared to the error on either method.

8.4 Charge Misidentification Rate

The abililty to determine the charge of the lepton limits the quality of the asymmetry measurement. The charge of the electron is determined by the curvature of its matched track. The misidentification of the charge comes primarily from two sources: energetic electrons leaving "straight" tracks and processes that generate a "kink" in the track, such as photon emission and multiple scattering.

In the region of greatest interest to this analysis, the very forward region of the detector, track reconstruction is poorest. This is related to the decreasing acceptance of the tracking system and the decreasing arc length of the track in

the forward region that leads to a higher error on the curvature measurement. Furthermore, the dead material density is the greatest in this part of the detector, enhancing Bremsstrahlung radiation.

Since misidentification of the charge represents a doubling effect (a misidentified electron is removed from the electron distribution *and* added to the positron distribution) it is critical that it be well-understood.

Charge misidentification is measured in the $Z \rightarrow ee$ sample where both electrons are matched with tracks. As discussed in Section 8.3, the "doubly-tracked" sample is very pure, so no background subtraction is required.

Typically it would be sufficient to determine if the tracks are like or opposite charged, but because we are binning in rapidity and the charge misidentification rate is highly dependent on the rapidity, it is necessary to determine which of the electrons' charge was reconstructed incorrectly. This suggests a tag-and-probe method, where the probe is required to have a charge opposite to that of the tag. This only provides a meaningful measurement if the charge of the tag has a high probability of being correct.

Monte Carlo provides the best prospect for studying the charge misidentification rate, as the "true" charge of the electron is known.

Beginning with a sample of 247k Pythia $\rightarrow$ GEANT $Z \rightarrow ee$ events, the generated charge (q_{gen}) and reconstructed charge (q_{reco}) of the individual electrons were compared to measure the "true" charge misidentification rate:

$$g_{true} = \frac{N(q_{reco} \neq q_{gen})}{N(q_{reco} \neq q_{gen}) + N(q_{reco} = q_{gen})} \tag{8.12}$$

The charge misidentification rate is measured in data by comparing the measured charge of the two electrons in $Z \rightarrow ee$ events using a "tag and probe" method.

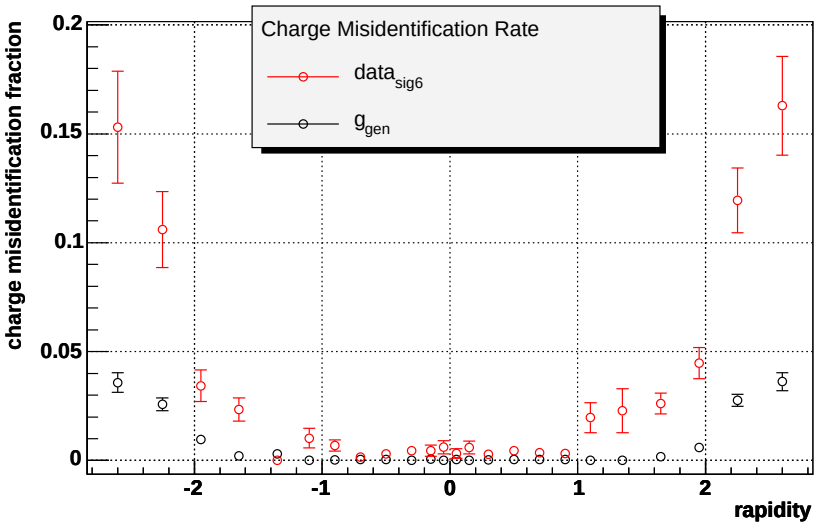

Figure 8.7. The charge misid rate measured in data and in 247k Pythia $Z \rightarrow ee$ events vs rapidity. Charge misidentification is not well modeled by the Monte Carlo, especially in the forward regions of the detector.

To eliminate biases and increase statistics, each of the electrons are, in turn, used as the "tag". The measured charge of the tag (q_{tag}) is presumed correct and opposite that of the probe (q_{probe}) such that

$$g_{data} = \frac{N(q_{tag} = q_{probe})}{N(q_{tag} = q_{probe}) + N(q_{tag} \neq q_{probe})} \tag{8.13}$$

Figure 8.7 compares g_{true} and g_{data}. It is clear that these distributions diverge rapidly as $|y|$ increases. Varying the cuts on the tag electron varies the magnitude of the effect, but only by a few percent. In fact, this is a documented feature of the GEANT simulation [40]. Neither the single-cluster resolution nor the materials budget are well-modeled, resulting in an underestimation of the charge misidentification from both tracking resolution and "kink" events.

It is expected, however, that a tag and probe method that accurately measures the underlying distribution g_{true} can accurately measure the underlying "true" distribution in data, even if that distribution is not the same in Monte Carlo and data. To select a method, the Monte Carlo was re-analyzed using the tag and probe method and the cuts on the "tag" leg were varied. The variations are summarized in Table 8.2. Results are found in Figure 8.8.

It was found that while g_{lopt} and g_{hipt} tend to overestimate g_{true}, and g_{cc} underestimates g_{true} at high rapidity, g_{sig} describes the underlying distribution well throughout the entire rapidity range. Thus this is selected as the method for measuring the misidentification rate in data. The systematic error is determined by calculating the misid rate in data using the best (g_{sig}) and worst (g_{lopt}) method, and quoting the difference in the central values as the error. The final misidentification rate with statistical and systematic errors in shown in Figure 8.9.

TABLE 8.2

TAG LEG CONDITIONS IN MONTE CARLO STUDY OF MISID

Variation	**Condition**	**Agreement with g_{true}**
g_{lopt}	The electrons are ordered in P_T. Only the electron with the lower P_T is allowed to be the tag.	POOR
g_{hipt}	The electrons are ordered in P_T. Only the electron with the higher P_T is allowed to be the tag.	POOR
g_{cc}	Both electrons are allowed to be the tag, with the requirement $\|\eta_{det}\| < 1.1$.	MODERATE
g_{sig}	Both electrons are allowed to be the tag, with a significance of curvature cut as described in Section 8.4.1.	GOOD

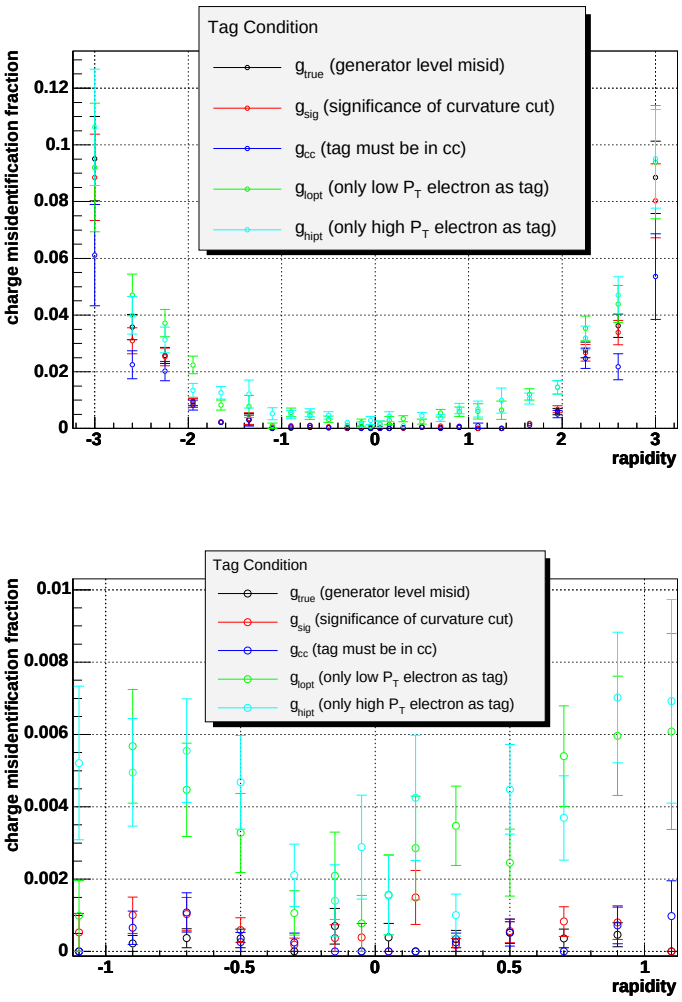

Figure 8.8. The charge misidentification rate measured in Monte Carlo, using four different conditions on the tag electron, and compared to generator-level information over (a) the entire rapidity range and (b) central rapidities. Using the low P_T electron as the tag condition clearly performs the worst when compared to the generator level information.

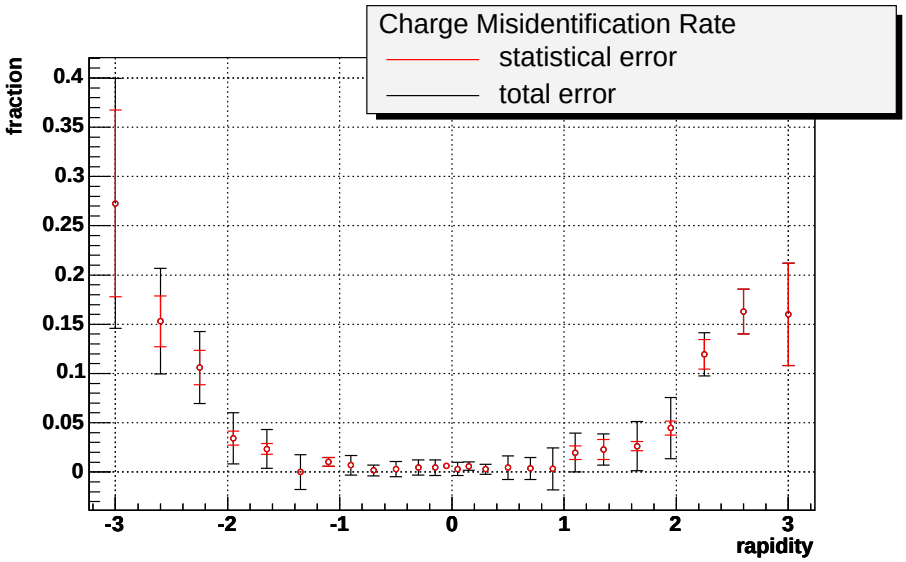

Figure 8.9. Charge misid rate vs electron rapidity.

8.4.1 Significance of Curvature

The charge of the electron is determined by the curvature of its track match, defined as the signed inverse of the radius of curvature:

$$C \equiv \frac{q}{R} \propto \frac{q \cdot B_T}{P_T} \tag{8.14}$$

The magnetic field B and the curvature of the track C are measured, so typically the quantity $\frac{q}{P_T}$ is calculated. Since P_T is a physical quantity that is always positive, the charge of a track is equal to the sign of the curvature. The ability to distinguish between positive and negative charged tracks is predicated on the ability to determine track curvature.

The curvature of a track is measured by fitting an arc parameterized by chord length and arc height. The distribution of the position errors of the clusters is gaussian, thus these errors propagate to the error on the curvature as a standard deviation, σ_C, through Equation 8.14. Of interest in this study is the case where a small error in the measurement of the curvature can lead to a discrete error in the assignment of the charge, around $C = 0$ ($P_T = \infty$).

$$N = \frac{C - 0}{\sigma_C} \tag{8.15}$$

Assuming Gaussian errors, if $N > 3$, the chance that the charge has been asigned incorrectly is 2%. Studies of the significance of curvature show that setting the cut at $N > 1$ was nearly as effective as harder cuts, yet to err on the side of caution - and attempt to avoid the problems of non-gaussian tails in the curvature - a significance cut of $N > 6.0$ was made.

8.4.2 Fake track matching rate

The fake track matching rate is determined using the jet+electron sample described in Section 8.2.2 above. Figure 8.11 shows the missing transverse momentum distribution for the jet+electron sample and the W candidate sample.

The fake rate, f, is simply defined as the ratio $f = N_{trk}/N_{cal}$, where N_{cal} is the number of events where a loose electron candidate was reconstructed and N_{trk} is the number of events where a loose electron was also matched to a charged track.

The cut on missing transverse energy, $\not\!\!E_T$ < 10GeV, removes a significant fraction of real W boson contamination in the background sample. However, the cut is chosen rather arbitrarily. As shown in Figure 8.10, the fake rate varies significantly ($\approx 50\%$) with the $\not\!\!E_T$ cut in the range $\not\!\!E_T$ < 30 GeV. Above 20

GeV, the increase is likely due to inclusion of real electrons. The spread in the range 5 GeV $< \not{E}_T <$ 15GeV is quoted as a systematic error. Figure 8.12 shows the measured fake rate in bins of lepton rapidity with statistical and systematic errors displayed.

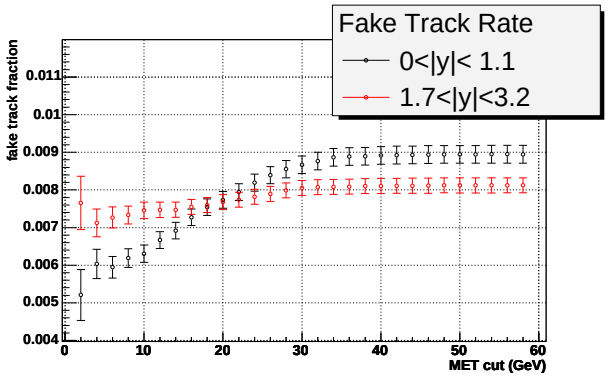

(a)

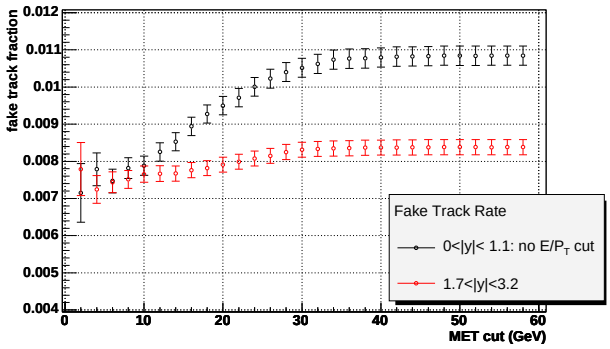

(b)

Figure 8.10. Fake track rate vs $\not\!\!E_T$ cut separately for the central and forward calorimeters. (a) uses the standard track matching algorithm, which includes an E_T/P_T element in the central region. That the CC distribution dips below the EC distribution at low $\not\!\!E_T$ suggests that the inclusion of the E_T/P_T element reduces the incidence of fake tracks. This interpretation is supported by (b): the feature disappears when the cut is removed. Additionally, it can be seen in plot (a) that the fake rate in the forward region is much more stable, suggesting that an E_T/P_T element is not required.

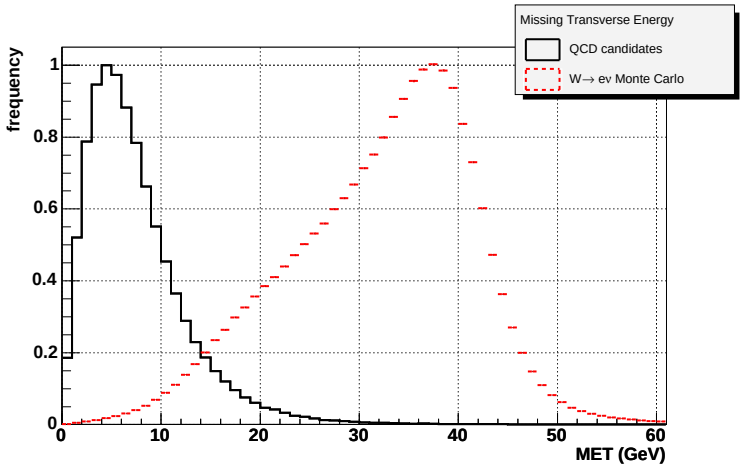

Figure 8.11. $\not\!\!E_T$ distribution for the jet+electron and *wenu* Monte Carlo samples. Distributions are peak-normalized to unity. A cut of $\not\!\!E_T < 10.0 GeV$ on the background candidate sample removes most $W \rightarrow e\nu$ signal events.

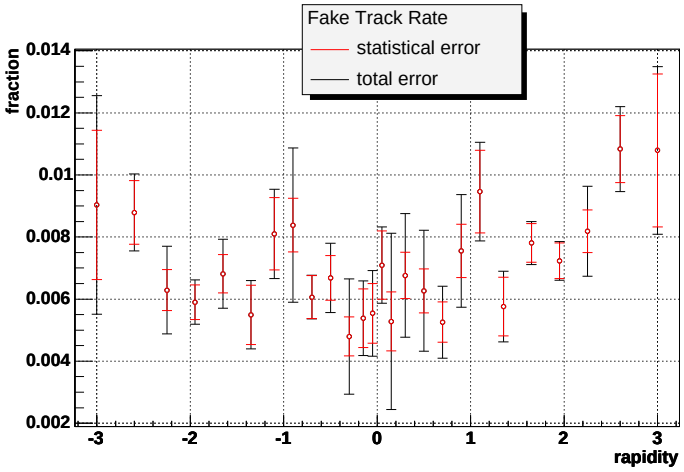

Figure 8.12. Fake track rate vs electron rapidity.

8.4.3 Application of the Matrix Method

Figure 8.13 shows the Matrix Method-measured asymmetry with statistical and total errors.

Figure 8.14 shows the effect of Matrix Method corrections on the "raw" asymmetry. Here the "raw" asymmetry refers to the the charge asymmetry in the $W \rightarrow e\nu$ *candidate* sample:

$$A_{raw}(y) = \frac{N^{+}_{cand} - N^{-}_{cand}}{N^{+}_{cand} + N^{-}_{cand}}. \tag{8.16}$$

As expected, in the very central region, where efficiencies are high and contamination low, the Matrix Method has very little effect. In the very forward regions, where the asymmetry is diluted by QCD contamination, the Matrix Method correction is significant.

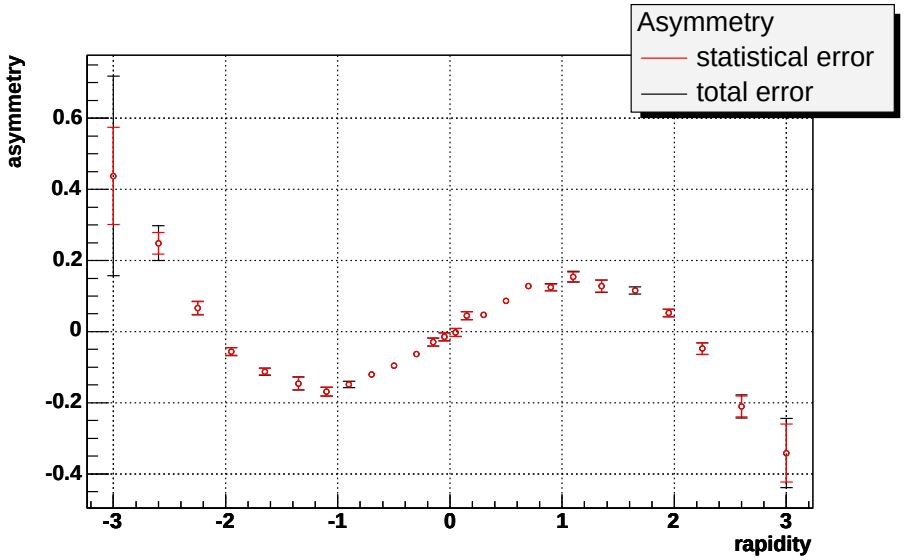

Figure 8.13. W Boson Production Asymmetry measured using Matrix Method.

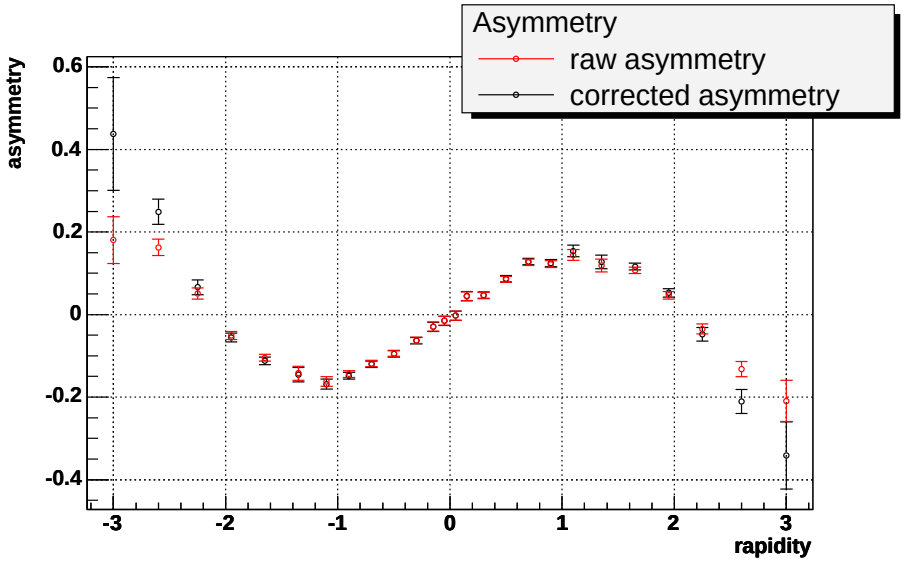

Figure 8.14. Effect of Matrix Method corrections on the "raw" asymmetry. Errors shown are statistical only.

8.5 Detector Charge Bias

In Section 2.6.1 it was stated that the measurement reduces to a counting experiment if the luminosity and acceptance $\times$ efficiency can be shown to charge independent. Though the luminosity by definition introduces no charge sensitive bias the same does not neccessarily hold for the acceptance or efficiency. The DØ detector is constructed from matter rather than anti-matter so, while such effects should be small, it is not inconceivable that some charge bias could be present in the acceptance $\times$ efficiency. This is investigated by comparing efficiencies measured for positrons and electrons separately and comparing them to look for significant differences (Figures 8.15 and 8.16).

A further cross-check for charge bias can be made by splitting the signal sample into two sub-samples based on the polarity of the solenoid field when the events were taken. Figure 8.17 shows the raw asymmetry, that is, uncorrected for the effects of background and charge misidentification, for forward and reverse field polarities.

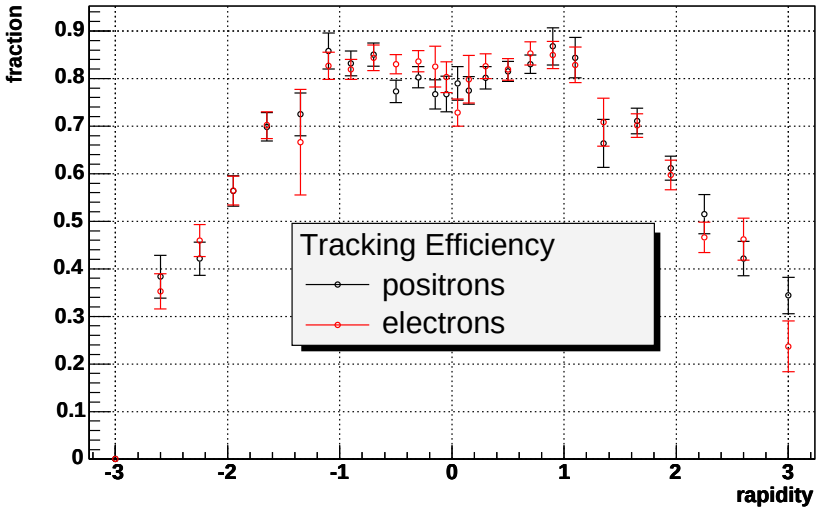

(a)

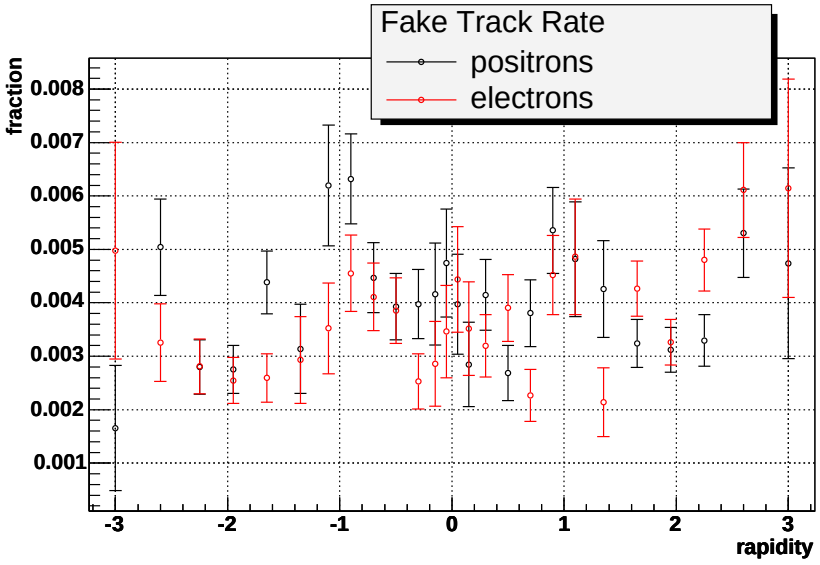

(b)

Figure 8.15. The tracking efficiency (a) and fake track rate (b) calculated separately for positrons and electrons. Errors are statistical.

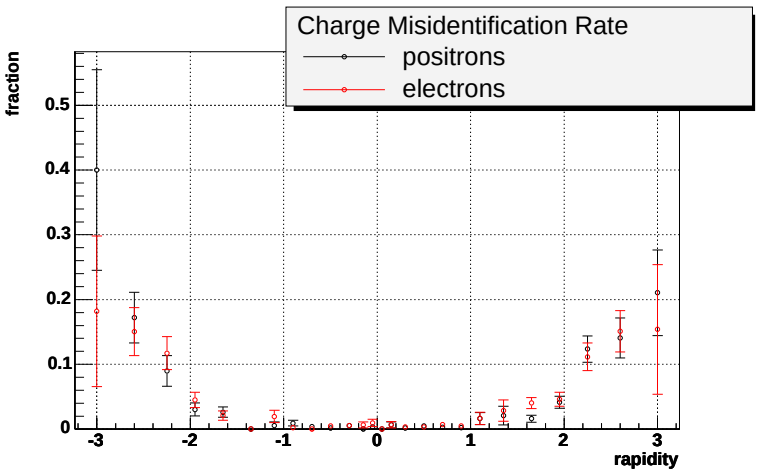

(a)

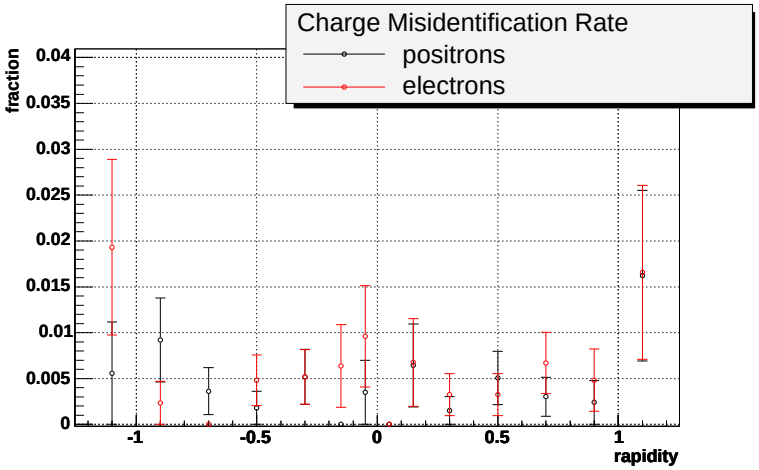

(b)

Figure 8.16. The charge misidentification rate with statistical errors across the whole rapidity range (a) and in the central calorimeter (b) calculated separately for positrons and electrons. There is no evidence of a systematic charge bias.

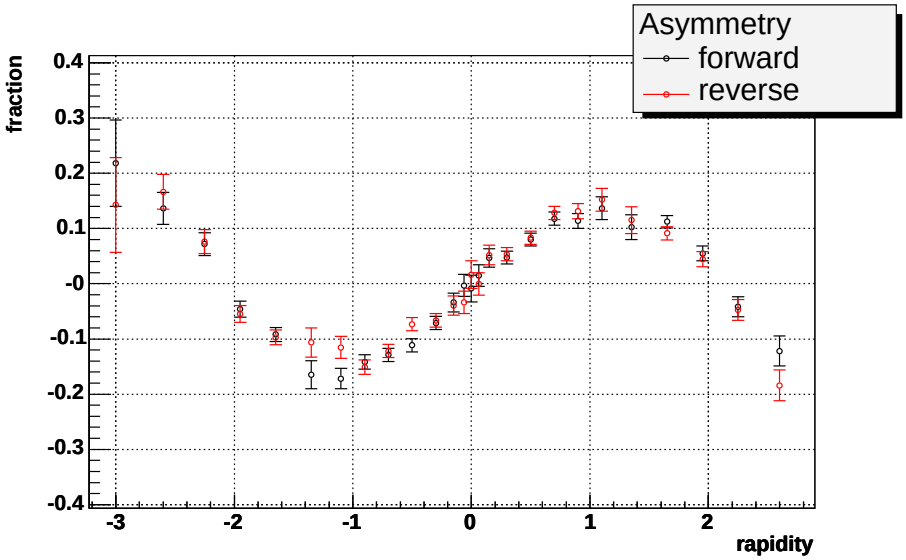

Figure 8.17. Raw electron asymmetry for the solenoid field in the forward and reverse polarizations. Errors are statistical.

8.6 Non-QCD Backgrounds

The background reduction method described above addresses only one source of background: QCD events in which one jet gets reconstructed as an electron. Other sources of background contamination are $Z \rightarrow ee$ events where one of the electrons is outside the fiducial region of the calorimeter and gets reconstructed as missing energy; and $W \rightarrow \tau\nu$ where the τ decays to an electron and neutrino. Both of these contributions are expected to be small: $Z \rightarrow ee$ because the Z boson production cross section is small relative to the W boson, and $W \rightarrow \tau\nu$ because the P_T spectrum of the decay electrons is soft.

To test this, 247k fully-simulated $Z \rightarrow ee$ events and 539750 fully-simulated $W \rightarrow \tau\nu$ events were run through the W boson selection software. Histograms were made of the rapidities of all the generated bosons, and the boson in events that pass the $W \rightarrow e\nu$ selection cuts. The ratio of these two histograms is shown in Figure 8.18(a) for $Z \rightarrow ee$ events and 8.19(a) for $W \rightarrow \tau\nu$ events.

It is difficult to produce similar distributions in the rapidity of the electron, because no suitable "tag" exists. In the $W \rightarrow \tau\nu$, not all events include an electron, and in the $Z \rightarrow ee$ sample, events include two electrons. Figures 8.18(b) and 8.19(b) show the distribution of the electron that passed the cuts in the $W \rightarrow e\nu$ selection. Since these distributions do not differ dramatically from the distribution in the candidate sample (Figure 8.20), it is assumed that the contamination is evenly distributed.

Summing over rapidity bins, 285 of 247k $Z \rightarrow ee$ events, passed the $W \rightarrow e\nu$ selection cuts. Because the production cross section of Z bosons is about 1/10 that of W bosons, this represents an effective contamination of 0.011%. From the $W \rightarrow \tau\nu$ sample, 5222 events or 0.97% passed the cut. Because the rate at which W bosons decay to τ and e is about the same, no further adjustment is needed.

Note that these numbers represent an upper limit to the contamination. The Monte Carlo used here was not run through the trigger simulation, so no trigger efficiencies are applied. Application of these efficiencies can only reduce the number of events that pass the $W \rightarrow e\nu$ selection cuts, so the contamination level must be less than that estimated here.

At this time, the precision of the measurement does not require that the asymmetry measurement be adjusted for this background.

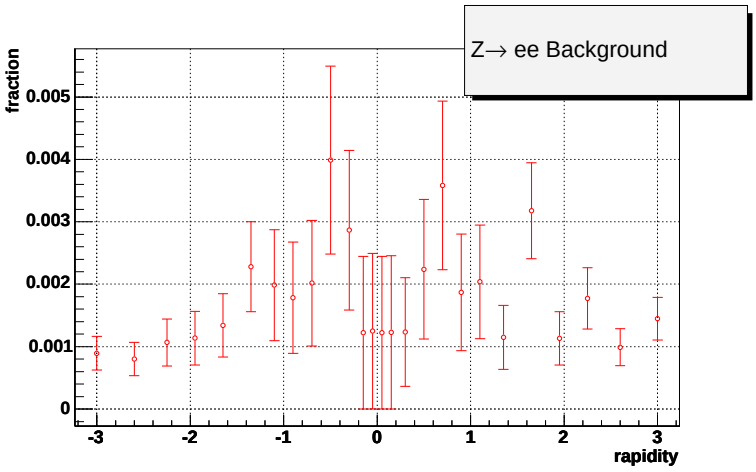

(a) Fraction of $Z \rightarrow ee$ Monte Carlo events that pass $W \rightarrow e\nu$ selection cuts, binned in the rapidity of the generated Z boson.

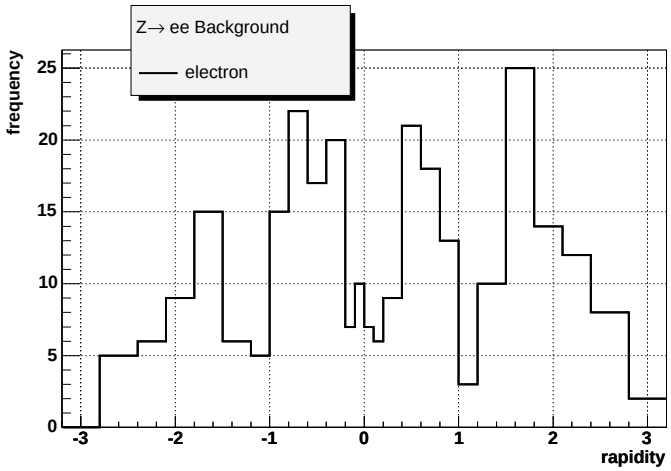

(b) Rapidity distribution of electrons from $Z \rightarrow ee$ Monte Carlo events passing $W \rightarrow e\nu$ selection cuts.

Figure 8.18. $Z \rightarrow ee$ background study.

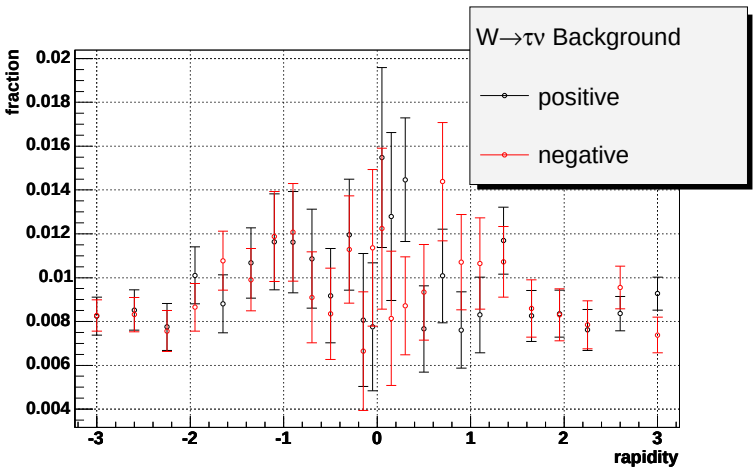

(a) Fraction of $W \rightarrow \tau\nu$ Monte Carlo events passing $W \rightarrow e\nu$ selection cuts, separately for positive and negative W bosons, binned in the rapidity of the generated W boson.

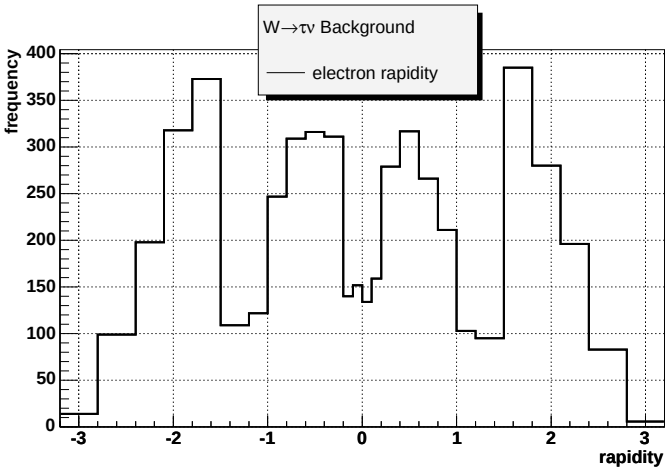

(b) Rapidity distribution of electrons from $W \rightarrow \tau\nu$ Monte Carlo events passing $W \rightarrow e\nu$ selection cuts.

Figure 8.19. $W \rightarrow \tau\nu$ background study.

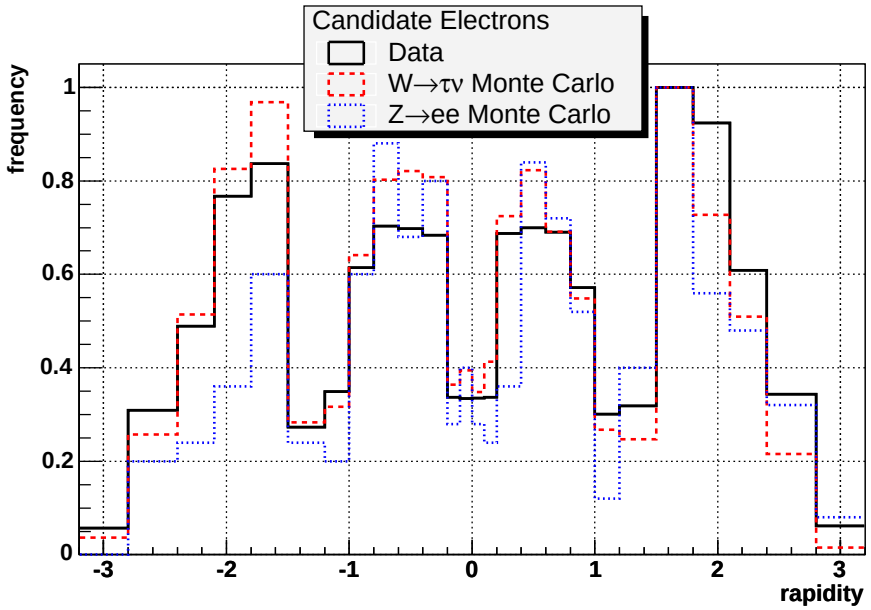

Figure 8.20. Rapidity distribution of electrons from data and Monte Carlo that pass $W \rightarrow e\nu$ selection cuts.

8.7 CP Folding

The asymmetry is expected to be CP invariant such that $A(y) = -A(-y)$. Figure 8.21 confirms that the data show no sign of CP violation.

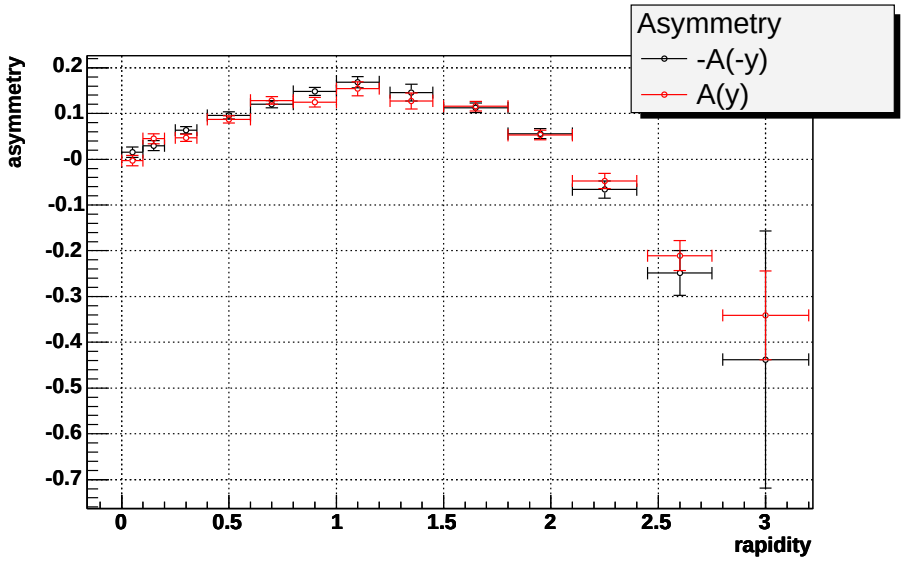

Figure 8.21. The asymmetry is CP invariant.

To increase statistical resolution, the asymmetry is "folded" via the transforms

$$N'_{trk^+}(y) = N_{trk^+}(y) + N_{trk^-}(-y),\ N'_{trk^-}(y) = N_{trk^-}(y) + N_{trk^+}(-y) \qquad (8.17)$$

and

$$N'_{notrk}(y) = N_{notrk}(y) + N_{notrk}(-y). \qquad (8.18)$$

The Poisson errors are recalculated. The efficiency coefficients ε, g, and f are averaged (e.g. $g'(y) = (g(y) + g(-y))/2$). Statistical errors are propagated quadratically. Systematic errors are assumed 100% correlated and propagated linearly. In the case of the tracking efficiency, in which the statistical and systematic errors are convolved, the total error is assumed systematic. A systematic error, $\Delta g_{CP} = |g(y) - g(-y)|$ is introduced and the total error recalculated. These calculations are summarized in Appendix A.

Once the data have been combined in this manner, the asymmetry is recalculated to produce Figure 8.22.

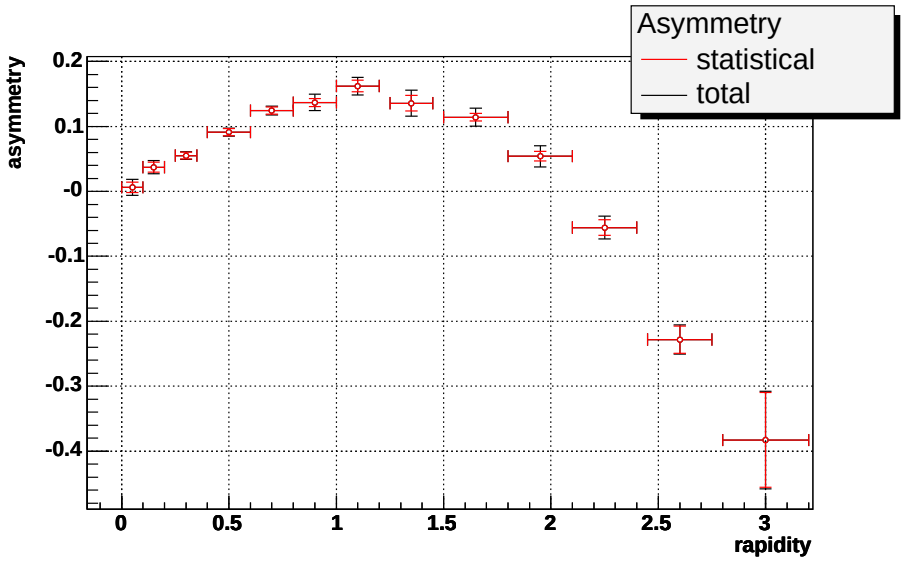

Figure 8.22. The CP folded asymmetry.

CHAPTER 9

RESULTS AND CONCLUSIONS

The results are summarized in Tables A.1 through A.4 where the contributions, systematic and statistical, are broken down. Tables A.8 and A.9 summarize the folded results. In calculating the total error it has been assumed that the systematic error contributions $\Delta\varepsilon_{sys}$, Δg_{sys} and Δf_{sys} are not correlated with each other, but that $\Delta\varepsilon_{sys}$ is 100% correlated with $\Delta\varepsilon_{CP}$, etc.

Figure 9.1 gives a graphical breakdown of the systematic error contributions from the track match efficiency, fake rate and charge misidentification rate determinations. It can been seen from these figures that although absolute value of the error on the misidentification rate is not disproportionate, its effect on the error on the asymmetry is, especially in the forward calorimeter regions ($y > 1.1$).

Figure 9.2 compares the measurement with the theoretical predictions discussed in Chapter 7 and a recently published measurement by the competing Fermilab experiment CDF [41].

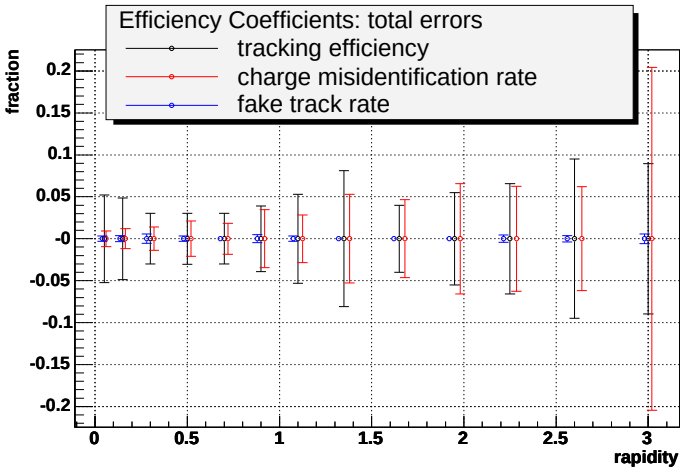

(a)

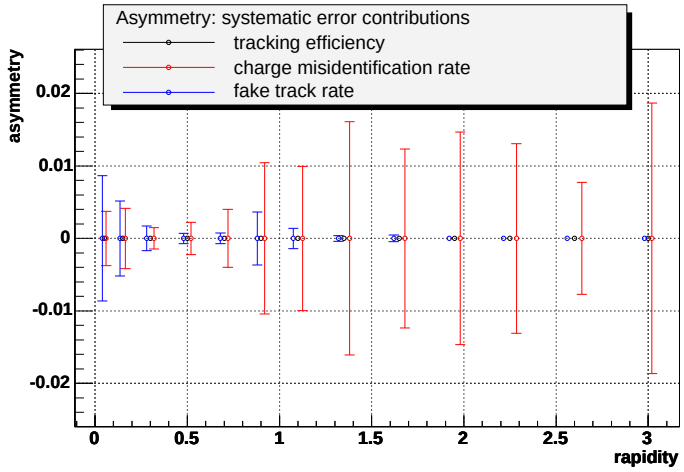

(b)

Figure 9.1. (a) The total error quoted for each of tracking efficiency, charge misidentification rate, and fake track rate. (b) The effect of each of the errors in (a) on the systematic uncertainty of the asymmetry. Note that at $y = 3.0$, the effect of the charge misidentification rate errors extends to $\pm.255$.

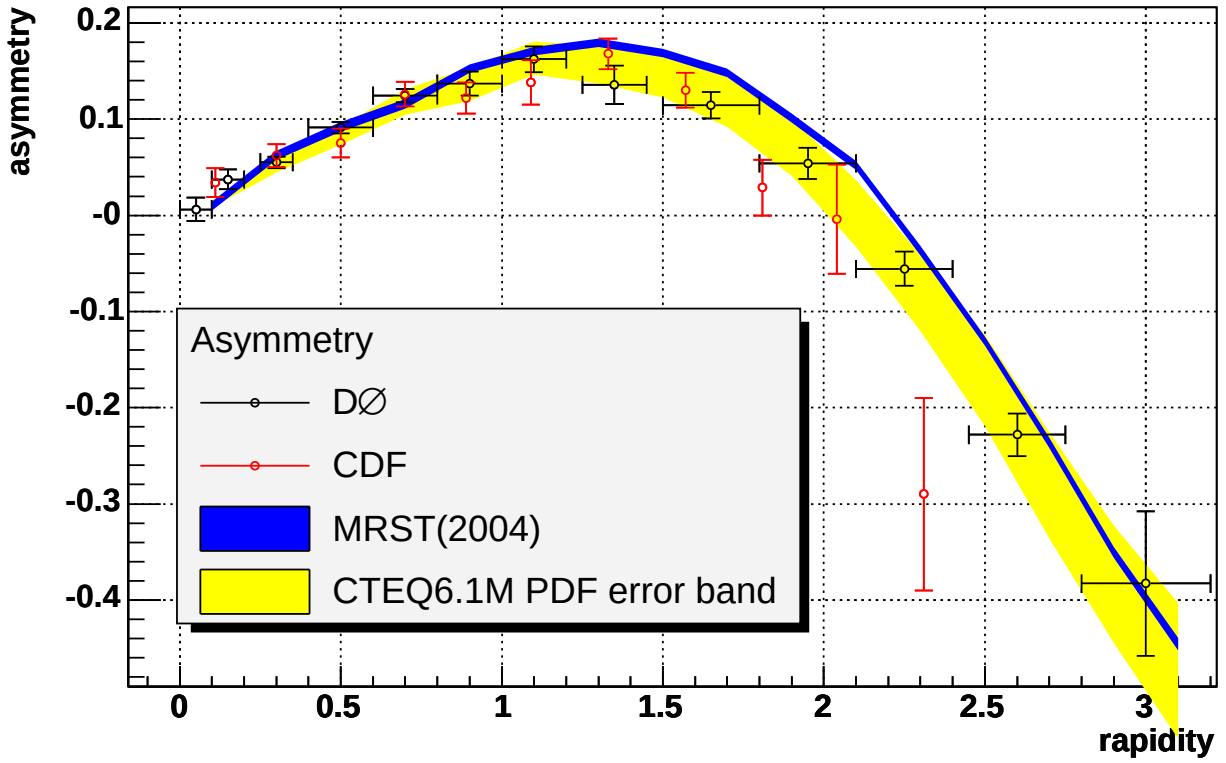

Figure 9.2. Asymmetry measurements from DØ and CDF shown with the CTEQ6.1M and MRST(2004) predictions.

In this plot, the blue band denotes the asymmetry measured in Monte Carlo where the MRST(2004) PDF was used in event generation. The thickness of the line represents the estimated statistical error arising from the finite statistics of the sample.

The yellow band is the CTEQ6.1M prediction. In addition to the statistical error, this band includes an estimate of the error on the PDF calculation.

Since the PDF are calculated by fitting to data, uncertainty arises from the underlying experimental uncertainty, as well as uncertainty in the fits. Until recently, the PDF collaborations neglected to address these uncertainties. The PDF collaborations are now beginning to include error estimates, which they typically calculate by adjusting the input parameters up and down by a standard deviation.

Unfortunately, at this time, the Legacy grid files required as input to ResBos-A (see Section 7.1.1) are not available for the MRST(2004) error set. While at first glance the data seem to correlate more strongly with the CTEQ prediction, were the MRST band as thick as the CTEQ band and centered at its current position, the situation would be less dramatic. The data would tend to sit at the lower edge of the MRST band. Perhaps it can be best said that the data show a strong but not definitive preference for the CTEQ PDF.

In all but the highest rapidity bin, the errors on the measurement are smaller than the estimated error on the CTEQ fit. This is very suggestive that this measurement will be useful in improving constraints on the existing parameterization.

Of considerable importance is the improvement this measurement represents over the world's best measurement, which is shown by the red points. The luminosity represented by the CDF measurement is about half of what is included

in this measurement. However, pure statistical scaling would suggest that for the point $2.0 < y < 2.5$, the CDF error ≈ 0.1 would translate to a DØ error ≈ 0.07. The measured error in this bin is less than a third that: 0.018.

This suggests that not only does the DØ measurment exceed the CDF measurement in statistical precision, but also in control of systematic errors. The greatest accomplishment of the DØ measurment, though, is the extension of the asymmetry measurement to $y = 3.0$. While the tracking coverage of the CDF detector restricts their measurement to $y < 2.3$, tracking instrumentation to $\eta_{det} = 3.0$ at DØ provides two statistically significant data points beyond that. Improvements in the understanding of the forward detector, as well as increased statistics will improve the significance of these points in the future.

As shown in Section 2.4, the rapidity and the momentum fraction, x, are correlated such that the expansion of the rapidity range corresponds to an expansion of the range of x that is probed. While these values of x are exotic at the Tevatron, it can be expected that future generations of colliders will have higher energies, and thus *lower* average x. In this way, the measurement of the asymmetry at high rapidities at the Tevatron will have relevance into the future of high energy physics.

APPENDIX A

CALCULATION TABLES

TABLE A.1

MATRIX METHOD INPUT AND RESULTS FOR $y < 0$

y	N_{trk+}	N_{trk+}	N_{notrk}	ε	g	f	A
-2.60	221	170	5486	0.37	0.1453	0.01179	0.2163
-2.25	431	471	7979	0.44	0.1258	0.01006	-0.06426
-1.95	790	969	11888	0.56	0.02174	0.01178	-0.1146
-1.65	1034	1315	13094	0.7	0.01848	0.01686	-0.1363
-1.35	241	300	3772	0.7	0	0.01265	-0.1191
-1.10	539	748	5801	0.84	0.006993	0.009805	-0.1721
-0.90	1156	1534	9520	0.83	0.004983	0.009959	-0.1469
-0.70	1368	1786	10211	0.85	0.002601	0.008015	-0.1366
-0.50	1457	1759	9459	0.8	0.003731	0.007075	-0.09647
-0.30	1481	1695	8872	0.82	0.006281	0.006143	-0.06934
-0.15	733	789	4482	0.8	0.009901	0.00703	-0.03827
-0.05	744	748	4425	0.79	0.005025	0.006239	-0.002755

TABLE A.2

MATRIX METHOD INPUT AND RESULTS FOR $y > 0$

y	N_{trk^+}	N_{trk^+}	N_{notrk}	ε	g	f	A
0.05	798	758	4299	0.75	0.005141	0.005733	0.02634
0.15	825	691	4384	0.79	0.002611	0.007469	0.09065
0.30	1634	1469	8982	0.82	0.003563	0.007026	0.05459
0.50	1677	1486	9474	0.82	0.003932	0.007622	0.06219
0.70	1738	1327	9930	0.84	0.00492	0.008075	0.1389
0.90	1333	1088	8752	0.85	0.005396	0.009597	0.1058
1.10	576	433	4885	0.84	0.02724	0.01196	0.1588
1.35	392	290	4511	0.68	0	0.01242	0.1622
1.65	1644	1286	15618	0.71	0.02719	0.01741	0.1416
1.95	1033	993	14411	0.6	0.03934	0.01103	0.0231
2.25	552	557	9956	0.49	0.1199	0.01004	-0.006457
2.60	222	263	6194	0.44	0.1677	0.009517	-0.1432

TABLE A.3

ERROR CONTRIBUTIONS TO THE ASYMMETRY FOR $y < 0$

y	$\Delta\varepsilon$	Δg	Δf	ΔA_{sys}	ΔA_{stat}	ΔA_{tot}
-3.00	0.041	0.13	0.0035	0.25	0.14	0.28
-2.60	0.026	0.054	0.0012	0.038	0.03	0.049
-2.25	0.023	0.037	0.0014	0.0062	0.018	0.019
-1.95	0.022	0.026	0.00072	0.0031	0.011	0.011
-1.65	0.02	0.02	0.0011	0.0047	0.0091	0.01
-1.35	0.047	0.018	0.0011	0.0052	0.017	0.018
-1.10	0.026	0.0046	0.0014	0.0017	0.012	0.012
-0.90	0.018	0.0099	0.0025	0.0031	0.0084	0.0089
-0.70	0.016	0.0056	0.0007	0.0014	0.0076	0.0077
-0.50	0.015	0.0077	0.0011	0.0015	0.0076	0.0078
-0.30	0.014	0.0076	0.0019	0.00099	0.0077	0.0078
-0.15	0.017	0.0078	0.0012	0.00047	0.011	0.011
-0.05	0.024	0.003	0.0014	0.0001	0.011	0.011

TABLE A.4

ERROR CONTRIBUTIONS TO THE ASYMMETRY FOR $y > 0$

y	$\Delta\varepsilon$	Δg	Δf	ΔA_{sys}	ΔA_{stat}	ΔA_{tot}
0.05	0.024	0.0065	0.0012	3.6e-05	0.011	0.011
0.15	0.027	0.0042	0.0028	0.00044	0.011	0.011
0.30	0.016	0.0051	0.002	0.00051	0.0077	0.0077
0.50	0.015	0.012	0.002	0.0021	0.0077	0.008
0.70	0.014	0.011	0.0012	0.0029	0.0077	0.0082
0.90	0.019	0.021	0.0018	0.0054	0.0087	0.01
1.10	0.027	0.02	0.0016	0.0064	0.014	0.015
1.35	0.034	0.016	0.0011	0.0043	0.017	0.017
1.65	0.018	0.025	0.00069	0.0061	0.0083	0.01
1.95	0.019	0.031	0.00062	0.0036	0.0099	0.011
2.25	0.024	0.022	0.0015	0.0027	0.016	0.017
2.60	0.026	0.023	0.0014	0.014	0.029	0.033
3.00	0.041	0.052	0.0027	0.053	0.082	0.097

TABLE A.5

CP FOLDING FO THE TRACKING EFFICIENCY

y	ε	$\Delta\varepsilon_{stat}$	$\Delta\varepsilon_{sys}$	$\Delta\varepsilon_{CP}$	$\Delta\varepsilon_{tot}$
0.05	0.77	-	0.048	0.02	0.052
0.15	0.79	-	0.044	0.02	0.049
0.30	0.82	-	0.03	0.001	0.03
0.50	0.82	-	0.03	0.0049	0.03
0.70	0.84	-	0.03	0.0004	0.03
0.90	0.84	-	0.037	0.014	0.039
1.10	0.84	-	0.052	0.0085	0.053
1.35	0.69	-	0.081	0.0061	0.081
1.65	0.71	-	0.038	0.013	0.04
1.95	0.58	-	0.041	0.037	0.055
2.25	0.46	-	0.047	0.045	0.066
2.60	0.4	-	0.052	0.079	0.095
3.00	0.28	-	0.082	0.036	0.09

TABLE A.6

CP FOLDING OF THE CHARGE MISID RATE

y	g	Δg_{stat}	Δg_{sys}	Δg_{CP}	Δg_{tot}
0.05	0.0046	0.0019	0.0062	0.003	0.0094
0.15	0.0052	0.0019	0.01	0.0015	0.012
0.30	0.0037	0.0012	0.012	0.0016	0.014
0.50	0.0037	0.0012	0.019	0.0016	0.021
0.70	0.0026	0.00098	0.016	0.0021	0.019
0.90	0.0051	0.0016	0.031	0.0037	0.035
1.10	0.015	0.0041	0.019	0.0094	0.028
1.35	0.011	0.005	0.03	0.023	0.053
1.65	0.025	0.0036	0.043	0.0028	0.046
1.95	0.039	0.0051	0.055	0.01	0.066
2.25	0.11	0.011	0.048	0.013	0.063
2.60	0.16	0.017	0.05	0.0098	0.062
3.00	0.22	0.054	0.084	0.11	0.2

TABLE A.7

CP FOLDING OF THE FAKE TRACK RATE

y	f	Δf_{stat}	Δf_{sys}	Δf_{CP}	Δf_{tot}
0.05	0.0063	0.00073	0.0015	0.0016	0.0032
0.15	0.0053	0.00067	0.0034	0.0001	0.0036
0.30	0.0058	0.00049	0.0036	0.002	0.0056
0.50	0.0065	0.00051	0.0027	0.00042	0.0031
0.70	0.0057	0.00047	0.0011	0.00081	0.002
0.90	0.008	0.00061	0.0039	0.00083	0.0048
1.10	0.0088	0.00088	0.0017	0.0014	0.0032
1.35	0.0056	0.00067	0.0012	0.00026	0.0016
1.65	0.0073	0.00044	0.0012	0.00099	0.0023
1.95	0.0066	0.0004	0.00068	0.0013	0.0021
2.25	0.0072	0.00048	0.0025	0.0019	0.0044
2.60	0.0098	0.00074	0.0016	0.002	0.0037
3.00	0.0099	0.0017	0.0037	0.0018	0.0057

TABLE A.8

MATRIX METHOD INPUT AND RESULTS FOR CP SYMMETRIC RAPIDITY BINS

y	N_{trk^+}	N_{trk^-}	N_{notrk}	ε	g	f	A
0.05	8293	8193	33111	0.77	0.004621	0.006319	0.00619
0.15	8741	8125	33030	0.79	0.005169	0.005332	0.03724
0.30	18278	16398	66949	0.82	0.003686	0.005779	0.05517
0.50	19158	16009	68362	0.82	0.003737	0.006476	0.09125
0.70	19438	15196	68600	0.84	0.002595	0.005661	0.1244
0.90	16189	12378	59314	0.84	0.005066	0.007969	0.1369
1.10	7514	5510	35182	0.84	0.01499	0.008783	0.1622
1.35	4163	3210	36452	0.69	0.01142	0.005627	0.1357
1.65	16824	13595	105689	0.71	0.02482	0.007311	0.1143
1.95	12250	11114	101946	0.58	0.03948	0.006568	0.0541
2.25	5897	6411	68998	0.46	0.1128	0.007239	-0.05575
2.60	2313	3104	42975	0.4	0.158	0.009812	-0.2282
3.00	276	411	8105	0.28	0.2164	0.009911	-0.3829

TABLE A.9

ERROR CONTRIBUTIONS TO THE ASYMMETRY FOR CP SYMMETRIC RAPIDITY BINS

y	$\Delta\varepsilon$	Δg	Δf	ΔA_{sys}	ΔA_{stat}	ΔA_{tot}
0.05	0.052	0.0094	0.0032	0.0094	0.0079	0.012
0.15	0.049	0.012	0.0036	0.0066	0.0078	0.01
0.30	0.03	0.014	0.0056	0.0023	0.0055	0.0059
0.50	0.03	0.021	0.0031	0.0023	0.0054	0.0059
0.70	0.03	0.019	0.002	0.0041	0.0054	0.0068
0.90	0.039	0.035	0.0048	0.011	0.006	0.013
1.10	0.053	0.028	0.0032	0.01	0.0091	0.014
1.35	0.081	0.053	0.0016	0.016	0.012	0.02
1.65	0.04	0.046	0.0023	0.012	0.0061	0.014
1.95	0.055	0.066	0.0021	0.015	0.0073	0.016
2.25	0.066	0.063	0.0044	0.013	0.012	0.018
2.60	0.095	0.062	0.0037	0.0077	0.021	0.022
3.00	0.09	0.2	0.0057	0.019	0.073	0.075

APPENDIX B

RESBOS-A/PMCS MONTE CARLO

While the Pythia/DØGSTAR-DØsim Monte Carlo has been well-tested by the collaboration, the private production of the ResBos-A Monte Carlo and the specialized tuning of wz_epmcs suggests that some rudimentary checking of the Monte Carlo against the data is in order.

Figures B.1-B.6 compare the electron transverse momentum ($P_T(e)$), missing transverse energy ($\not\!\!E_T$), and transverse mass (M_T) distributions from the smeared Monte-Carlo (histogram) with the distributions from data (points). Note that the Monte Carlo represents only signal, whereas the data is expected to be contaminated by background. Simplistic background removal was performed by estimating a background shape from the loose background sample described in 8.1 and then subtracting the scaled distribution from the data plot. For the transverse momentum and missing transverse energy distributions, "signal" was removed by making a hard inverse-HMatrix cut, HMx8 (HMx7) > 50. For the transverse mass distribution, the electron was required to have a track match.

Comparisons have been made separately for the central calorimeter north (CCN) and south (CCS), the south end calorimeter (ECS) and the north end calorimeter (ECN). These regions are defined in the detector pseudorapidity of the reconstructed electron, η_{det}, as follows:

- ECN : $-2.8 < \eta_{det} < -1.2$

- CCN : $-1.2 < \eta_{det} < 0.$
- CCS : $0. < \eta_{det} < 1.2$
- ECS : $1.2 < \eta_{det} < 2.8$

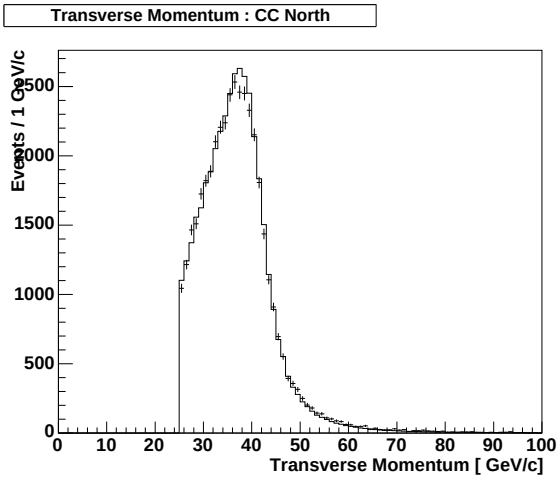

(a)

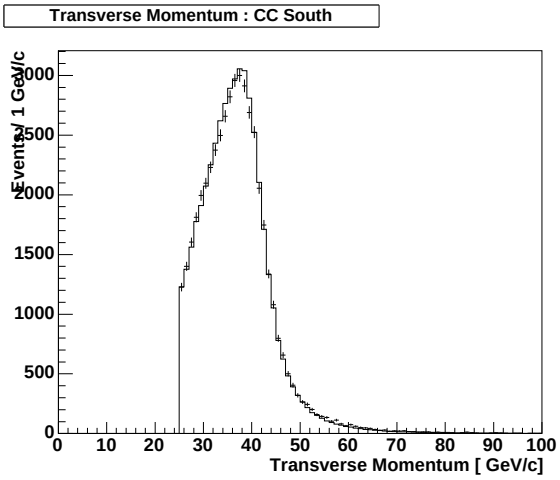

(b)

Figure B.1. Transverse momentum distribution of of data (points) and Monte Carlo (lines) electrons in the a) CCN and b)CCS.

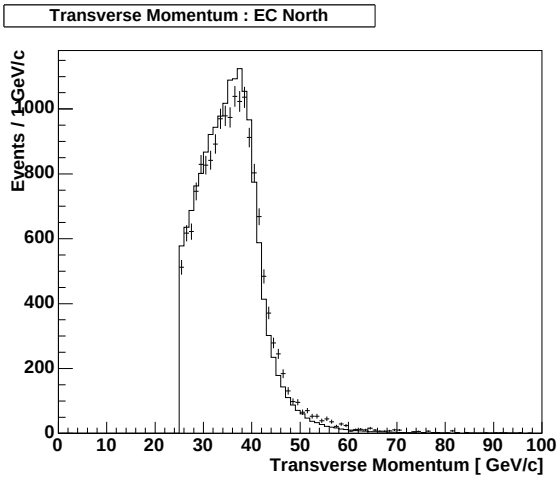

(a)

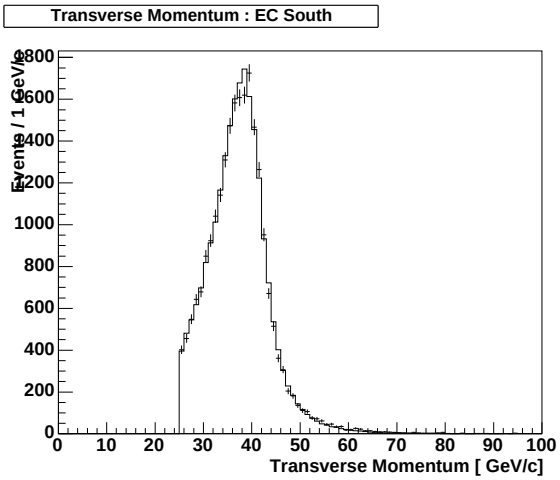

(b)

Figure B.2. Transverse momentum distribution of data (points) and Monte Carlo (lines) electrons in the a) ECN and b)ECS.

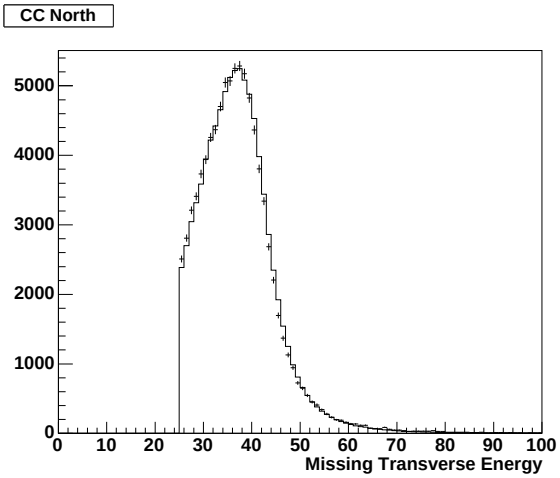

(a)

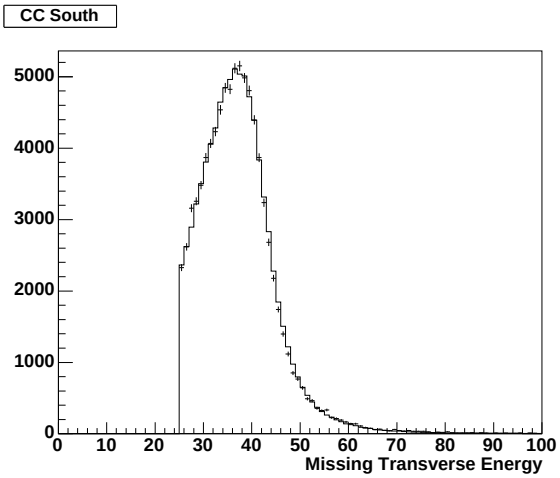

(b)

Figure B.3. Data (points) and Monte Carlo (lines) $\not\!\!E_T$ distribution of events with electrons in the a) CCN and b)CCS.

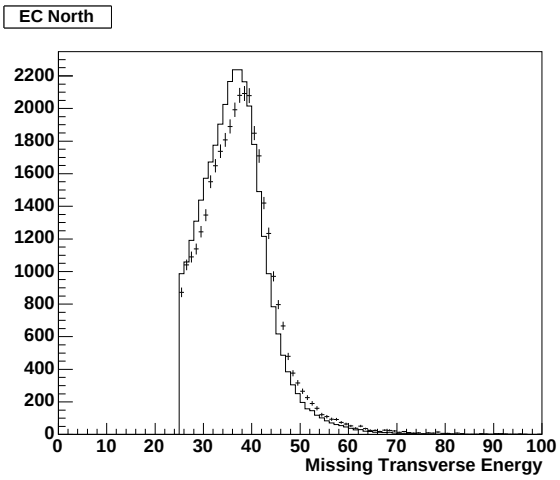

(a)

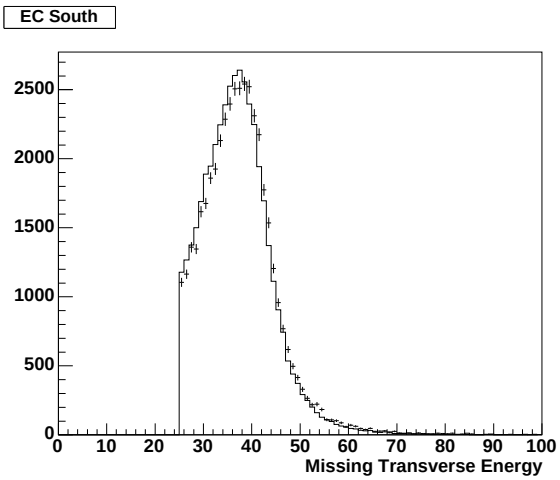

(b)

Figure B.4. Data (points) and Monte Carlo (lines) $\not\!\!E_T$ distribution of events with electrons in the a) ECN and b)ECS.

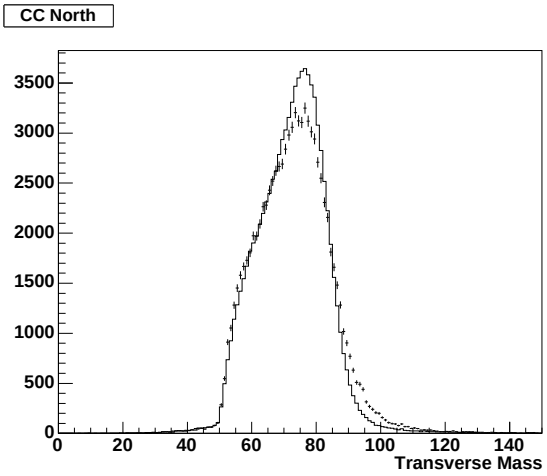

(a)

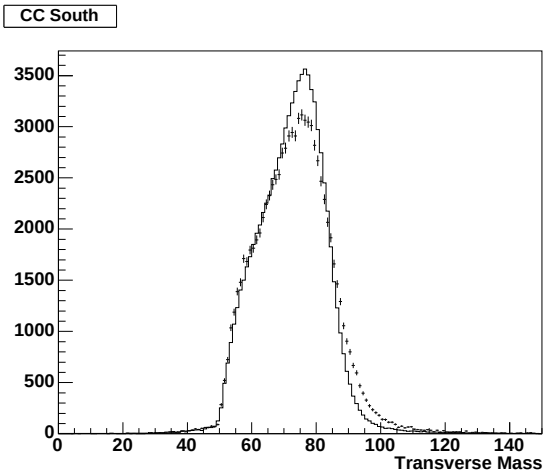

(b)

Figure B.5. Data (points) and Monte Carlo (lines) transverse mass distribution of events with electrons in the a) CCN and b)CCS.

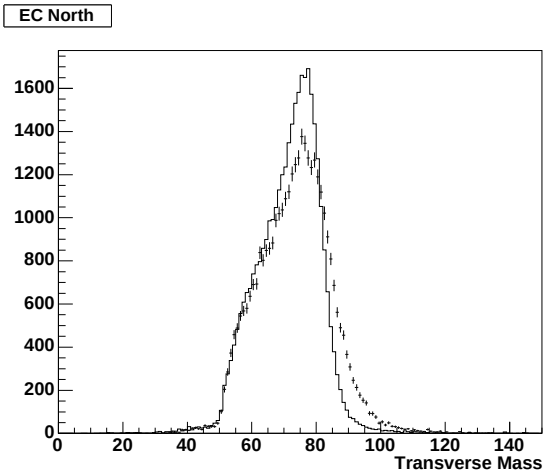

(a)

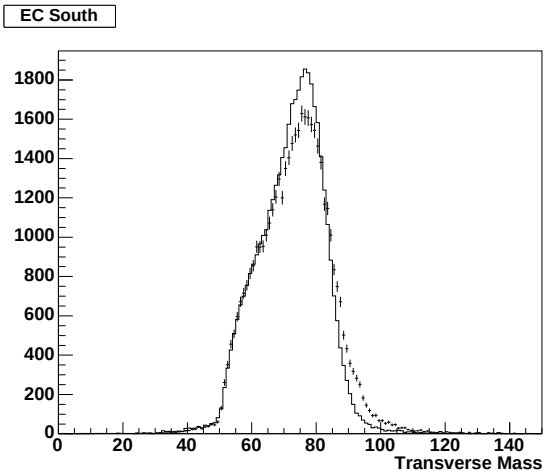

(b)

Figure B.6. Data (points) and Monte Carlo (lines) transverse mass distribution of events with electrons in the a) ECN and b)ECS.

Clearly, these distributions could be more finely tuned. But, as in many aspects of this analysis, effects tend to cancel. What is important is how the asymmetry distribution is affected by small changes in these distributions.

The following plots show the change in asymmetry versus rapidity as each one of the P_T and $\not\!\!E_T$ resolution and scale parameters was varied. The red circles show the change in the measured lepton asymmetry when a standard smearing is applied. This distribution represents the baseline "detector effect."

In some of the plots, particularly the $\not\!\!E_T$ distributions (Figures B.9 and B.10), the slope of this distribution is alarming. Note however, that at $y = -3.0$ where the value of the distributions is greatest, the relative difference between generated and smeared asymmetries is $\approx 3\%$, while the width of the error band is twice that. Even at $y = 2.0$, which is very near $A = 0$, to which point the relative error asymptotically increases, the total effect of smearing is only $\approx 10\%$.

More significant is comparison of this baseline with the $\pm 1\ \sigma$ variations shown in blue boxes and green triangles. To form these distributions, the smearing parameter in question was adjusted a standard deviation up or down, the Monte Carlo was re-smeared, and the asymmetry re-measured.

The largest relative shift is when the P_T scale is adjusted $\pm 1\ \sigma$ (Figure B.8). Again, the effect on the Monte Carlo distribution is $\approx 1\%$, while the uncertainty on the distribution is $\approx 7\%$.

The conclusion is that while significant understanding may be gained by investigating improvements in the PMCS smearing of ResBos-A Monte Carlo, there is little discriminatory power to be gained.

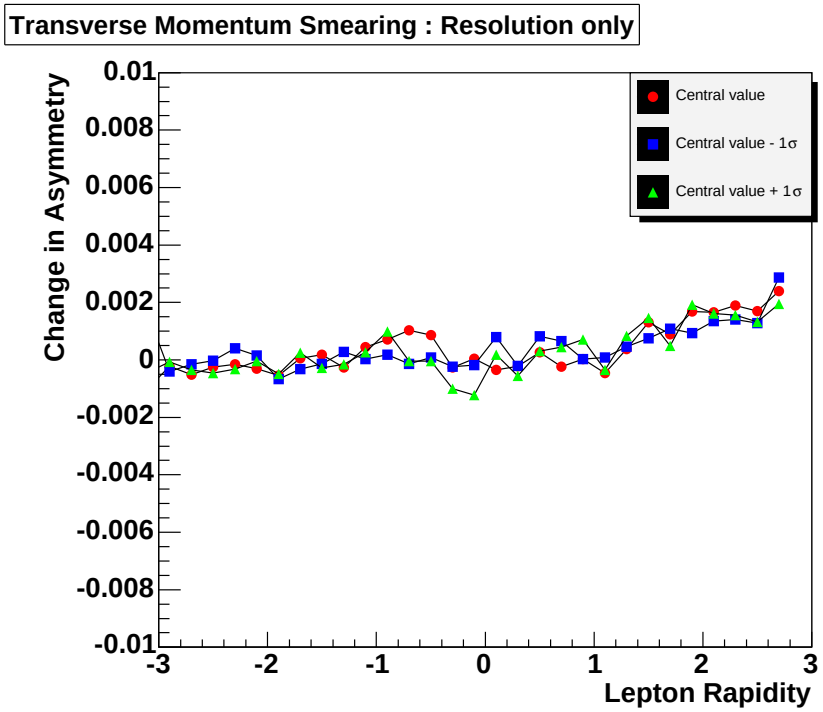

Figure B.7. Sensitivity to electron transverse momentum resolution.

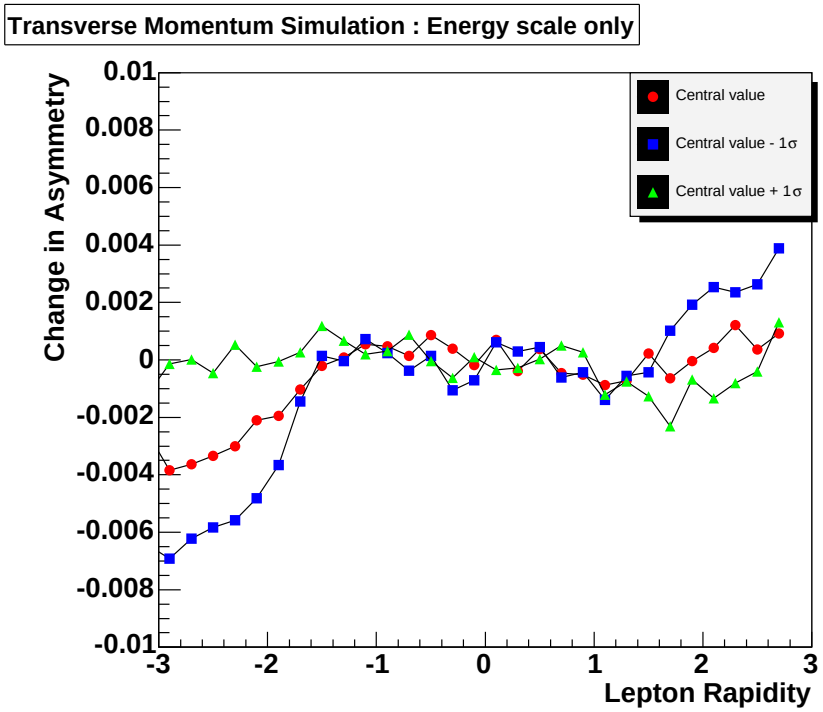

Figure B.8. Sensitivity to electron transverse momentum scale.

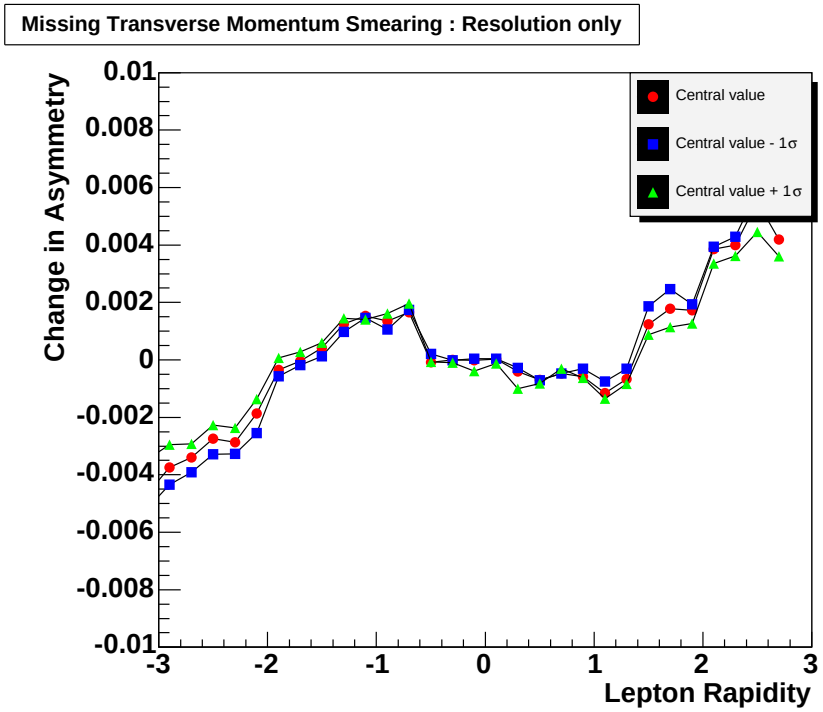

Figure B.9. Sensitivity to missing transverse momentum resolution.

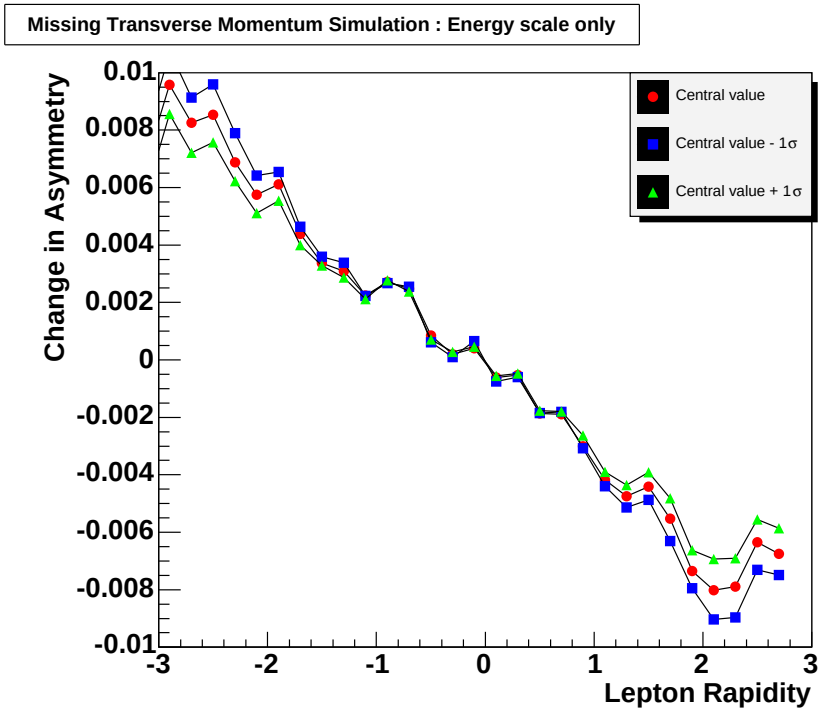

Figure B.10. Sensitivity to missing transverse momentum scale.

REFERENCES

1. Albert Einstein. A new determination of molecular dimensions. *Annalen Phys.*, 19:289–305, 1906.

2. Albert Einstein. On the motion of small particles suspended in liquids at rest required by the molecular-kinetic theory of heat. *Annalen Phys.*, 17:549–560, 1905.

3. Albert Einstein. On the electrodynamics of moving bodies. *Annalen Phys.*, 17:891–921, 1905.

4. Albert Einstein. Does the inertia of a body depend on its energy content? *Annalen Phys.*, 18:639–641, 1905.

5. Albert Einstein. On a heuristic viewpoint concerning the production and transformation of light. *Annalen Phys.*, 17:132–148, 1905.

6. David Griffiths. *Introduction to Elementary Particles*. John Wiley & Sons, 1987.

7. R. K. Ellis, W. J. Stirling, and B. R. Webber. *QCD and Collider Physics*. Monographs on Particle Physics. Cambridge University Press, 1996, 2003.

8. Francis Halzen and Alan D. Martin. *Quarks & Leptons: An Introductory Course in Modern Particle Physics*. John Wiley & Sons, 1984.

9. Stefano Forte. Structure functions and parton distributions. *Nucl. Phys.*, A755:100–110, 2005.

10. Byron Roe. *Particle Physics at the New Millennium*. Springer, New York, USA, 1996.

11. Gordon Kane. *Modern Elementary Particle Physics*. Addison-Wesley, Redwood City, USA, 1987.

12. `http://www-bd.fnal.gov/public/antiproton.html#cooling`; accessed May 9, 2005.

13. J.D. Jackson. Kinematics. *The European Physical Journal C: Review of Particle Physics*, 3(1-4), 1998.

14. J. Ellison. The DØ detector upgrade and physics program. In M.N. Dubinin and V.I. Savrin, editors, *PROCEEDINGS of the 15th International Workshop On High-Energy Physics And Quantum Field Theory (QFTHEP 2000), 14-20 Sep 2000, Tver, Russia*. Institute of Nuclear Physics, Moscow State University, September 2000.

15. DØ Upgrade Collaboration. DØ Silicon Tracker Technical Design Report. http://d0server1.fnal.gov/projects/silicon/www/tdr_final.ps, 1994.

16. D. Adams et al. The DØ upgrade: Central fiber tracker, technical design report. Technical Report 4164, DØ, 2003.

17. M. Adams et al. Design report of the central preshower detector for the DØ upgrade. Technical Report 3014, DØ, 1996.

18. A. Gordeev et al. Technical design report of the forward preshower detector for the DØ upgrade. Technical Report 3445, DØ, 1998.

19. Hai Zheng. *A Search for Large Extra Dimensions in the Jet + $\not\!\!E_T$ Final State in $\sqrt{s}$ = 1.8-TeV $p\overline{p}$ Collisions at DØ*. PhD thesis, University of Notre Dame, April 2002.

20. Linda Coney. *Diffractive W and Z Boson Production in $p\overline{p}$ Collisions at $\sqrt{s} = 1800$ GeV*. PhD thesis, University of Notre Dame, April 2000.

21. B. Baldin et al. Technical Design Report of the Central Muon System. Technical Report 3365, DØ, 1997.

22. G. Alexeev et al. Technical Design Report for the DØ Forward Muon Tracking Detector Based on Mini-drift Tubes. Technical Report 3366, DØ, 1997.

23. Ryan J. Hooper. *A Search For Large Extra Spatial Dimensions and Z' Bosons in the Dimuon Final State in $\sqrt{s}$ = 1.96 TeV $p\overline{p}$ Collicsions at DØ*. PhD thesis, University of Notre Dame, April 2004.

24. R Schwienhorst. The DØ Run 2 trigger system. To appear in the proceedings of DPF 2004: Annual Meeting of the Division of Particles and Fields (DPF) of the American Physical Society (APS), Riverside, California, 26-31 Aug 2004, submitted to Int.J.Mod.Phys.A, 2004.

25. Adam Yurkewicz. *Search for Evidence of Supersymmetry in the Like-Sign Dimuon Channel in the DØ Experiment*. PhD thesis, Michigan State University, 2004.

26. http://www.pa.msu.edu/~balazs/ResBos/; accessed May 10, 2005.

27. http://hep.pa.msu.edu/wwwlegacy/; accessed May 10, 2005.

28. http://www.pa.msu.edu/~balazs/ResBos/Grids/WPM_Grids.html; accessed May 10, 2005.

29. Torbjorn Sjostrand, Leif Lonnblad, Stephen Mrenna, and Peter Skands. Pythia 6.3: Physics and manual, 2003.

30. http://www-d0.fnal.gov/computing/mcprod/mcc.html; accessed May 10, 2005.

31. http://www-d0.fnal.gov/computing/algorithms/status/releases.htm; accessed May 13, 2005.

32. http://www-d0.fnal.gov/Run2Physics/cs/fixing/fixing.html; accessed May 13, 2005.

33. http://www-d0.fnal.gov/Run2Physics/cs/skimming/pass2.html; accessed May 13, 2005.

34. http://www-d0.fnal.gov/Run2Physics/cs/d0correct/d0correct.html; accessed May 13, 2005.

35. http://d0db.fnal.gov/run/runQuery.html; accessed May 13, 2005.

36. http://www-clued0.fnal.gov/~pverdier/d0_private/MetRunSel/; accessed May 13, 2005.

37. http://www-d0.fnal.gov/phys_id/luminosity/; accessed May 13, 2005.

38. Doug Chapin, Harald Fox, John Gardner, Robert Illingworth, Adam Lyon, and Junjie Zhu. Measurement of $\mathtt{Z} \rightarrow ee$ and $W \rightarrow e\nu$ production cross sections with $|\eta| < 2.3$. Technical Report 4403, DØ, 2004.

39. http://www-d0.fnal.gov/phys_id/jets/jetid.html; accessed May 13, 2005.

40. M. Strauss. Material and tracking. All DØ Meeting. Feb. 11, 2005.

41. D. Acosta et al. Measurement of the forward-backward charge asymmetry from $w \rightarrow e\nu$ production in $p\overline{p}$ collisions at $\sqrt{s}$ =1.96 tev. *Phys. Rev.*, D71:051104, 2005.

This document was prepared & typeset with LaTeX 2_ε*, and formatted with* NDdiss2_ε *classfile (v1.0[2004/06/15]) provided by Sameer Vijay.*